Supplementary Information (SI) for Energy & Environmental Science.

Supporting Information

Data-driven Discovery of Electrode Materials for Protonic Ceramic Cells

Xueyu Hu,[a] Yucun Zhou,[a] Zheyu Luo,[a] Haoyu Li,[a] Nai Shi,[b] Zhijun Liu,[a] Weilin Zhang,[a] Weining Wang,[a] Yong Ding[a] and Meilin Liu*[a]

[a]School of Materials Science and Engineering, Georgia Institute of Technology; Atlanta, 30332-0245, USA

[b]Kyushu University Platform of Inter-/Transdisciplinary Energy Research, Kyushu University; Fukuoka, 819-0395, Japan

*Corresponding author: meilin.liu@mse.gatech.edu

Experimental Details

Preparation of Oxygen Electrode Powders. The oxygen electrode powders were synthesized using the EDTA-citric acid method. Initially, a stoichiometric quantity of metal nitrates (obtained from Aldrich Chemicals) was combined with ethylenediaminetetraacetic (EDTA) and citric acid (CA) in deionized water, maintaining a molar ratio of metal ions to EDTA to CA of 1: 1: 2. Ammonium hydroxide was employed to adjust the pH to 6. Subsequently, the water was evaporated, yielding a gel that was calcined at 300°C for 10 hours. The resulting primary powder was ground and subjected to further calcination at 1000°C for 5 hours.

Preparation of Electrolyte Powders. The electrolyte powders $BaZr_{0.1}Ce_{0.7}Y_{0.1}Yb_{0.1}O_{3-\delta}$ (BZCYYb1711) and $BaSn_{0.1}Ce_{0.7}Yb_{0.2}O_{3-\delta}$ (BSCYb172) were synthesized using the solid-state-reaction method. Stochiometric amounts of barium carbonate, zirconium oxide, cerium oxide, yttrium oxide, ytterbium oxide, and tin oxide powders (obtained from Aldrich Chemicals) were subjected to ball milling at 400 rpm for 4 hours in ethanol. Subsequently, the mixture was dried and calcinated at 1100°C for 10 hours in the air. Following calcination, the powder underwent another round of ball milling (at 400 rpm for 4 hours) and calcination (at 1100°C for 10 hours) before being utilized for further applications.

Fabrication of Strip Samples. The green strip samples were fabricated by uniaxially dry pressing the $PrBaCo_{1.9}Hf_{0.1}O_{6-\delta}$ (PBCHf10) powders, followed by sintering at temperatures of 1200°C and 1150°C, respectively. Employing Archimede’s drainage method, it was determined that the relative density of the sintered samples exceeds 97%, fulfilling the requisite for subsequent measurement of transport properties.

Fabrication of Symmetrical Cells. $Sm_{0.2}Ce_{0.8}O_{1.9}$ (SDC) pellets were crafted through uniaxially dry pressing of commercially available SDC powder (Fuel Cell Materials, US). Subsequently, the pressed pellet underwent a sintering process at 1450°C for 5 hours, resulting in a relative density of approximately 98%. Similarly, BZCYYb1711 pellets were synthesized utilizing BZCYYb1711 powder, with the incorporation of a 1 wt% NiO additive. For the oxygen electrodes, deposition onto the electrolyte surface was achieved using a screen-printing technique. A slurry comprising oxygen electrode powder and α-terpineol (6% ethyl cellulose) with a weight ratio of 0.7: 1 was utilized. The slurry was printed on both sides of the electrolyte, followed by drying at 70°C for 30 minutes, and subsequent calcination at 950°C for 2 hours to form the porous oxygen electrode layer.

Fabrication of Single Cells. The Ni-BSCYb172 fuel electrode-supported single cells were meticulously crafted through co-tape casting and co-sintering techniques. Initially, the BSCYb172 electrolyte layer, NiO-BSCYb172 functional layer, and NiO-BSCYb172 supporting layer were sequentially cast onto the Mylar film. Subsequently, by co-sintering was performed at 1400°C for 5 hours in the presence of air. The fabrication process for the oxygen electrode layer mirrored that of symmetrical cells.

Testing Conditions of Single Cells. For electrochemical performance testing, single cells were mounted on alumina supporting tubes using Ceramabond 552 (Aremco). The fuel electrode was fed with 20 sccm humidified H_2 (3% water vapor pressure) and the oxygen electrode was exposed to 100 sccm humidified air (3%, 30% water vapor pressure). Steam concentration was regulated by a humidification system (Fuel Cell Technologies, Inc.). Cell performance was evaluated using an Arbin multi-channel electrochemical testing system (MSTAT). Electrochemical impedance spectra (EIS) were acquired with a Solartron 1255 HF frequency response analyzer interfaced with an EG&G PAR potentiostat model 273 A, utilizing an AC amplitude of 10 mV in the frequency range from 100kHz to 0.01 Hz. Distribution of Relaxation Times (DRT) analysis was conducted with a homemade MATLAB script.

Characterizations. XRD measurements were conducted using a Panalytical X'Pert Pro Alpha-1, equipped with CuKα1 radiation and XCelerator detector, with the 20-80° range. The cross-sectional microstructure and morphology of the powders and cells were examined using a scanning electron microscope (SEM, Hitachi SU8010). Transmission electron microscopy (TEM, JEOL 4000EX) was employed to scrutinize the microstructure and morphology of the PBCHf10 electrodes. X-ray photoelectron spectroscopy (XPS) was performed on a Thermo K Alpha for excitation and a 180°, double-focusing, hemispherical analyzer with a 128-channel detector and 10-400 μm spot size. To analyze the distribution of oxygen-related species within the bulk material, ion etching was carried out prior to XPS analysis. The ion etching process utilized an EX06 Ion Source, which operated at a high voltage of 3000 eV for a period of 180 seconds. Thermogravimetric analysis (TGA) tests were carried out using a NETZSCH Jupiter STA449 F3. In-situ XRD measurements were conducted with a BRUKER D8 PHASER, utilizing CuKα radiation under two atmospheres: air, and wet air (air with 3% water vapor pressure). Temperature ranges spanned 50 to 700°C, with increments of 50°C.

Determination of Mechanical and Chemical Compatibility. The dilatometer investigations (NETZSCH DIL402C, Germany) were implemented with PBCHf10 strip sample to obtain the thermal expansion coefficient (TEC), evaluating the mechanical compatibility between PBCHf10 and electrolyte. To evaluate the chemical compatibility between PBCHf10 and electrolyte, powders of PBCHf10 were physically mixed with SDC or BZCYYb1711, respectively. These mixtures were then calcinated at 950 °C for 2 hours. Post-calcination, XRD measurements were performed on the resulting powders to assess their chemical compatibility.

Determination of transport properties. The oxygen surface exchange coefficient (k_{Chem}) and chemical oxygen bulk diffusion coefficient (D_{Chem}) for PBCHf10 were determined using electrical conductivity relaxation (ECR) measurements, conducted between 550 and 650 °C utilizing a four-probe technique via Keithley-2700 instrument, and the electrical conductivity values are also collected. The experimental setup involved cyclically alternating the atmosphere between air and pure oxygen, thereby deriving normalized conductivity curves for both ORR and oxygen evolution reaction (OER). The k_{Chem} and D_{Chem} related to ORR and OER processes were extracted using a homemade MATLAB script, with results illustrated in.

Supplementary Notes

High-throughput Calculation. All high-throughput calculations were conducted employing density functional theory (DFT) within the Vienna ab initio simulation package (VASP)[1, 2]. The exchange-correlation effects in the Kohn-Sham equations were accounted for using the Perdew-Butke-Ernzerhof (PBE) functional under the generalized gradient approximation (GGA)[3]. Pseudopotential and U_{eff} values for each element were sourced from Supplementary Table 1, following recommendations from the Material Project[4]. The energy cutoff and convergence criteria were set as 400 eV and 4×10^{-3} eV, respectively. Electronic optimization utilized the RMM-DIIS algorithm, while ionic optimization employed the conjugate gradient method.

For the 4455 distinct B-site doping and 184 A-site doping candidates, their most energetically favorable atomic distributions were determined through Molecular Dynamics – Monte Carlo simulations, utilizing M3GNet as the interatomic potential[5, 6]. These simulations were executed at 298.15K using the Nose-Hoover thermostat in the NVT ensemble with a time step of 1 femtosecond, implemented via the Large-scale Atomic/Molecular Massively Parallel Simulator (LAMMPS). Every 1000 steps, a Monte Carlo swap was performed independently on the A-site and B-site elements, with acceptance of the swap determined by whether it reduced the total energy. The simulation continued until the element distribution reached equilibrium and no longer changed. Structural relaxation and static calculation were performed successively for each material to obtain their DFT energy. Subsequently, accessing the Materials Projects database and applying the energy shift using the temperature and pressure dependence of the gas species, the E_{hull} value at oxygen electrode operation condition (T = 600 °C and $p(O_2)$ = 0.21 atm) was obtained using the energy derived from the static calculation[7]. The chemical potential of oxygen is defined as follows:

$$\mu_{O_2}(T,P) = E_{elec} + ZPE + \int C_p(O_2)dT - T * S(O_2) + k * T * \ln\left(\frac{P}{P^0}\right)$$

where E_{elec} is the calculated electronic energy, ZPE is the zero-point energy, $C_p(O_2)$ is the heat capacity available from NIST database, $S(O_2)$ is the entropy contribution available from NIST database, and the temperature (T) and partial pressure (P) were assumed to be 873.15K and 0.21 atm[8,9], respectively. For the state-of-the-art oxygen electrode shown in Fig. 1b, to align the stoichiometry of these benchmark materials with our screening model, we constructed bulk models of $La_{0.625}Sr_{0.375}Co_{0.1875}Fe_{0.8125}O_3$, $Ba_{0.5}Sr_{0.5}Co_{0.8125}Fe_{0.1875}O_3$, $Sm_{0.5}Sr_{0.5}CoO_3$, $BaCo_{0.375}Fe_{0.375}Zr_{0.125}Y_{0.125}O_3$, and $PrBa_{0.5}Sr_{0.5}Co_{1.5}Fe_{0.5}O_6$, as depicted in Fig.S9.

Theoretical Basis of Decomposition Analysis. The theoretical basis of decomposition analysis originates from the study of phase diagrams. To illustrate, we utilize the Co-O binary phase diagram (Fig. S6) at 0 K as a case study. The formation energy (E_F) of elements, Co (mp-102) and O_2 (mp-611836), is set as 0 eV/atom, while the E_F of compounds is determined by subtracting the energies of constituent elements in their standard states from the compound's energy, each multiplied by their respective stoichiometric coefficients. This metric elucidates the ease of compound formation from elements. By linking stable phases with the lowest E_F, such as CoO (mp-22408, $F\bar{4}3m$), Co_3O_4 (mp-1271793), and CoO_2 (mp-1400906), and considering the elements, we construct a convex hull, delineating stability boundaries. The thermodynamic stability of compounds beyond the convex hull is described by the energy above the convex hull (E_{hull}) value. For instance, CoO (mp-19275, I4/mmm), with an E_{hull} of 0.132 eV/atom, may undergo a phase transformation to $F\bar{4}3m$, reducing its E_{hull}. While Co_7O_{12} (mp-2215229) could decompose, yielding Co_3O_4 (mp-1271793), and CoO_2 (mp-1400906) with fractions of 0.33 and 0.67. The energy disparity between compounds and their decomposition products signifies decomposition tendencies, while the fractions of each decomposition products provide quantitative insights. Leveraging our script "DecompositionAnalysis.py" yields decomposition products alongside their fractions, furnishing both energetic and quantitative details for potential phase transformations or decompositions.

To validate the universal applicability of DA method, it was applied to the state-of-the-art oxygen electrode, such as LSCF, BSCF, SSC, BCFZY, and PBSCF. For LSCF, the predominant decomposition product, $LaFeO_3$, with the lowest E_F of -2.226 eV/atom and highest fraction of 0.625, fosters a propensity for the separation of La and Sr, offering a plausible explanation for the noted Sr segregation in LSCF[8], as illustrated in Fig. S10a. In the case of BSCF, decomposition into $BaCoO_3$ (E_F = -1.426 eV/atom, $P6_3/mmc$) at a fraction of 5/12, intimates a possible phase transition from a corner-shared cubic phase to a face-shared hexagonal phase[9], highlighted in Fig. S10b. Leveraging these characteristics, Liu et al. developed a synergistic cubic-hexagonal dual-phase oxygen electrode for PCECs by modulating the stoichiometric ratio of the A-site/B-site in BSCF[10]. SSC, PBSCF, and BCFZY, with their relatively low E_{hull} values (0.183, 0.261, 0.345 eV/atom, respectively) as shown in Fig. S10 c-e, exhibit relatively good stability. However, SSC is susceptible to forming a secondary phase Sm_2O_3, particularly when synthesized via the sol-gel method[11] – a tendency confirmed by the identified decomposition product Sm_2O_3 (E_F = -3.236 eV/atom) with a fraction of 0.25. BCFZY notably prefers the formation of $BaZrO_3$ (E_F = -3.016 eV/atom) and Y_2O_3 (E_F = -3.286 eV/atom), given the substantial E_F differential between these decomposition products and BCFZY (E_F = -1.46 eV/atom). Decomposition analysis of PBSCF reveals a notable decomposition tendency, leading to the formation of Pr_2O_3 (E_F = -2.986 eV/atom). When directly compared, PBC emerges as superior in thermodynamic stability, evidenced by a much lower E_{hull} of 0.134 eV/atom. This is further corroborated by the insignificant disparity observed between the E_F of PBC and its decomposition products, as illustrated in Fig. S10f.

Further examination of the DA theory was carried out on a spectrum of PBC-derived materials scrutinizing its precision. Fifteen distinct PBC-derived materials, doped with a variety of elements (M = Bi, Ce, Ga, Hf, In, Mo, Nb, Sb, Sc, Sn, Ta, W, Y, Yb, and Zr) at a 6.25% doping content, were synthesized via the sol-gel method and analyzed through X-ray diffraction (XRD), as displayed in Fig. S11. These materials are denoted as $PrBaCo_{1.875}M_{0.125}O_{5+\delta}$ or succinctly PBCM0625. To delineate the secondary phases, the XRD patterns of pristine PBC were juxtaposed with each material for straightforward comparison. Secondary phases for each material were also identified, with their XRD data sourced from Inorganic Crystal Structure Database (ICSD)[12]. Notably, among these 15 PBC-derived materials, $PrBaCo_{1.875}Sc_{0.125}O_{5+\delta}$ and $PrBaCo_{1.875}Y_{0.125}O_{5+\delta}$ exhibited no secondary phases, indicating PBC's tolerance for Sc and Y doping. The DA method accurately forecasted the emergence of secondary phases in 10 of these materials, as demonstrated in Fig. S12. Nonetheless, anomalies were observed on Sb, Sn, and Ta. $PrBaCo_{1.875}Sb_{0.125}O_{5+\delta}$ and $PrBaCo_{1.875}Sn_{0.125}O_{5+\delta}$ unexpectedly formed $BaPrO_3$ (E_F = -2.266 eV/atom, E_{hull} = 0.11 eV/atom), while $PrBaCo_{1.875}Ta_{0.125}O_{5+\delta}$ notably decomposed by producing $Ba_5Co_5O_{14}$ (E_F = -1.443 eV/atom, E_{hull} = 0.01 eV/atom). It is essential to acknowledge that DA's sensitivity to phase diagrams mirrors that of the E_{hull} theory, as DA fundamentally stems from it. Both $BaPrO_3$ and $Ba_5Co_5O_{14}$, being identified as metastable structures in the current database, eluded detection for potential decomposition during the DA process.

The efficacy of DA is unequivocally proved through its successful application to state-of-the-art oxygen electrodes and its precision in discerning subtle differences among a variety of PBC-derived materials. The synergy of E_{hull} theory and DA method substantially augments our understanding of perovskite oxide materials. For materials with relatively low E_{hull} values, DA provides intricate insights into potential decomposition tendencies, thereby preventing pseudo-stable materials screened within a vast chemical space. Conversely, for materials with relatively high E_{hull} values, DA identifies detailed decomposed products, offering precise guidance for the development of self-generated composite electrodes. In our research, DA facilitates a comprehensive assessment of potential decomposition products across all 4455 materials, providing an extensive blueprint for perovskite materials design. This approach entails evaluating over 30,000 diverse materials, a fifth of the entire Materials Project database, to construct the potential energy surface, delivering invaluable insights into the thermodynamic stability and potential decomposition behaviors. All scripts are accessible via https://github.com/XueyuHu/HighthroughputCalculation/.

Detailed DFT-based Calculation. All spin-polarized calculations were conducted using the DFT method with the VASP. The PAW method was employed, incorporating atomic configurations for Hf([Kr]$5p^6 5d^2 6s^2$), Pr([Kr]$5s^2 5p^6 6s^2$) Ba([Kr]$5s^2 5p^6 6s^2$), Co([Ne]$3d^7 4s^2$), O([He]$2s^2 2p^4$), and H($1s^1$) to accurately depict interactions between ionic core electrons and valence electrons. To account for exchange correlations in the Kohn-Sham equations, the GGA with PBC functional was utilized. Additionally, GGA+U with U_{eff} = 3.3 eV was incorporated to capture correlated electrons within the Co 3d-orbital [13]. The energy cutoff and convergence criteria were set at 520 eV and 10^{-7} eV, respectively, ensuring computational accuracy. Structures relaxation was pursued until the force on each atom was below 0.02 eV $Å^{-1}$, employing the RMM-DIIS algorithm for electronic optimization and conjugate gradient for optimization.

For the pristine $PrBaCo_2O_{5+\delta}$, a supercell of $PrBaCo_2O_6$ with dimensions $2a \times 2a \times 2a$ was constructed (Fig. S31), comprising 4 Pr, 4 Ba, 8 Co, and 24 O atoms to delineate its properties. To assess the activity of $PrBaCo_2O_{5+\delta}$, low-index (001) surfaces were cleaved with BO_2 surface terminated[14]. All potential BO_2-terminated (001) surfaces were evaluated, with the most energetically favorable one selected for further analysis. A similar procedure was applied to $Pr_{1.125}Ba_{0.875}Co_2O_6$, and $BaHfO_3$ to characterize Pr-excessive PBC and $BaHfO_{3-\delta}$. In exploring the catalytic behavior of the PBC-BHO interface, a hybrid PBC-BHO structure was constructed by concatenating PBC and BHO. Various configurations were considered and the most energetically favorable structure was identified for in-depth analysis (Fig. S31). Similarly, low-index (001) surface was cleaved with BO_2 surface termination (Fig. S28). Vacuum layers of 15 Å were introduced to mitigate inter-slab interactions between neighboring cells, while dipole correction was applied to maintain computational accuracy.

The detailed pathways of oxygen reduction reaction (ORR) and proton-involved oxygen reduction reaction (PI-ORR) were meticulously simulated utilizing the climbing image nudged elastic band (CI-NEB) method[15]. For this analysis, three to five intermediate images were employed, with forces minimized to 0.02 eV $Å^{-1}$. Microkinetic analysis, grounded in transition state theory, was performed to validate the calculations[16]. Additionally, Bader charge analysis was conducted to illustrate charge transfer information. Systematically exploring all feasible elementary steps for ORR[14], we extensively discussed the most favorable pathways.

Ab initio molecular dynamics (AIMD) simulations were carried out using VASP, with the Nose-Hoover thermostat implemented in the NVT ensemble. Machine learning force fields (MLFFs) were developed for PBC and BHO at 400, 500, and 600 °C, respectively, incorporating proton in advance, with a training time of 10 ps. Subsequently, these well-established MLFFs were utilized for extended simulation duration of 100 ps (Fig. S34). The mean squared displacement (MSD), vibrational density of states (VDOS), and protonic diffusion coefficient (D_{H}) were computed using vaspkit[17]. As illustrated in Fig. S35, two distinct vibrational modes emerge at 783 cm^{-1} and 3347 cm^{-1}, signifying the reorientation and hopping of protons during the simulation process. Additionally, the trajectories of protons in both PBC and BHO are depicted in Fig. S36.

Experimental Assessment on Catalytic Activity for ORR. The integration of Pr-rich PBC and BHO as composite electrode has resulted in exceptional ORR activity. This significant achievement is evidenced by comprehensive electrochemical impedance spectrum (EIS) measurements conducted with symmetrical cell configurations of PBC(Hf)/SDC/PBC(Hf), as illustrated in Fig. S15. The substitution of Hf for Co in PBC led to a significant enhancement in catalytic activity. Specifically, at 600 °C, the polarization resistance (R_p) exhibited remarkable decreases from 0.152 Ω cm^2 for pristine PBC to 0.142 and 0.073 Ω cm^2 for PBCHf05 and PBCHf10, respectively. However, further increasing on Hf doping content beyond x = 0.1 diminished the electrochemical performance, with R_p slightly rising to 0.084 and 0.092 Ω cm^2 for PBCHf15 and PBCHf20, respectively. A V-shape relationship is observed for both R_p and its corresponding activation energy (E_a), with PBCHf10 displaying the optimal chemical composition, thus demonstrating superior ORR/OER performance (Fig. S16). This is evidenced by the lowest recorded R_p of 0.022, 0.038, 0.073, 0.166 and 0.400 Ω cm^2 at temperatures 700, 650, 600, 550, and 500 °C, respectively, alongside the lowest E_a of 0.95 eV. This performance marks a significant advancement over existing state-of-the-art electrodes, as highlighted in Fig. S17.

Distribution of Relaxation Time (DRT) analysis was utilized to elucidate the mechanisms driving ORR activities. At an operating temperature of 600 °C, two distinct peaks were identified, each corresponding to separate elementary steps in the ORR/OER process, as detailed in Fig. S18. The electrochemical process with the higher frequency peak was determined to be the primary contributor to the overall R_p. To identify the electrochemical step corresponding to each peak, EIS tests were performed with PBCHf10/SDC/PBCHf10 symmetrical cells at 600 °C across various oxygen partial pressures (Fig. S20a). Subsequent DRT analysis was carried out, detailed in Fig. S20b. Consistent with results observed under ambient air (Fig. S18), two distinct peaks were identified, signifying two separate elementary steps contributing to the overall ORR. The high-frequency peak, which has a larger area, constitutes the majority part of the total R_p. The area under both peaks were integrated to ascertain their respective contributions to the total R_p. An evident reduction in both peaks was observed as the oxygen partial pressure increased, leading to the application of linear fitting to determine the reaction order (n) for each step, based on the relationship ln $(R_p) \propto \mathrm{n}\ln(pO_2)$ (Fig. S20c). The electrochemical process associated with the high-frequency peak has a reaction order of 0.36, which is assigned to the oxygen dissociation process (n = 0.375). On the other hand, the process associated with the low frequency peak has a reaction order of 0.98, indicating that it corresponds to oxygen transport process (n = 1)[18]. These analyses indicate that the doping with Hf significantly enhanced the rate of oxygen dissociation process in PBCHf10, the critical rate-determining step in ORR/OER. Further DFT-based calculations were performed to gain critical insight into the mechanism of the exceptionally high ORR activities of PBCHf10. Three configurations were constructed, PBC, Pr-rich PBC and PBC-BHO, to simulate the pristine PBC, the primary phase of PBCHf10, and the interface of PBC-BHO within PBCHf10, respectively, as illustrated in Supplementary Fig. 31. Through projected density of states (PDOS) analysis, the p-band center value for the hybrid PBC-BHO structure was found to be -1.52 eV, in contrast to -2.13 eV for PBC and -1.81 eV for Pr-rich PBC (Supplementary Fig. 19), suggesting the enhanced oxygen dissociation process primarily due to the present of PBC-BHO interface[21]. Subsequently, a comprehensive investigation of the ORR pathway on both pristine PBC and hybrid PBC-BHO models was then undertaken, focusing on the (001) BO_2-terminated surface for its significant catalytic activity contribution (Fig. S28)[14]. The investigation comprehensively captured all relevant configurations encountered during the ORR process, which are summarized in Fig. 4, Figs. S37 and S39. First, in the pristine PBC case, the surface's inherent oxygen vacancy (denoted as $V_{O,\text{surf}}^{\cdot\cdot}$) creates a coordinatively unsaturated environment for oxygen molecules ($O_{2,\text{gas}}$) to adsorb, facilitating the formation of superoxide species, $* \, (O_{\text{I}}^{q\,\text{I}} \ldots O_{\text{II}}^{q\,\text{II}})$,

$$V_{O,\text{surf}}^{\cdot\cdot} + O_{2,\text{gas}} + q_{\text{ads}}e' \rightarrow * \, (O_{\text{I}}^{q_{\text{I}}} \ldots O_{\text{II}}^{q_{\text{II}}}) \tag{1}$$

This adsorption process is quantified by an adsorption energy of -0.237 eV on the (001) BO$_2$-terminated PBC surface. The Bader charge analysis for the oxygen atoms involved, O_{I} and O_{II} (denoted as individual oxygen atom of a single oxygen molecule), yields charges of q_{I} = 0.32 e and q_{II} = 0.48 e, respectively, as illustrated in Fig. S37. Following adsorption, the dissociation reaction occurs,

$$* \, (O_{\text{I}}^{q_{\text{I}}} \ldots O_{\text{II}}^{q_{\text{II}}}) + q_{\text{diss}}e' \rightarrow * \, (O_{\text{I}}^{q_{\text{I}}'}) + O_{\text{II},O,\text{surf}}^{q_{\text{II}}'} \tag{2}$$

Here, the O_{II} integrates into the vacancy site, becoming $O_{\text{II},O,\text{surf}}^{q_{\text{II}}'}$ (with its Bader charge rising to $q_{\text{II}}' =$ 0.94 e), denoting a surface-located lattice oxygen, distinct from bulk lattice oxygen ($O_{O,\text{bulk}}^{\times}$, with Bader charge of 1.10 e). The remaining oxygen atom O_{I}, now identified as a peroxide species $* \, (O_{\text{I}}^{q_{\text{I}}'})$, retains a Bader charge of $q_{\text{I}}' =$ 0.47 e. The dissociation reaction's E_a is calculated to be 0.74 eV. Subsequent to the dissociation, oxygen transport from the surface to bulk,

$$O_{\text{II},O,\text{surf}}^{q_{\text{II}}'} + V_{O,\text{bulk}}^{\cdot\cdot} + q_{\text{trans}}e' \rightarrow V_{O,\text{surf}}^{\cdot\cdot} + O_{O,\text{bulk}}^{\times} \tag{3}$$

This stage sees the O_{II} atom moving deeper into the bulk, with the emergence of new surface vacancy ($V_{O,\text{surf}}^{\cdot\cdot}$). The peroxide species $* \, (O_{\text{I}}^{q_{\text{I}}'})$ then undergoes an incorporation reaction,

$$* \left(O_{\text{I}}^{q_{\text{I}}'}\right) + V_{O,\text{surf}}^{\cdot\cdot} + q_{\text{incorp}}e' \rightarrow O_{\text{I},O,\text{surf}}^{q_{\text{I}}''} \tag{4}$$

During this process, the Bader charge of O_{I} escalates from $q_{\mathrm{I}}' = 0.51\mathrm{e}$ to $q_{\mathrm{I}}'' = 0.98\mathrm{e}$, with E_a of 0.66 eV. This cycle concludes with the regeneration of a new surface vacancy, marking the completion of a ORR cycle for one oxygen molecule[14]. From the DFT-calculations, the dissociation reaction emerges as the rate-determining step, corroborated by charge variations and aligning with prior DRT analysis. On the other hand, self-generated BHO particles, forming the PBC-BHO interface on PBCHf10, significantly enhances the ORR kinetics with reduced E_a for oxygen dissociation (0.64 eV) and incorporation (0.49 eV). This is evidenced by an improved oxygen adsorption property at the interface, boasting the adsorption energy to -0.427 eV. Moreover, charge distribution difference analysis for the (001) BO_2-terminated surface of both PBC and hybrid PBC-BHO, with superoxide species adsorbed, underscores the enhanced oxygen-cobalt bonding in the hybrid structure (Fig. S38), featuring the higher amount of charges to the adsorbed oxygen with 0.929e for the hybrid, against 0.801e for pristine PBC. Chemical oxygen surface exchange coefficient (k_{Chem}) and the chemical oxygen bulk diffusion coefficient (D_{Chem}) were determined through ECR measurements (Supplementary Figs. 49 and 50), leading further support to our proposed mechanism for ORR. For PBCHf10, both k_{Chem} and D_{Chem} exhibited significant enhancements compared to pristine PBC (k_{Chem} = 7.5 E^{-5} cm s^{-1}, D_{Chem} = 8.0 E^{-6} cm^2 s^{-1} for PBCHf10; k_{Chem} = 4.1E^{-5} cm s^{-1}, D_{Chem} = 4.8 E^{-6} cm^2 s^{-1} for PBC at 600°C) [18]. These findings highlight the self-generated PBC-BHO interface's role in enhancing the ORR process's efficiency, outperforming pathways exclusive to PBC[19].

Theoretical Analysis on PI-OER. To gain deeper understanding about the proton-involved oxygen evolution reaction (PI-OER), the water electrolysis energy profile is determined for PBC surface and PBC-BHO interface, with the Gibbs free energy of each elementary step was calculated at 600°C with an applied voltage of 1.3 V. Vibration mode for all surface-adsorbed species were calculated to obtain the zero-energy potential and entropy corrections (Supplementary Table 6)[20]. The detailed description for each elementary step is provided[21, 22], with the proton denoted as H^+, transported via $OH_O^{\cdot}$ either through electrolyte or electrode.

Step E1: $H_2O \leftrightarrow * OH \ldots * H$ (5)

Step E2: $* OH + * H + e' \leftrightarrow * OH \ldots H^+$ (6)

Step E3: $* OH \leftrightarrow * O \ldots * H$ (7)

Step E4: $* O \ldots * H + e' \leftrightarrow * O + H^+$ (8)

Step E5: $* O + O_s^{\times} + e' \leftrightarrow * OO$ (9)

Step E6: $* OO + e' \leftrightarrow V_O^{\cdot\cdot} + O_2$ (10)

Hence, the Gibbs free energy for each elementary step can be calculated as,

$$\Delta G_1 = E(* OH \ldots * H) - E(H_2O) + \Delta ZPE_1 - T\Delta S_1 \tag{11}$$

$$\Delta G_2 = E(* OH) + E(H^+) - E(* OH \ldots * H) + \Delta ZPE_2 - T\Delta S_2 - eU \tag{12}$$

$$\Delta G_3 = E(* O \ldots * H) - E(* OH) + \Delta ZPE_3 - T\Delta S_3 \tag{13}$$

$$\Delta G_4 = E(* O) + E(H^+) - E(* O \ldots * H) + \Delta ZPE_4 - T\Delta S_4 - eU \tag{14}$$

$$\Delta G_5 = E(* OO) - E(* O \ldots O_s^{\times}) + \Delta ZPE_5 - T\Delta S_5 - eU \tag{15}$$

$$\Delta G_6 = E(O_2) + E(V_O^{\cdot\cdot}) - E(* OO) + \Delta ZPE_6 - T\Delta S_6 - eU \tag{16}$$

The calculated thermodynamics values for H_2, O_2 , and H_2O were compared with data extracted from NIST-JANAF thermochemical tables to validate their accuracy and reliability[23].

For PBC, the rate-determining step was identified as the transformation of $* OH \ldots * H + e'$ into $* OH + H^+$, with an observed energy barrier of 1.28 eV (Fig. S53). In contrast, the hybrid PBC-

BHO maintained the same rate-determinant step but exhibited a significantly lower energy barrier of 1.07 eV, underscoring the catalytic activity enhancement afforded by the PBC-BHO interface.

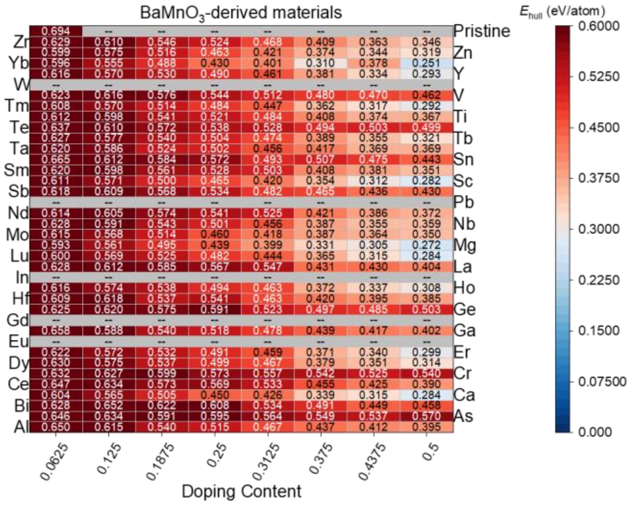

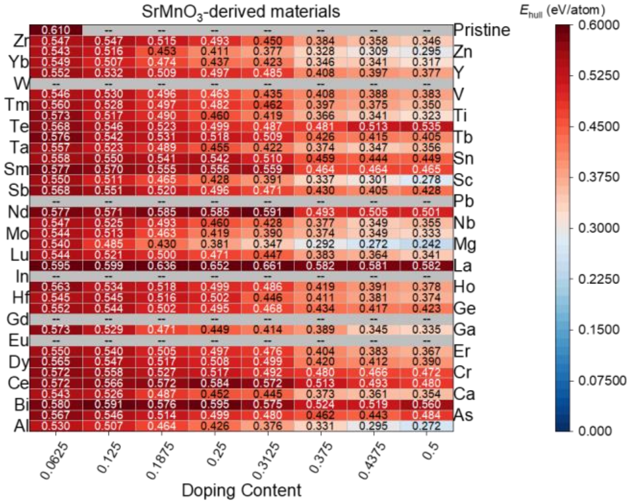

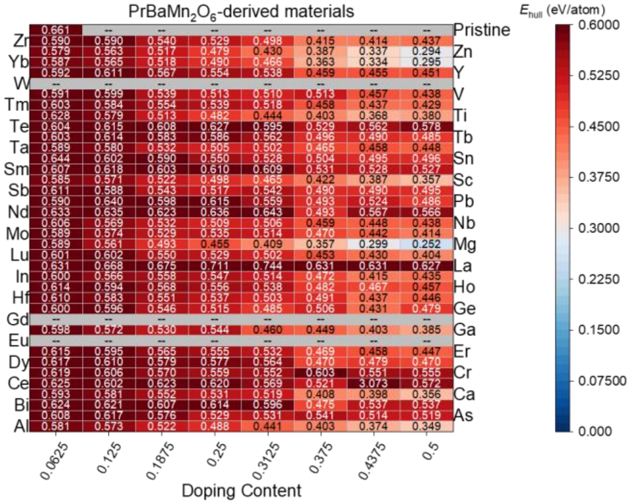

Figure S1. Summary of E_{hull} values for $BaMnO_3$, $SrMnO_3$, and $PrBaMn_2O_6$-derived materials.

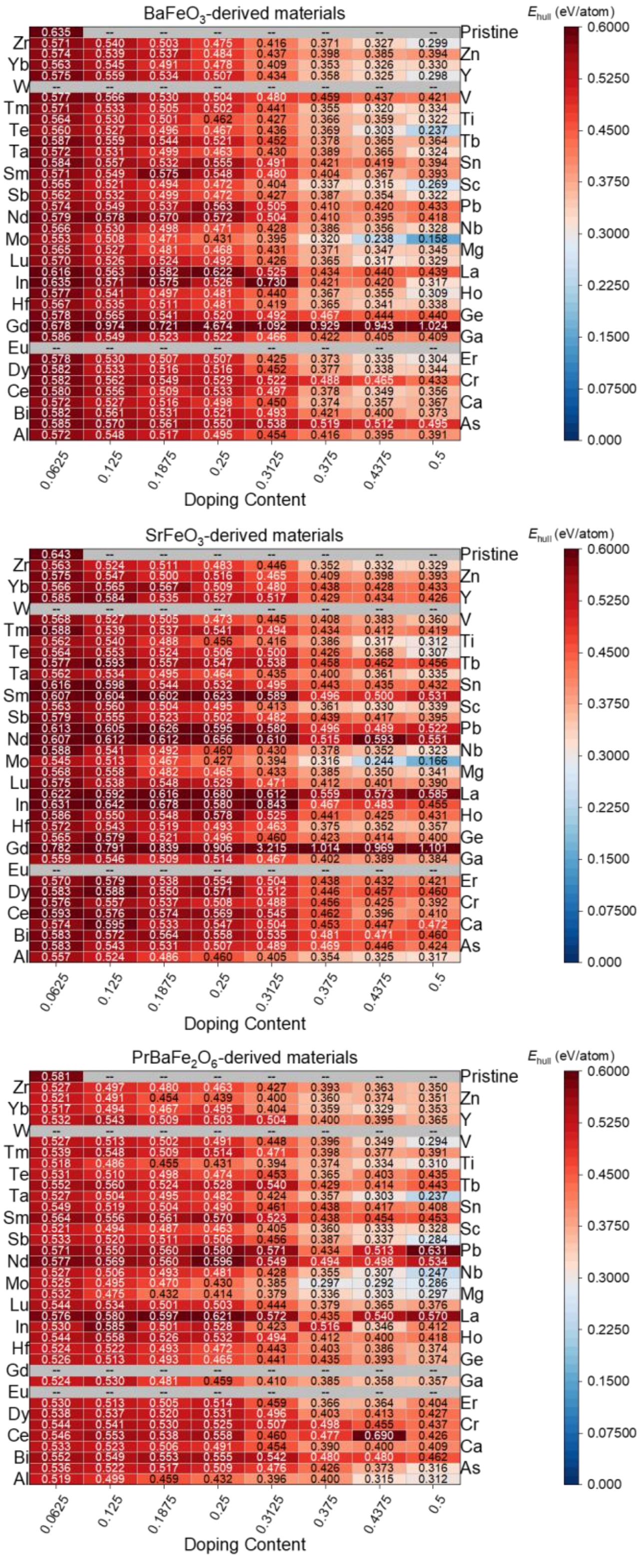

BaFeO$_3$-derived materials

	0.0625	0.125	0.1875	0.25	0.3125	0.375	0.4375	0.5
Pristine	0.635	--	--	--	--	--	--	--
Zr	0.571	0.540	0.503	0.475	0.416	0.371	0.327	0.299
Zn	0.574	0.539	0.537	0.484	0.437	0.398	0.385	0.394
Yb	0.563	0.545	0.491	0.478	0.409	0.353	0.326	0.330
Y	0.575	0.559	0.534	0.507	0.434	0.358	0.325	0.298
W	--	--	--	--	--	--	--	--
V	0.577	0.566	0.530	0.504	0.480	0.459	0.437	0.421
Tm	0.571	0.533	0.505	0.502	0.441	0.355	0.320	0.334
Ti	0.564	0.530	0.501	0.462	0.427	0.366	0.359	0.322
Te	0.560	0.527	0.496	0.467	0.436	0.369	0.303	0.237
Tb	0.587	0.559	0.544	0.521	0.452	0.378	0.365	0.364
Ta	0.572	0.531	0.499	0.463	0.430	0.389	0.365	0.324
Sn	0.584	0.557	0.532	0.555	0.491	0.421	0.419	0.394
Sm	0.571	0.549	0.575	0.548	0.480	0.404	0.367	0.393
Sc	0.565	0.521	0.494	0.472	0.404	0.337	0.315	0.269
Sb	0.562	0.532	0.499	0.472	0.427	0.387	0.354	0.322
Pb	0.574	0.549	0.537	0.563	0.505	0.410	0.420	0.433
Nd	0.579	0.578	0.570	0.572	0.504	0.410	0.395	0.418
Nb	0.566	0.530	0.498	0.471	0.428	0.386	0.356	0.328
Mo	0.553	0.508	0.471	0.431	0.395	0.320	0.238	0.158
Mg	0.565	0.527	0.481	0.468	0.431	0.371	0.347	0.345
Lu	0.570	0.526	0.524	0.492	0.426	0.365	0.317	0.329
La	0.616	0.563	0.582	0.622	0.525	0.434	0.440	0.439
In	0.635	0.571	0.575	0.526	0.730	0.421	0.420	0.317
Ho	0.577	0.541	0.497	0.481	0.440	0.367	0.355	0.309
Hf	0.567	0.535	0.511	0.481	0.419	0.365	0.341	0.338
Ge	0.578	0.565	0.541	0.520	0.492	0.467	0.444	0.440
Gd	0.678	0.974	0.721	4.674	1.092	0.929	0.943	1.024
Ga	0.586	0.549	0.523	0.522	0.466	0.422	0.405	0.409
Eu	--	--	--	--	--	--	--	--
Er	0.578	0.530	0.507	0.507	0.425	0.373	0.335	0.304
Dy	0.582	0.533	0.516	0.516	0.452	0.377	0.338	0.344
Cr	0.582	0.562	0.549	0.529	0.522	0.488	0.465	0.433
Ce	0.580	0.556	0.509	0.533	0.497	0.378	0.349	0.356
Ca	0.572	0.527	0.516	0.498	0.450	0.374	0.357	0.367
Bi	0.582	0.561	0.531	0.521	0.493	0.421	0.400	0.373
As	0.585	0.570	0.561	0.550	0.538	0.519	0.512	0.495
Al	0.572	0.548	0.517	0.495	0.454	0.416	0.395	0.391

SrFeO$_3$-derived materials

	0.0625	0.125	0.1875	0.25	0.3125	0.375	0.4375	0.5
Pristine	0.643	--	--	--	--	--	--	--
Zr	0.563	0.524	0.511	0.483	0.446	0.352	0.332	0.329
Zn	0.575	0.547	0.500	0.516	0.465	0.409	0.398	0.393
Yb	0.566	0.565	0.567	0.509	0.480	0.438	0.428	0.433
Y	0.585	0.584	0.535	0.527	0.517	0.429	0.434	0.426
W	--	--	--	--	--	--	--	--
V	0.568	0.527	0.505	0.473	0.445	0.408	0.383	0.360
Tm	0.588	0.539	0.537	0.541	0.494	0.434	0.412	0.419
Ti	0.562	0.540	0.488	0.456	0.416	0.386	0.317	0.312
Te	0.564	0.553	0.524	0.506	0.500	0.426	0.368	0.307
Tb	0.577	0.593	0.557	0.547	0.538	0.458	0.462	0.456
Ta	0.562	0.534	0.495	0.464	0.435	0.400	0.361	0.335
Sn	0.616	0.598	0.544	0.532	0.495	0.443	0.435	0.432
Sm	0.607	0.604	0.602	0.623	0.589	0.496	0.500	0.531
Sc	0.563	0.560	0.504	0.495	0.413	0.361	0.330	0.339
Sb	0.579	0.555	0.523	0.502	0.482	0.439	0.417	0.395
Pb	0.613	0.605	0.626	0.595	0.580	0.496	0.489	0.522
Nd	0.607	0.612	0.612	0.656	0.610	0.515	0.593	0.551
Nb	0.588	0.541	0.492	0.460	0.430	0.378	0.352	0.323
Mo	0.545	0.513	0.467	0.427	0.394	0.316	0.244	0.166
Mg	0.568	0.558	0.482	0.465	0.433	0.385	0.350	0.341
Lu	0.575	0.538	0.548	0.529	0.471	0.412	0.401	0.390
La	0.622	0.592	0.616	0.680	0.612	0.559	0.573	0.585
In	0.631	0.642	0.678	0.580	0.843	0.467	0.483	0.455
Ho	0.586	0.550	0.548	0.578	0.525	0.441	0.425	0.431
Hf	0.572	0.543	0.519	0.493	0.463	0.375	0.352	0.357
Ge	0.565	0.579	0.521	0.496	0.460	0.423	0.414	0.400
Gd	0.782	0.791	0.839	0.906	3.215	1.014	0.969	1.101
Ga	0.559	0.546	0.509	0.514	0.467	0.402	0.389	0.384
Eu	--	--	--	--	--	--	--	--
Er	0.570	0.579	0.538	0.554	0.504	0.438	0.432	0.421
Dy	0.583	0.588	0.550	0.571	0.512	0.446	0.457	0.460
Cr	0.576	0.557	0.537	0.508	0.488	0.456	0.425	0.392
Ce	0.593	0.576	0.574	0.569	0.545	0.462	0.396	0.410
Ca	0.574	0.595	0.533	0.547	0.504	0.453	0.447	0.472
Bi	0.583	0.572	0.564	0.558	0.535	0.481	0.471	0.460
As	0.583	0.543	0.531	0.507	0.489	0.469	0.446	0.424
Al	0.557	0.524	0.486	0.460	0.405	0.354	0.325	0.317

PrBaFe$_2$O$_6$-derived materials

	0.0625	0.125	0.1875	0.25	0.3125	0.375	0.4375	0.5
Pristine	0.581	--	--	--	--	--	--	--
Zr	0.527	0.497	0.480	0.463	0.427	0.393	0.363	0.350
Zn	0.521	0.491	0.454	0.439	0.400	0.360	0.374	0.351
Yb	0.517	0.494	0.467	0.495	0.404	0.359	0.329	0.353
Y	0.532	0.543	0.509	0.503	0.504	0.400	0.395	0.365
W	--	--	--	--	--	--	--	--
V	0.527	0.513	0.502	0.491	0.448	0.396	0.349	0.294
Tm	0.539	0.548	0.509	0.514	0.471	0.398	0.377	0.391
Ti	0.518	0.486	0.455	0.431	0.394	0.374	0.334	0.310
Te	0.531	0.510	0.498	0.474	0.453	0.365	0.403	0.435
Tb	0.552	0.560	0.524	0.528	0.540	0.429	0.414	0.443
Ta	0.527	0.504	0.495	0.482	0.424	0.357	0.303	0.237
Sn	0.549	0.519	0.504	0.490	0.461	0.438	0.417	0.408
Sm	0.564	0.556	0.561	0.570	0.523	0.438	0.454	0.453
Sc	0.521	0.494	0.487	0.463	0.405	0.360	0.333	0.328
Sb	0.533	0.520	0.511	0.506	0.456	0.387	0.337	0.284
Pb	0.571	0.550	0.560	0.580	0.571	0.434	0.513	0.631
Nd	0.577	0.569	0.560	0.596	0.549	0.494	0.498	0.534
Nb	0.527	0.506	0.493	0.481	0.428	0.355	0.307	0.247
Mo	0.525	0.495	0.470	0.430	0.385	0.297	0.292	0.286
Mg	0.532	0.475	0.432	0.414	0.379	0.336	0.303	0.297
Lu	0.544	0.534	0.501	0.503	0.444	0.379	0.365	0.376
La	0.576	0.580	0.597	0.621	0.572	0.435	0.540	0.570
In	0.530	0.585	0.501	0.528	0.423	0.516	0.346	0.412
Ho	0.544	0.558	0.526	0.532	0.494	0.412	0.400	0.418
Hf	0.524	0.522	0.493	0.472	0.443	0.403	0.386	0.374
Ge	0.526	0.513	0.493	0.465	0.441	0.435	0.393	0.374
Gd	--	--	--	--	--	--	--	--
Ga	0.524	0.530	0.481	0.459	0.410	0.385	0.358	0.357
Eu	--	--	--	--	--	--	--	--
Er	0.530	0.513	0.505	0.514	0.459	0.366	0.364	0.404
Dy	0.538	0.537	0.520	0.531	0.496	0.403	0.413	0.427
Cr	0.544	0.541	0.530	0.525	0.507	0.498	0.455	0.437
Ce	0.546	0.553	0.538	0.558	0.460	0.477	0.690	0.426
Ca	0.533	0.523	0.506	0.491	0.454	0.390	0.400	0.409
Bi	0.552	0.549	0.553	0.555	0.542	0.480	0.480	0.462
As	0.536	0.522	0.517	0.509	0.476	0.426	0.373	0.316
Al	0.519	0.499	0.459	0.432	0.396	0.400	0.315	0.312

Figure S2. Summary of E_{hull} values for BaFeO$_3$, SrFeO$_3$, and PrBaFe$_2$O$_6$-derived materials.

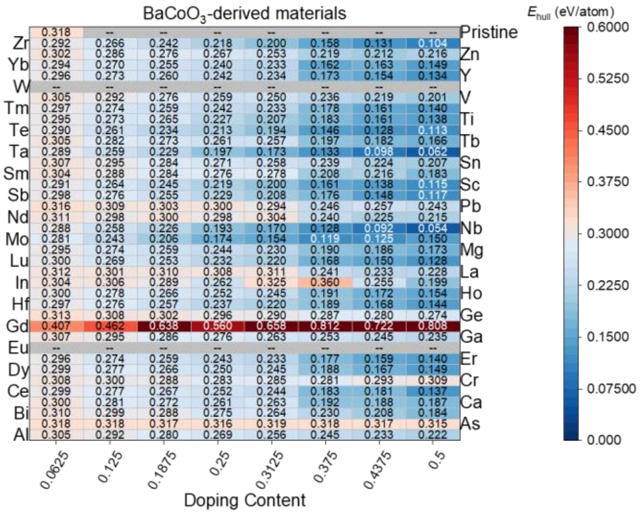

BaCoO$_3$-derived materials

	0.0625	0.125	0.1875	0.25	0.3125	0.375	0.4375	0.5
Pristine	0.318	--	--	--	--	--	--	--
Zr	0.292	0.266	0.242	0.218	0.200	0.158	0.131	0.104
Zn	0.302	0.286	0.276	0.267	0.253	0.219	0.212	0.216
Yb	0.294	0.270	0.255	0.240	0.233	0.162	0.163	0.149
Y	0.296	0.273	0.260	0.242	0.234	0.173	0.154	0.134
W	--	--	--	--	--	--	--	--
V	0.305	0.292	0.276	0.259	0.250	0.236	0.219	0.201
Tm	0.297	0.274	0.259	0.242	0.233	0.178	0.161	0.140
Ti	0.295	0.273	0.265	0.227	0.207	0.183	0.161	0.138
Te	0.290	0.261	0.234	0.213	0.194	0.146	0.128	0.113
Tb	0.305	0.282	0.273	0.261	0.257	0.197	0.182	0.166
Ta	0.289	0.259	0.229	0.197	0.173	0.133	0.098	0.062
Sn	0.307	0.295	0.284	0.271	0.258	0.239	0.224	0.207
Sm	0.304	0.288	0.284	0.276	0.278	0.208	0.216	0.183
Sc	0.291	0.264	0.245	0.219	0.200	0.161	0.138	0.115
Sb	0.298	0.276	0.255	0.229	0.208	0.176	0.148	0.117
Pb	0.316	0.309	0.303	0.300	0.294	0.246	0.257	0.243
Nd	0.311	0.298	0.300	0.298	0.304	0.240	0.225	0.215
Nb	0.288	0.258	0.226	0.193	0.170	0.128	0.092	0.054
Mo	0.281	0.243	0.206	0.174	0.154	0.119	0.125	0.150
Mg	0.295	0.274	0.259	0.244	0.230	0.190	0.186	0.173
Lu	0.300	0.269	0.253	0.232	0.220	0.168	0.150	0.128
La	0.312	0.301	0.310	0.308	0.311	0.241	0.233	0.228
In	0.304	0.306	0.289	0.262	0.325	0.360	0.255	0.199
Ho	0.300	0.278	0.266	0.252	0.245	0.191	0.172	0.154
Hf	0.297	0.276	0.257	0.237	0.220	0.189	0.168	0.144
Ge	0.313	0.308	0.302	0.296	0.290	0.287	0.280	0.274
Gd	0.407	0.462	0.638	0.560	0.658	0.812	0.722	0.808
Ga	0.307	0.295	0.286	0.276	0.263	0.253	0.245	0.235
Eu	--	--	--	--	--	--	--	--
Er	0.296	0.274	0.259	0.243	0.233	0.177	0.159	0.140
Dy	0.299	0.277	0.266	0.250	0.245	0.188	0.167	0.149
Cr	0.308	0.300	0.288	0.283	0.285	0.281	0.293	0.309
Ce	0.299	0.277	0.267	0.252	0.244	0.183	0.181	0.137
Ca	0.300	0.281	0.272	0.261	0.263	0.192	0.188	0.187
Bi	0.310	0.299	0.288	0.275	0.264	0.230	0.208	0.184
As	0.318	0.318	0.317	0.316	0.319	0.318	0.317	0.315
Al	0.305	0.292	0.280	0.269	0.256	0.245	0.233	0.222

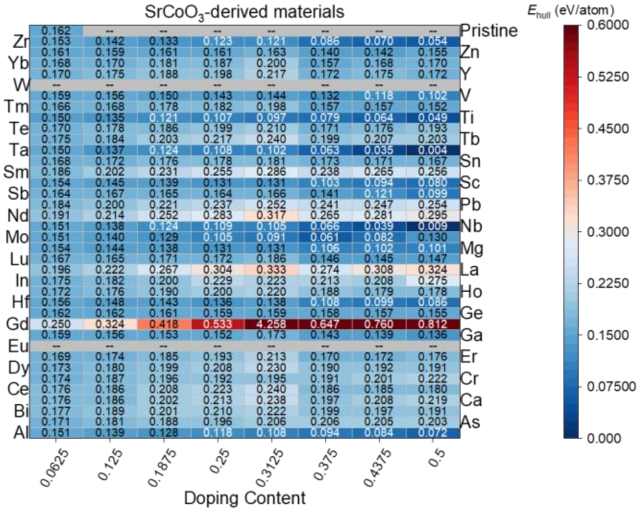

SrCoO$_3$-derived materials

	0.0625	0.125	0.1875	0.25	0.3125	0.375	0.4375	0.5
Pristine	0.162	--	--	--	--	--	--	--
Zr	0.153	0.142	0.133	0.123	0.121	0.086	0.070	0.054
Zn	0.161	0.159	0.161	0.161	0.163	0.140	0.142	0.155
Yb	0.168	0.170	0.181	0.187	0.200	0.157	0.168	0.170
Y	0.170	0.175	0.188	0.198	0.217	0.172	0.175	0.172
W	--	--	--	--	--	--	--	--
V	0.159	0.156	0.150	0.143	0.144	0.132	0.118	0.102
Tm	0.166	0.168	0.178	0.182	0.198	0.157	0.157	0.152
Ti	0.150	0.135	0.121	0.107	0.097	0.079	0.064	0.049
Te	0.170	0.178	0.186	0.199	0.210	0.171	0.176	0.193
Tb	0.175	0.184	0.203	0.217	0.240	0.199	0.207	0.203
Ta	0.150	0.137	0.124	0.108	0.102	0.063	0.035	0.004
Sn	0.168	0.172	0.176	0.178	0.181	0.173	0.171	0.167
Sm	0.186	0.202	0.231	0.255	0.286	0.238	0.265	0.256
Sc	0.154	0.145	0.139	0.131	0.131	0.103	0.094	0.080
Sb	0.164	0.167	0.165	0.164	0.166	0.141	0.121	0.099
Pb	0.184	0.200	0.221	0.237	0.252	0.241	0.247	0.254
Nd	0.191	0.214	0.252	0.283	0.317	0.265	0.281	0.295
Nb	0.151	0.138	0.124	0.109	0.105	0.066	0.039	0.009
Mo	0.151	0.140	0.129	0.105	0.091	0.061	0.082	0.130
Mg	0.154	0.144	0.138	0.131	0.131	0.106	0.102	0.101
Lu	0.167	0.165	0.171	0.172	0.186	0.146	0.145	0.147
La	0.196	0.222	0.267	0.304	0.333	0.274	0.308	0.324
In	0.175	0.182	0.200	0.229	0.223	0.213	0.208	0.275
Ho	0.172	0.176	0.190	0.200	0.220	0.188	0.179	0.178
Hf	0.156	0.148	0.143	0.136	0.138	0.108	0.099	0.086
Ge	0.162	0.162	0.161	0.159	0.159	0.158	0.157	0.155
Gd	0.250	0.324	0.418	0.533	4.258	0.647	0.760	0.812
Ga	0.159	0.156	0.153	0.152	0.173	0.143	0.139	0.136
Eu	--	--	--	--	--	--	--	--
Er	0.169	0.174	0.185	0.193	0.213	0.170	0.172	0.176
Dy	0.173	0.180	0.199	0.208	0.230	0.190	0.192	0.191
Cr	0.174	0.187	0.196	0.192	0.195	0.191	0.201	0.222
Ce	0.176	0.186	0.208	0.223	0.240	0.186	0.185	0.180
Ca	0.176	0.186	0.202	0.213	0.238	0.197	0.208	0.219
Bi	0.177	0.189	0.201	0.210	0.222	0.199	0.197	0.191
As	0.171	0.181	0.188	0.196	0.206	0.206	0.205	0.203
Al	0.151	0.139	0.128	0.118	0.108	0.094	0.084	0.072

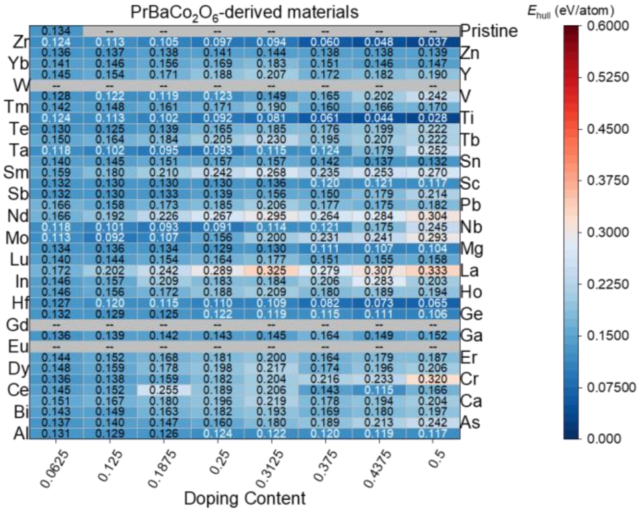

PrBaCo$_2$O$_6$-derived materials

	0.0625	0.125	0.1875	0.25	0.3125	0.375	0.4375	0.5
Pristine	0.134	--	--	--	--	--	--	--
Zr	0.124	0.113	0.105	0.097	0.094	0.060	0.048	0.037
Zn	0.136	0.137	0.138	0.141	0.144	0.138	0.138	0.139
Yb	0.141	0.146	0.156	0.169	0.183	0.151	0.146	0.147
Y	0.145	0.154	0.171	0.188	0.207	0.172	0.182	0.190
W	--	--	--	--	--	--	--	--
V	0.128	0.122	0.119	0.123	0.149	0.165	0.202	0.242
Tm	0.142	0.148	0.161	0.171	0.190	0.160	0.166	0.170
Ti	0.124	0.113	0.102	0.092	0.081	0.061	0.044	0.028
Te	0.130	0.125	0.139	0.165	0.185	0.176	0.199	0.222
Tb	0.150	0.164	0.184	0.205	0.230	0.195	0.207	0.222
Ta	0.118	0.102	0.095	0.093	0.115	0.124	0.179	0.252
Sn	0.140	0.145	0.151	0.157	0.157	0.142	0.137	0.132
Sm	0.159	0.180	0.210	0.242	0.268	0.235	0.253	0.270
Sc	0.132	0.130	0.130	0.130	0.136	0.120	0.121	0.117
Sb	0.132	0.130	0.133	0.139	0.156	0.150	0.179	0.214
Pb	0.166	0.158	0.173	0.185	0.206	0.177	0.175	0.182
Nd	0.166	0.192	0.226	0.267	0.295	0.264	0.284	0.304
Nb	0.118	0.101	0.093	0.091	0.114	0.121	0.175	0.245
Mo	0.113	0.092	0.107	0.156	0.200	0.231	0.241	0.293
Mg	0.134	0.136	0.134	0.129	0.130	0.111	0.107	0.104
Lu	0.140	0.144	0.154	0.164	0.177	0.151	0.155	0.158
La	0.172	0.202	0.242	0.289	0.325	0.279	0.307	0.333
In	0.146	0.157	0.209	0.183	0.184	0.206	0.283	0.203
Ho	0.146	0.156	0.172	0.188	0.209	0.180	0.189	0.194
Hf	0.127	0.120	0.115	0.110	0.109	0.082	0.073	0.065
Ge	0.132	0.129	0.125	0.122	0.119	0.115	0.111	0.106
Gd	--	--	--	--	--	--	--	--
Ga	0.136	0.139	0.142	0.143	0.145	0.164	0.149	0.152
Eu	--	--	--	--	--	--	--	--
Er	0.144	0.152	0.168	0.181	0.200	0.164	0.179	0.187
Dy	0.148	0.159	0.178	0.198	0.217	0.174	0.196	0.206
Cr	0.136	0.138	0.159	0.182	0.204	0.216	0.233	0.320
Ce	0.145	0.152	0.255	0.189	0.206	0.143	0.115	0.166
Ca	0.151	0.167	0.180	0.196	0.219	0.178	0.194	0.204
Bi	0.143	0.149	0.163	0.182	0.193	0.169	0.180	0.197
As	0.137	0.140	0.147	0.160	0.180	0.189	0.213	0.242
Al	0.131	0.129	0.126	0.124	0.122	0.120	0.119	0.117

Figure S3. Summary of E_{hull} values for BaCoO$_3$, SrCoO$_3$, and PrBaCo$_2$O$_6$-derived materials.

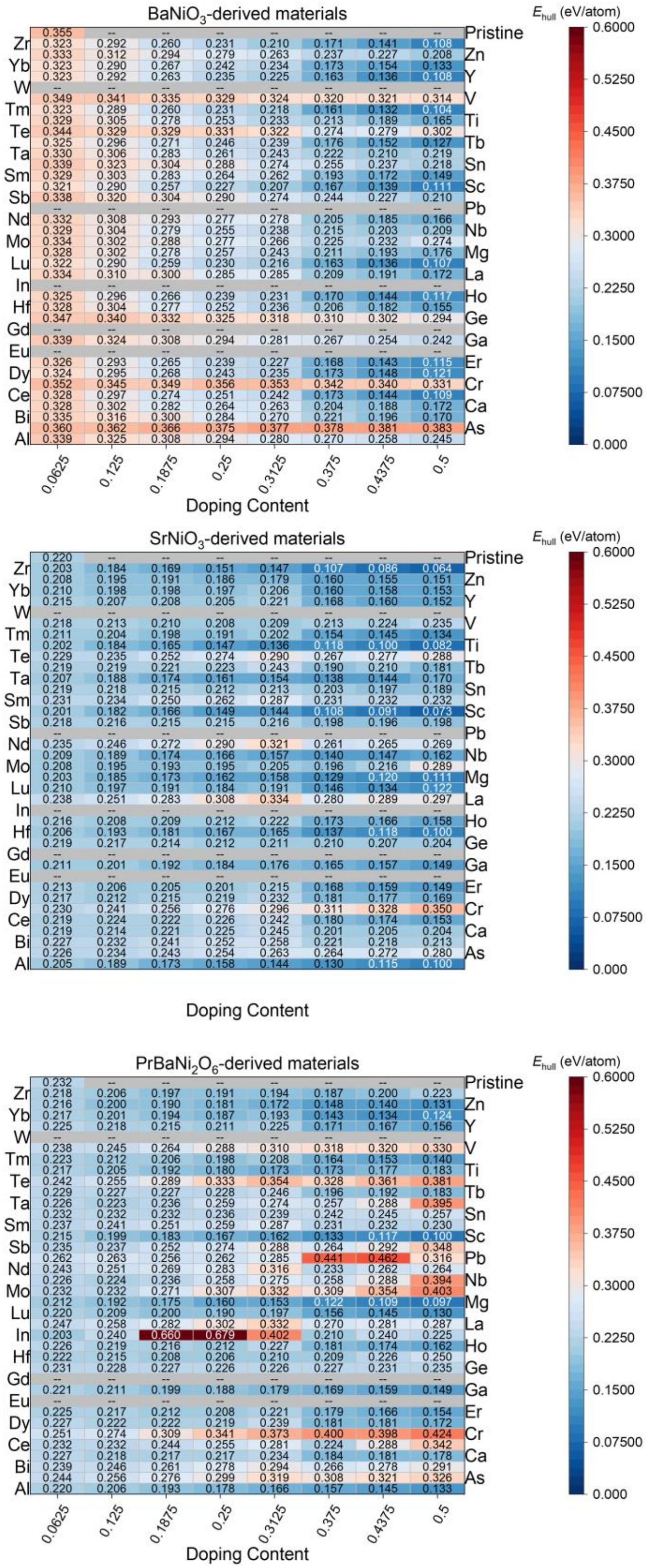

BaNiO$_3$-derived materials

	0.0625	0.125	0.1875	0.25	0.3125	0.375	0.4375	0.5
Pristine	0.355	--	--	--	--	--	--	--
Zr	0.323	0.292	0.260	0.231	0.210	0.171	0.141	0.108
Zn	0.333	0.312	0.294	0.279	0.263	0.237	0.227	0.208
Yb	0.323	0.290	0.267	0.242	0.234	0.173	0.154	0.133
Y	0.323	0.292	0.263	0.235	0.225	0.163	0.136	0.108
W	--	--	--	--	--	--	--	--
V	0.349	0.341	0.335	0.329	0.324	0.320	0.321	0.314
Tm	0.323	0.289	0.260	0.231	0.218	0.161	0.132	0.104
Ti	0.329	0.305	0.278	0.253	0.233	0.213	0.189	0.165
Te	0.344	0.329	0.329	0.331	0.322	0.274	0.279	0.302
Tb	0.325	0.296	0.271	0.246	0.239	0.176	0.152	0.127
Ta	0.330	0.306	0.283	0.261	0.243	0.222	0.210	0.219
Sn	0.339	0.323	0.304	0.288	0.274	0.255	0.237	0.218
Sm	0.329	0.303	0.283	0.264	0.262	0.193	0.172	0.149
Sc	0.321	0.290	0.257	0.227	0.207	0.167	0.139	0.111
Sb	0.338	0.320	0.304	0.290	0.274	0.244	0.227	0.210
Pb	--	--	--	--	--	--	--	--
Nd	0.332	0.308	0.293	0.277	0.278	0.205	0.185	0.166
Nb	0.329	0.304	0.279	0.255	0.238	0.215	0.203	0.209
Mo	0.334	0.302	0.288	0.277	0.266	0.225	0.232	0.274
Mg	0.328	0.302	0.278	0.257	0.243	0.211	0.193	0.176
Lu	0.322	0.290	0.259	0.230	0.216	0.163	0.136	0.107
La	0.334	0.310	0.300	0.285	0.285	0.209	0.191	0.172
In	--	--	--	--	--	--	--	--
Ho	0.325	0.296	0.266	0.239	0.231	0.170	0.144	0.117
Hf	0.328	0.304	0.277	0.252	0.236	0.206	0.182	0.155
Ge	0.347	0.340	0.332	0.325	0.318	0.310	0.302	0.294
Gd	--	--	--	--	--	--	--	--
Ga	0.339	0.324	0.308	0.294	0.281	0.267	0.254	0.242
Eu	--	--	--	--	--	--	--	--
Er	0.326	0.293	0.265	0.239	0.227	0.168	0.143	0.115
Dy	0.324	0.295	0.268	0.243	0.235	0.173	0.148	0.121
Cr	0.352	0.345	0.349	0.356	0.353	0.342	0.340	0.331
Ce	0.328	0.297	0.274	0.251	0.242	0.173	0.144	0.109
Ca	0.328	0.302	0.282	0.264	0.263	0.204	0.188	0.172
Bi	0.335	0.316	0.300	0.284	0.270	0.221	0.196	0.170
As	0.360	0.362	0.366	0.375	0.377	0.378	0.381	0.383
Al	0.339	0.325	0.308	0.294	0.280	0.270	0.258	0.245

SrNiO$_3$-derived materials

Pristine	0.220	--	--	--	--	--	--	--
Zr	0.203	0.184	0.169	0.151	0.147	0.107	0.086	0.064
Zn	0.208	0.195	0.191	0.186	0.179	0.160	0.155	0.151
Yb	0.210	0.198	0.198	0.197	0.206	0.160	0.158	0.153
Y	0.215	0.207	0.208	0.205	0.221	0.168	0.160	0.152
W	--	--	--	--	--	--	--	--
V	0.218	0.213	0.210	0.208	0.209	0.213	0.224	0.235
Tm	0.211	0.204	0.198	0.191	0.202	0.154	0.145	0.134
Ti	0.202	0.184	0.165	0.147	0.136	0.118	0.100	0.082
Te	0.229	0.235	0.252	0.274	0.290	0.267	0.277	0.288
Tb	0.219	0.219	0.221	0.223	0.243	0.190	0.210	0.181
Ta	0.207	0.188	0.174	0.161	0.154	0.138	0.144	0.170
Sn	0.219	0.218	0.215	0.212	0.213	0.203	0.197	0.189
Sm	0.231	0.234	0.250	0.262	0.287	0.231	0.232	0.232
Sc	0.201	0.182	0.166	0.149	0.144	0.108	0.091	0.073
Sb	0.218	0.216	0.215	0.215	0.216	0.198	0.196	0.198
Pb	--	--	--	--	--	--	--	--
Nd	0.235	0.246	0.272	0.290	0.321	0.261	0.265	0.269
Nb	0.209	0.189	0.174	0.166	0.157	0.140	0.147	0.162
Mo	0.208	0.195	0.193	0.195	0.205	0.196	0.216	0.289
Mg	0.203	0.185	0.173	0.162	0.158	0.129	0.120	0.111
Lu	0.210	0.197	0.191	0.184	0.191	0.146	0.134	0.122
La	0.238	0.251	0.283	0.308	0.334	0.280	0.289	0.297
In	--	--	--	--	--	--	--	--
Ho	0.216	0.208	0.209	0.212	0.222	0.173	0.166	0.158
Hf	0.206	0.193	0.181	0.167	0.165	0.137	0.118	0.100
Ge	0.219	0.217	0.214	0.212	0.211	0.210	0.207	0.204
Gd	--	--	--	--	--	--	--	--
Ga	0.211	0.201	0.192	0.184	0.176	0.165	0.157	0.149
Eu	--	--	--	--	--	--	--	--
Er	0.213	0.206	0.205	0.201	0.215	0.168	0.159	0.149
Dy	0.217	0.212	0.215	0.219	0.232	0.181	0.177	0.169
Cr	0.230	0.241	0.256	0.276	0.296	0.311	0.328	0.350
Ce	0.219	0.224	0.222	0.226	0.242	0.180	0.174	0.153
Ca	0.219	0.214	0.221	0.225	0.245	0.201	0.205	0.204
Bi	0.227	0.232	0.241	0.252	0.258	0.221	0.218	0.213
As	0.226	0.234	0.243	0.254	0.263	0.264	0.272	0.280
Al	0.205	0.189	0.173	0.158	0.144	0.130	0.115	0.100

PrBaNi$_2$O$_6$-derived materials

	0.0625	0.125	0.1875	0.25	0.3125	0.375	0.4375	0.5
Pristine	0.232	--	--	--	--	--	--	--
Zr	0.218	0.206	0.197	0.191	0.194	0.187	0.200	0.223
Zn	0.216	0.200	0.190	0.181	0.172	0.148	0.140	0.131
Yb	0.217	0.201	0.194	0.187	0.193	0.143	0.134	0.124
Y	0.225	0.218	0.215	0.211	0.225	0.171	0.167	0.156
W	--	--	--	--	--	--	--	--
V	0.238	0.245	0.264	0.288	0.310	0.318	0.320	0.330
Tm	0.223	0.212	0.206	0.198	0.208	0.164	0.153	0.140
Ti	0.217	0.205	0.192	0.180	0.173	0.173	0.177	0.183
Te	0.242	0.255	0.289	0.333	0.354	0.328	0.361	0.381
Tb	0.229	0.227	0.227	0.228	0.246	0.196	0.192	0.183
Ta	0.226	0.223	0.236	0.259	0.274	0.257	0.288	0.395
Sn	0.232	0.232	0.232	0.236	0.239	0.242	0.245	0.257
Sm	0.237	0.241	0.251	0.259	0.287	0.231	0.232	0.230
Sc	0.215	0.199	0.183	0.167	0.162	0.133	0.117	0.100
Sb	0.235	0.237	0.252	0.274	0.288	0.264	0.292	0.348
Pb	0.262	0.263	0.256	0.262	0.285	0.441	0.462	0.316
Nd	0.243	0.251	0.269	0.283	0.316	0.233	0.262	0.264
Nb	0.226	0.224	0.236	0.258	0.275	0.258	0.288	0.394
Mo	0.232	0.232	0.271	0.307	0.332	0.309	0.354	0.403
Mg	0.212	0.192	0.175	0.160	0.153	0.122	0.109	0.097
Lu	0.220	0.209	0.200	0.190	0.197	0.156	0.145	0.130
La	0.247	0.258	0.282	0.302	0.332	0.270	0.281	0.287
In	0.203	0.240	0.660	0.679	0.402	0.210	0.240	0.225
Ho	0.226	0.219	0.216	0.212	0.227	0.181	0.174	0.162
Hf	0.222	0.215	0.208	0.206	0.210	0.209	0.226	0.250
Ge	0.231	0.228	0.227	0.226	0.226	0.227	0.231	0.235
Gd	--	--	--	--	--	--	--	--
Ga	0.221	0.211	0.199	0.188	0.179	0.169	0.159	0.149
Eu	--	--	--	--	--	--	--	--
Er	0.225	0.217	0.212	0.208	0.221	0.179	0.166	0.154
Dy	0.227	0.222	0.222	0.219	0.239	0.181	0.181	0.172
Cr	0.251	0.274	0.309	0.341	0.373	0.400	0.398	0.424
Ce	0.232	0.232	0.244	0.255	0.281	0.224	0.288	0.342
Ca	0.227	0.218	0.217	0.217	0.234	0.184	0.181	0.178
Bi	0.239	0.246	0.261	0.278	0.294	0.266	0.278	0.291
As	0.244	0.256	0.276	0.299	0.319	0.308	0.321	0.326
Al	0.220	0.206	0.193	0.178	0.166	0.157	0.145	0.133

Figure S4. Summary of E_{hull} values for BaNiO$_3$, SrNiO$_3$, and PrBaNi$_2$O$_6$-derived materials.

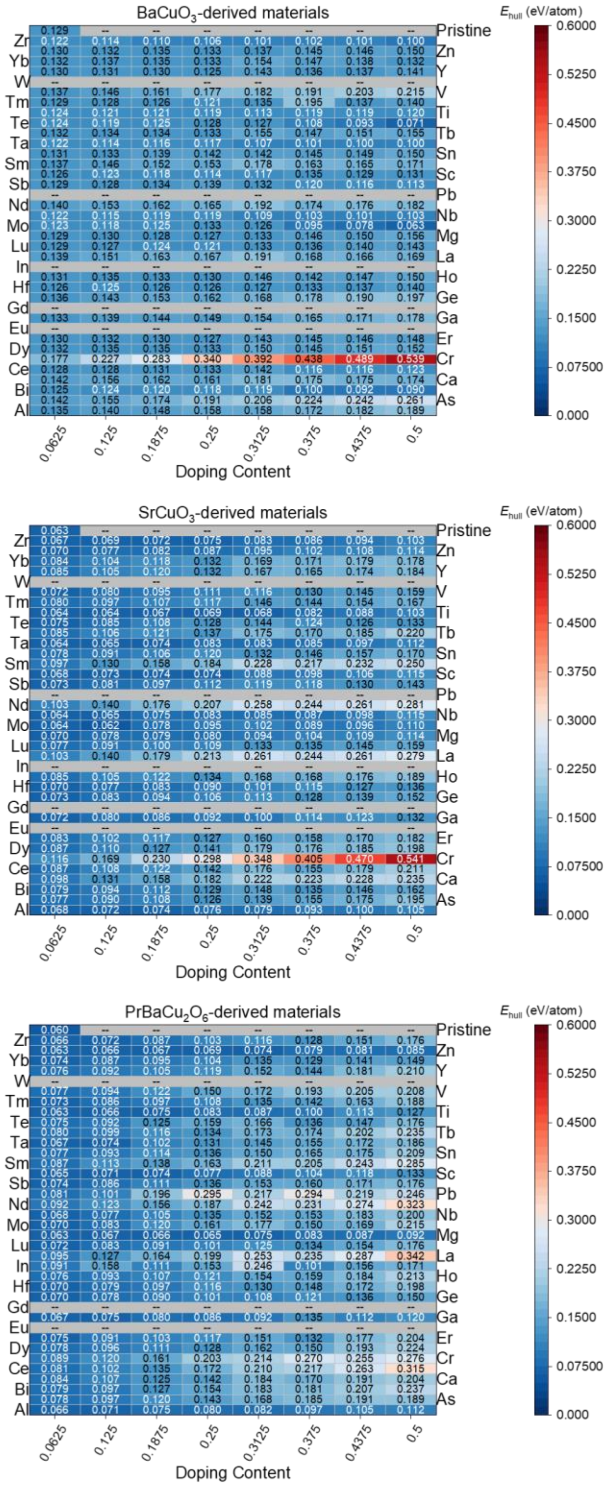

$BaCuO_3$-derived materials

	0.0625	0.125	0.1875	0.25	0.3125	0.375	0.4375	0.5
Pristine	0.129	--	--	--	--	--	--	--
Zr	0.122	0.114	0.110	0.106	0.101	0.102	0.101	0.100
Zn	0.130	0.132	0.135	0.133	0.137	0.145	0.146	0.150
Yb	0.132	0.137	0.135	0.133	0.154	0.147	0.138	0.132
Y	0.130	0.131	0.130	0.125	0.143	0.136	0.137	0.141
W	--	--	--	--	--	--	--	--
V	0.137	0.146	0.161	0.177	0.182	0.191	0.203	0.215
Tm	0.129	0.128	0.126	0.121	0.135	0.195	0.137	0.140
Ti	0.124	0.121	0.121	0.119	0.113	0.119	0.119	0.120
Te	0.124	0.119	0.125	0.128	0.127	0.108	0.093	0.071
Tb	0.132	0.134	0.134	0.133	0.155	0.147	0.151	0.155
Ta	0.122	0.114	0.116	0.117	0.107	0.101	0.100	0.100
Sn	0.131	0.133	0.139	0.142	0.142	0.145	0.149	0.150
Sm	0.137	0.146	0.152	0.153	0.178	0.163	0.165	0.171
Sc	0.126	0.123	0.118	0.114	0.117	0.135	0.129	0.131
Sb	0.129	0.128	0.134	0.139	0.132	0.120	0.116	0.113
Pb	--	--	--	--	--	--	--	--
Nd	0.140	0.153	0.162	0.165	0.192	0.174	0.176	0.182
Nb	0.122	0.115	0.119	0.119	0.109	0.103	0.101	0.103
Mo	0.123	0.118	0.125	0.133	0.126	0.095	0.078	0.063
Mg	0.129	0.130	0.128	0.127	0.133	0.146	0.150	0.156
Lu	0.129	0.127	0.124	0.121	0.133	0.136	0.140	0.143
La	0.139	0.151	0.163	0.167	0.191	0.168	0.166	0.169
In	--	--	--	--	--	--	--	--
Ho	0.131	0.135	0.133	0.130	0.146	0.142	0.147	0.150
Hf	0.126	0.125	0.126	0.126	0.127	0.133	0.137	0.140
Ge	0.136	0.143	0.153	0.162	0.168	0.178	0.190	0.197
Gd	--	--	--	--	--	--	--	--
Ga	0.133	0.139	0.144	0.149	0.154	0.165	0.171	0.178
Eu	--	--	--	--	--	--	--	--
Er	0.130	0.132	0.130	0.127	0.143	0.145	0.146	0.148
Dy	0.132	0.135	0.135	0.133	0.150	0.145	0.151	0.152
Cr	0.177	0.227	0.283	0.340	0.392	0.438	0.489	0.539
Ce	0.128	0.128	0.131	0.133	0.142	0.116	0.116	0.123
Ca	0.142	0.156	0.162	0.161	0.181	0.175	0.175	0.174
Bi	0.125	0.124	0.120	0.118	0.119	0.100	0.092	0.090
As	0.142	0.155	0.174	0.191	0.206	0.224	0.242	0.261
Al	0.135	0.140	0.148	0.158	0.158	0.172	0.182	0.189

$SrCuO_3$-derived materials

	0.0625	0.125	0.1875	0.25	0.3125	0.375	0.4375	0.5
Pristine	0.063	--	--	--	--	--	--	--
Zr	0.067	0.069	0.072	0.075	0.083	0.086	0.094	0.103
Zn	0.070	0.077	0.082	0.087	0.095	0.102	0.108	0.114
Yb	0.084	0.104	0.118	0.132	0.169	0.171	0.179	0.178
Y	0.085	0.105	0.120	0.132	0.167	0.165	0.174	0.184
W	--	--	--	--	--	--	--	--
V	0.072	0.080	0.095	0.111	0.116	0.130	0.145	0.159
Tm	0.080	0.097	0.107	0.117	0.146	0.144	0.154	0.167
Ti	0.064	0.064	0.067	0.069	0.068	0.082	0.088	0.103
Te	0.075	0.085	0.108	0.128	0.144	0.124	0.126	0.133
Tb	0.085	0.106	0.121	0.137	0.175	0.170	0.185	0.220
Ta	0.064	0.065	0.074	0.083	0.083	0.085	0.097	0.112
Sn	0.078	0.091	0.106	0.120	0.132	0.146	0.157	0.170
Sm	0.097	0.130	0.158	0.184	0.228	0.217	0.232	0.250
Sc	0.068	0.073	0.074	0.074	0.088	0.098	0.106	0.115
Sb	0.073	0.081	0.097	0.112	0.119	0.118	0.130	0.143
Pb	--	--	--	--	--	--	--	--
Nd	0.103	0.140	0.176	0.207	0.258	0.244	0.261	0.281
Nb	0.064	0.065	0.075	0.083	0.085	0.087	0.098	0.115
Mo	0.064	0.062	0.078	0.095	0.102	0.089	0.096	0.110
Mg	0.070	0.078	0.079	0.080	0.094	0.104	0.109	0.114
Lu	0.077	0.091	0.100	0.109	0.133	0.135	0.145	0.159
La	0.103	0.140	0.179	0.213	0.261	0.244	0.261	0.279
In	--	--	--	--	--	--	--	--
Ho	0.085	0.105	0.122	0.134	0.168	0.168	0.176	0.189
Hf	0.070	0.077	0.083	0.090	0.101	0.115	0.127	0.136
Ge	0.073	0.083	0.094	0.106	0.113	0.128	0.139	0.152
Gd	--	--	--	--	--	--	--	--
Ga	0.072	0.080	0.086	0.092	0.100	0.114	0.123	0.132
Eu	--	--	--	--	--	--	--	--
Er	0.083	0.102	0.117	0.127	0.160	0.158	0.170	0.182
Dy	0.087	0.110	0.127	0.141	0.179	0.176	0.185	0.198
Cr	0.116	0.169	0.230	0.298	0.348	0.405	0.470	0.541
Ce	0.087	0.108	0.122	0.142	0.176	0.155	0.179	0.211
Ca	0.098	0.131	0.158	0.182	0.222	0.223	0.228	0.235
Bi	0.079	0.094	0.112	0.129	0.148	0.135	0.146	0.162
As	0.077	0.090	0.108	0.126	0.139	0.155	0.175	0.195
Al	0.068	0.072	0.074	0.076	0.079	0.093	0.100	0.105

$PrBaCu_2O_6$-derived materials

	0.0625	0.125	0.1875	0.25	0.3125	0.375	0.4375	0.5
Pristine	0.060	--	--	--	--	--	--	--
Zr	0.066	0.072	0.087	0.103	0.116	0.128	0.151	0.176
Zn	0.063	0.066	0.067	0.069	0.074	0.079	0.081	0.085
Yb	0.074	0.087	0.095	0.104	0.135	0.129	0.141	0.149
Y	0.076	0.092	0.105	0.119	0.152	0.144	0.181	0.210
W	--	--	--	--	--	--	--	--
V	0.077	0.094	0.122	0.150	0.172	0.193	0.205	0.208
Tm	0.073	0.086	0.097	0.108	0.135	0.142	0.163	0.188
Ti	0.063	0.066	0.075	0.083	0.087	0.100	0.113	0.127
Te	0.075	0.092	0.125	0.159	0.166	0.136	0.147	0.176
Tb	0.080	0.099	0.116	0.134	0.173	0.174	0.202	0.235
Ta	0.067	0.074	0.102	0.131	0.145	0.155	0.172	0.186
Sn	0.077	0.093	0.114	0.136	0.150	0.165	0.175	0.209
Sm	0.087	0.113	0.138	0.163	0.211	0.205	0.243	0.285
Sc	0.065	0.071	0.074	0.077	0.088	0.104	0.118	0.133
Sb	0.074	0.086	0.111	0.136	0.153	0.160	0.171	0.176
Pb	0.081	0.101	0.196	0.295	0.217	0.294	0.219	0.246
Nd	0.092	0.123	0.156	0.187	0.242	0.231	0.274	0.323
Nb	0.068	0.077	0.105	0.135	0.152	0.153	0.183	0.200
Mo	0.070	0.083	0.120	0.161	0.177	0.150	0.169	0.215
Mg	0.063	0.067	0.066	0.065	0.075	0.083	0.087	0.092
Lu	0.072	0.083	0.091	0.101	0.125	0.134	0.154	0.176
La	0.095	0.127	0.164	0.199	0.253	0.235	0.287	0.342
In	0.091	0.158	0.111	0.153	0.246	0.101	0.156	0.171
Ho	0.076	0.093	0.107	0.121	0.154	0.159	0.184	0.213
Hf	0.070	0.079	0.097	0.116	0.130	0.148	0.172	0.198
Ge	0.070	0.078	0.090	0.101	0.108	0.121	0.136	0.150
Gd	--	--	--	--	--	--	--	--
Ga	0.067	0.075	0.080	0.086	0.092	0.135	0.112	0.120
Eu	--	--	--	--	--	--	--	--
Er	0.075	0.091	0.103	0.117	0.151	0.132	0.177	0.204
Dy	0.078	0.096	0.111	0.128	0.162	0.150	0.193	0.224
Cr	0.089	0.120	0.161	0.203	0.214	0.270	0.255	0.276
Ce	0.081	0.102	0.135	0.172	0.210	0.217	0.263	0.315
Ca	0.084	0.107	0.125	0.142	0.184	0.170	0.191	0.204
Bi	0.079	0.097	0.127	0.154	0.183	0.181	0.207	0.237
As	0.078	0.097	0.120	0.143	0.168	0.185	0.191	0.189
Al	0.066	0.071	0.075	0.080	0.082	0.097	0.105	0.112

Figure S5. Summary of E_{hull} values for $BaCuO_3$, $SrCuO_3$, and $PrBaCu_2O_6$-derived materials.

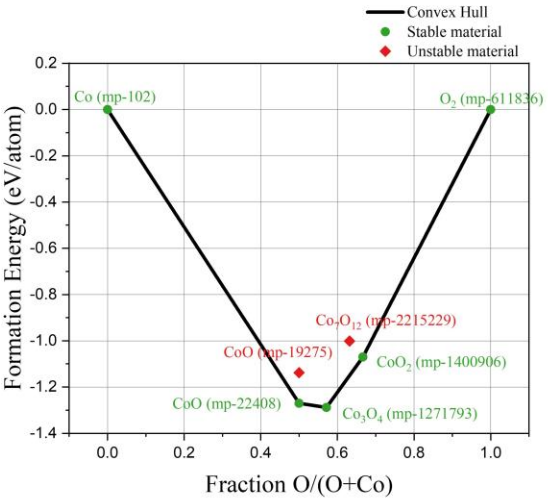

❖ Phase Transformation

CoO (mp-19275, $E_F = 1.138$ eV/atom)
↓
CoO (mp-22408, $E_F = 1.27$ eV/atom)

❖ Structure Decomposition

Co_7O_{12} (mp-2215229, $E_F = 1.001$ eV/atom)
↓
$\begin{cases} Co_3O_4 \text{ (mp-1271793, } E_F = 1.288 \text{ eV/atom)} \\ CoO_2 \text{ (mp-1400906, } E_F = 1.07 \text{ eV/atom)} \end{cases}$

Figure S6. Schematic representation of the decomposition analysis method, using the Co-O binary phase diagram to demonstrate the analytical approach.

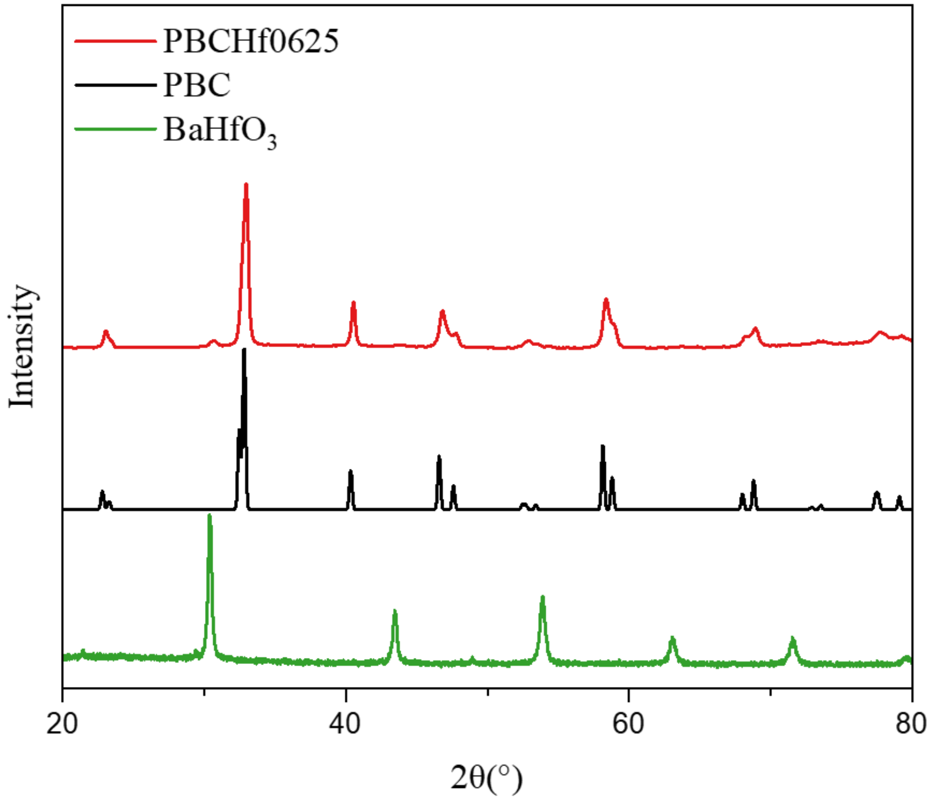

Figure S7. XRD patterns for $PrBaCo_{1.875}Hf_{0.125}O_{5+\delta}$ alongside pristine PBC for reference. The identified secondary phase $BaHfO_3$ is also indicated.

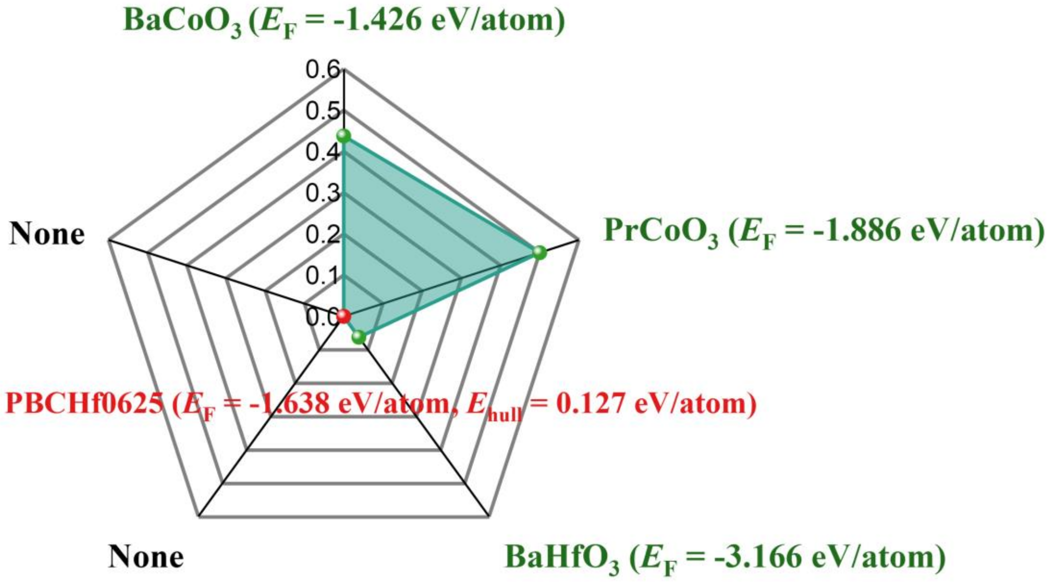

Figure S8. Two-dimensional representations of the decomposition analysis for $PrBaCo_{1.875}Hf_{0.125}O_{5+\delta}$, highlighting the stable phases in green.

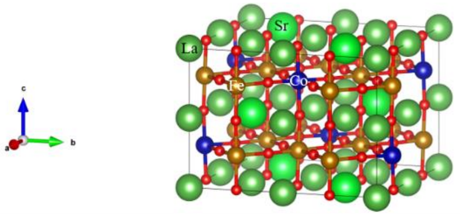

$La_{0.625}Sr_{0.375}Co_{0.1875}Fe_{0.8125}O_3$

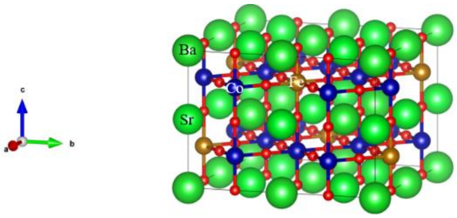

$Ba_{0.5}Sr_{0.5}Co_{0.8125}Fe_{0.1875}O_3$

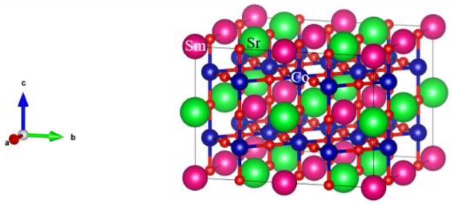

$Sm_{0.5}Sr_{0.5}CoO_3$

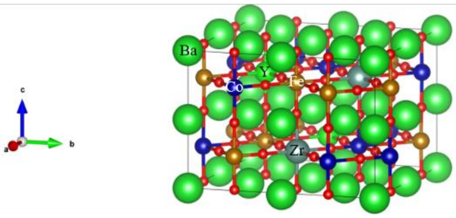

$BaCo_{0.375}Fe_{0.375}Zr_{0.125}Y_{0.125}O_3$

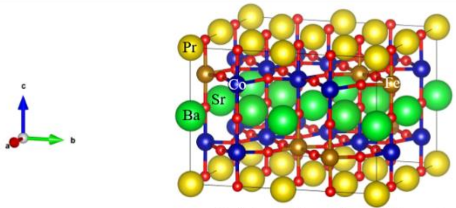

$PrBa_{0.5}Sr_{0.5}Co_{1.5}Fe_{0.5}O_6$

Figure S9. Depiction of the bulk structures for state-of-the-art oxygen electrodes including LSCF, BSCF, SSC, BCFZY, and PBSCF.

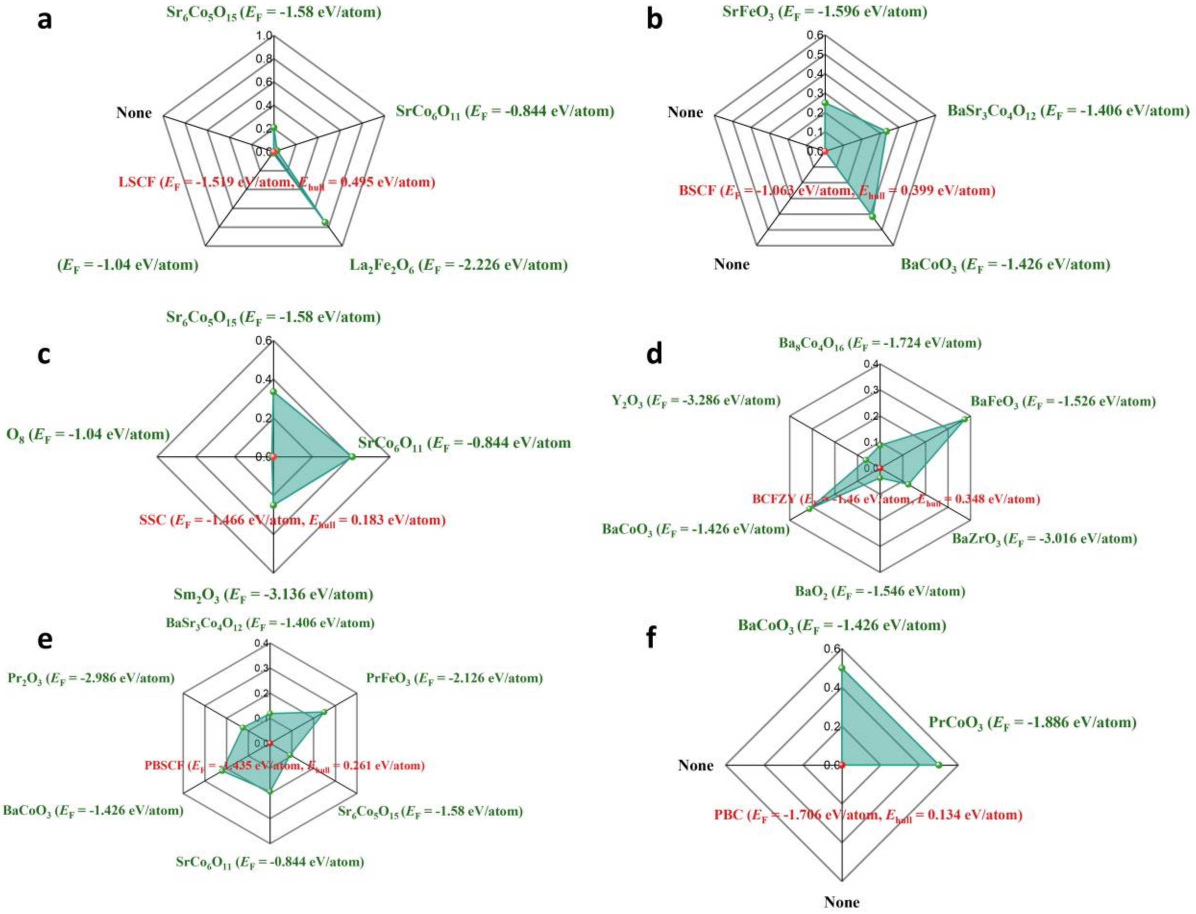

Figure S10. Two-dimensional representations of the decomposition analysis for LSCF (a), BSCF (b), SSC (c), BCFZY (d), PBSCF (e), and PBC (f).

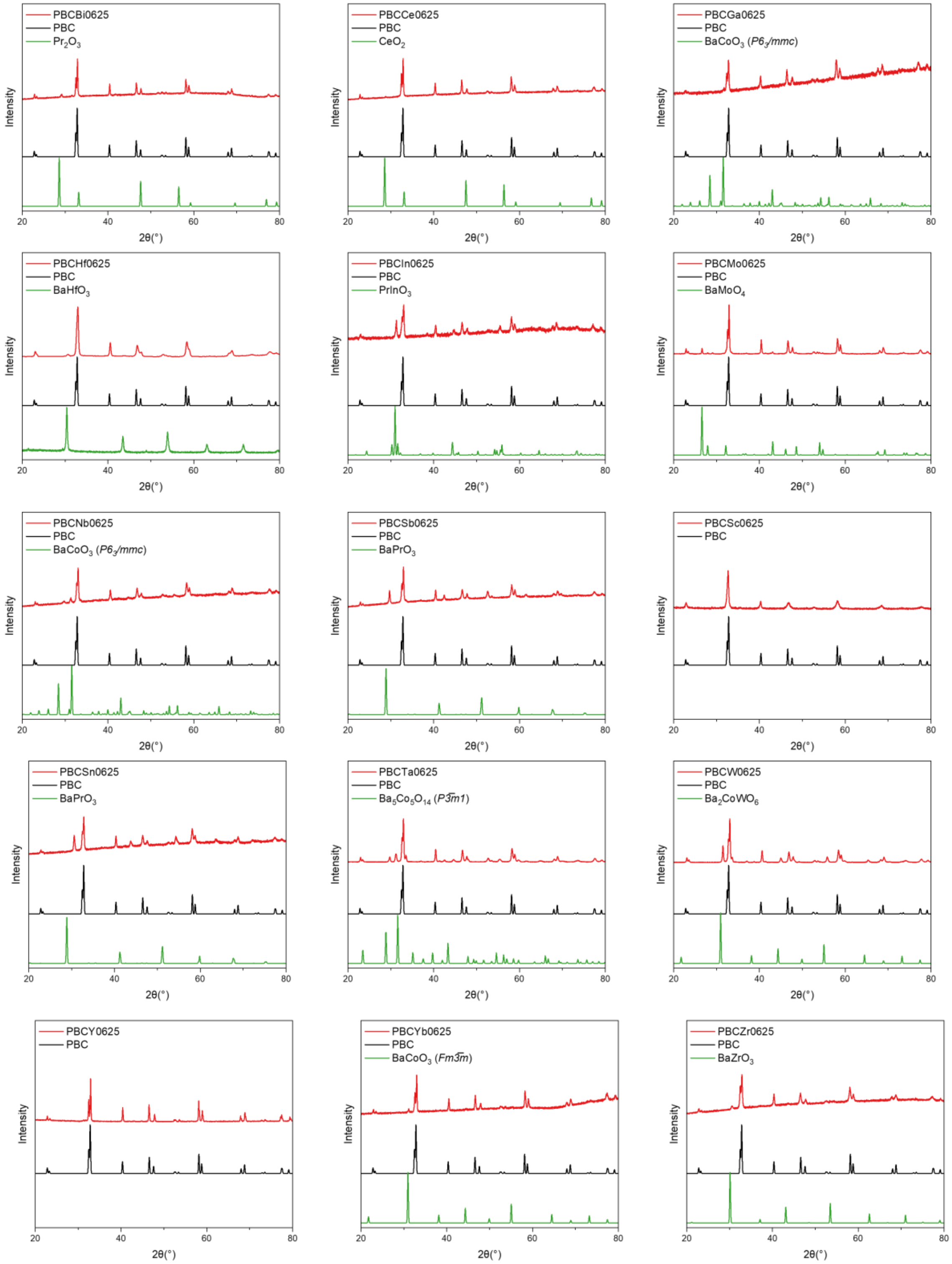
PBCBi0625
PBC
Pr_2O_3
PBCCe0625
PBC
CeO_2
PBCGa0625
PBC
$BaCoO_3$ ($P6_3/mmc$)
PBCHf0625
PBC
$BaHfO_3$
PBCIn0625
PBC
$PrInO_3$
PBCMo0625
PBC
$BaMoO_4$
PBCNb0625
PBC
$BaCoO_3$ ($P6_3/mmc$)
PBCSb0625
PBC
$BaPrO_3$
PBCSc0625
PBC
PBCSn0625
PBC
$BaPrO_3$
PBCTa0625
PBC
$Ba_5Co_5O_{14}$ ($P\bar{3}m1$)
PBCW0625
PBC
Ba_2CoWO_6
PBCY0625
PBC
PBCYb0625
PBC
$BaCoO_3$ ($Fm\bar{3}m$)
PBCZr0625
PBC
$BaZrO_3$
Intensity
2θ(°)
20
40
60
80

Figure S11. XRD patterns for $PrBaCo_{1.875}M_{0.125}O_{5+\delta}$ (M = Bi, Ce, Ga, Hf, In, Mo, Nb, Sb, Sc, Sn, Ta, W, Y, Yb, and Zr) alongside pristine PBC for reference. The identified secondary phase for each specific compound is also indicated.

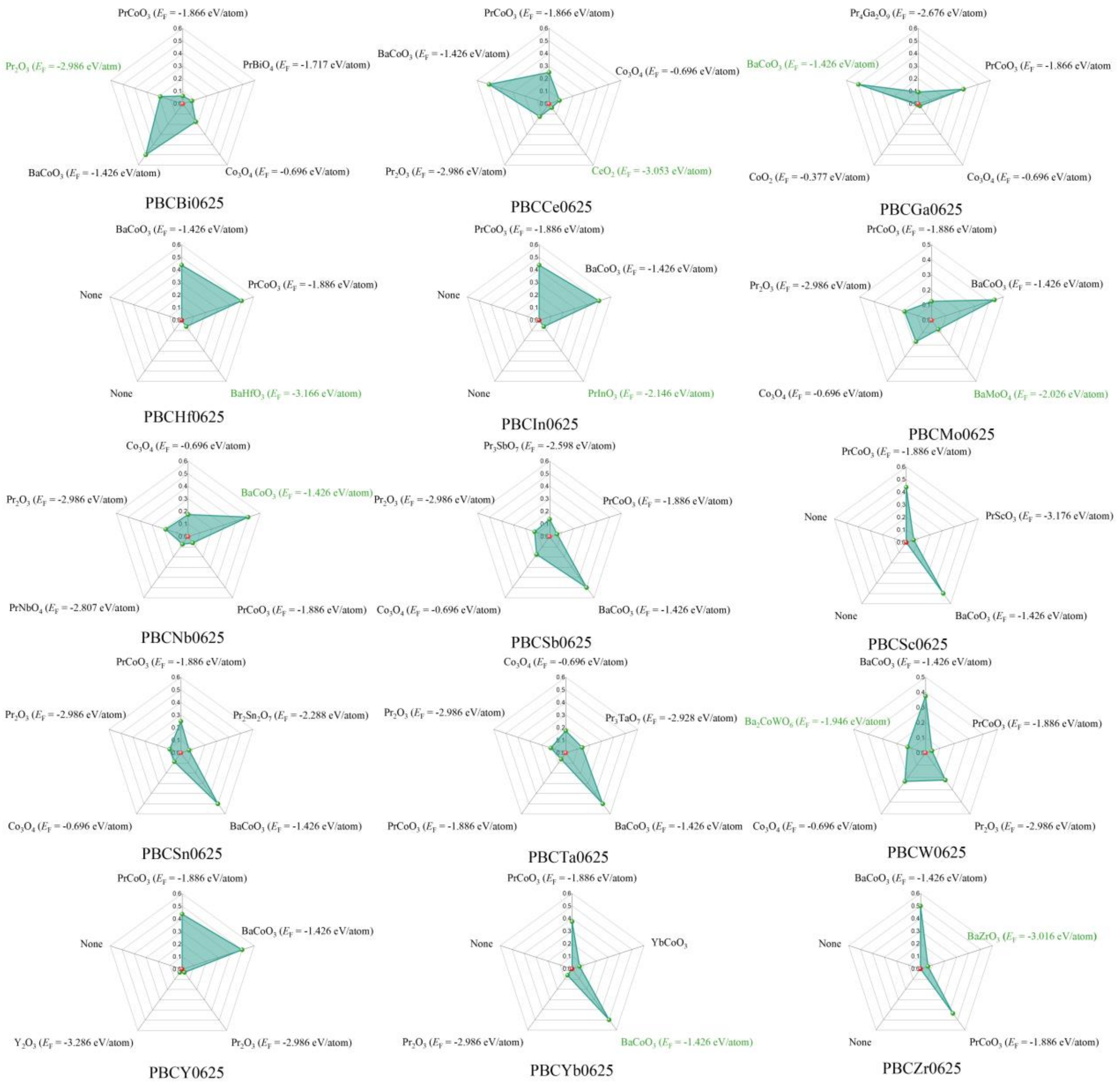

PBCBi0625 PBCCe0625 PBCGa0625

PBCHf0625 PBCIn0625 PBCMo0625

PBCNb0625 PBCSb0625 PBCSc0625

PBCSn0625 PBCTa0625 PBCW0625

PBCY0625 PBCYb0625 PBCZr0625

Figure S12. Two-dimensional representations of the decomposition analysis for $PrBaCo_{1.875}M_{0.125}O_{5+\delta}$ (M = Bi, Ce, Ga, Hf, In, Mo, Nb, Sb, Sc, Sn, Ta, W, Y, Yb, and Zr), highlighting successful prediction in green.

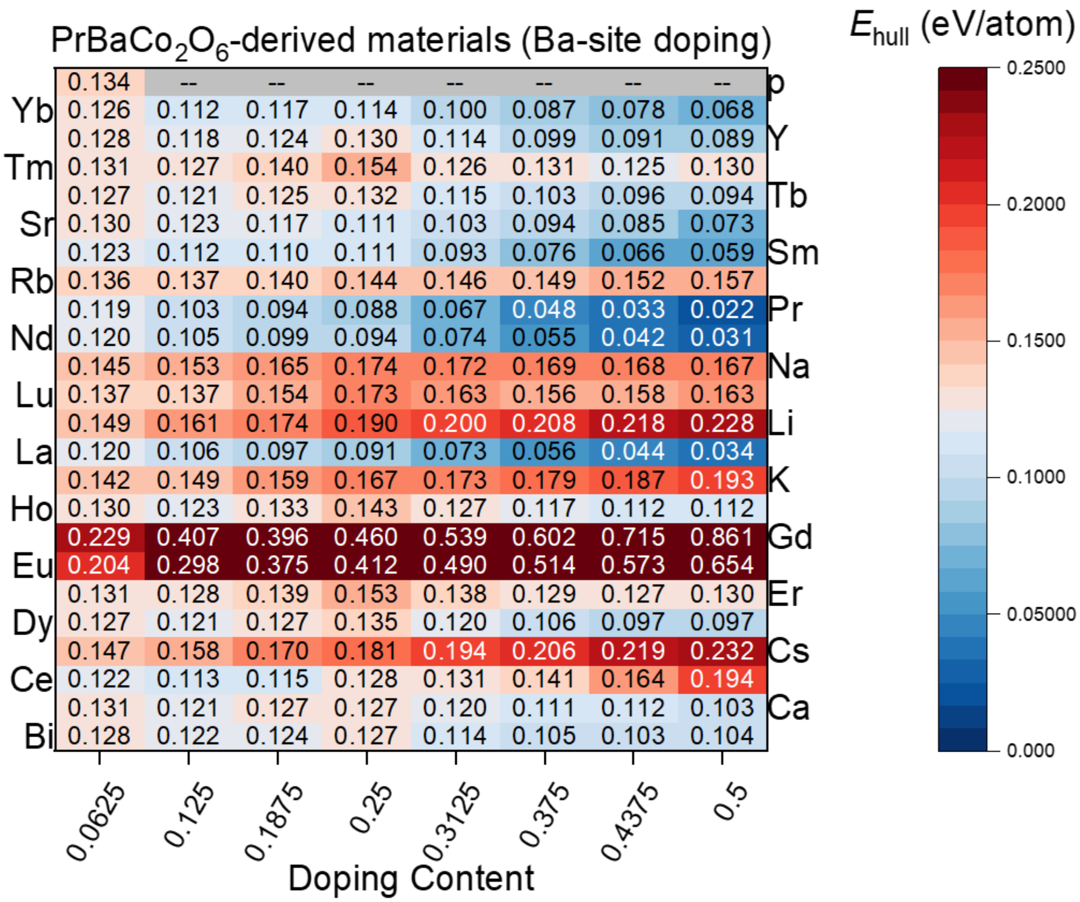

	0.0625	0.125	0.1875	0.25	0.3125	0.375	0.4375	0.5
p	0.134	--	--	--	--	--	--	--
Yb	0.126	0.112	0.117	0.114	0.100	0.087	0.078	0.068
Y	0.128	0.118	0.124	0.130	0.114	0.099	0.091	0.089
Tm	0.131	0.127	0.140	0.154	0.126	0.131	0.125	0.130
Tb	0.127	0.121	0.125	0.132	0.115	0.103	0.096	0.094
Sr	0.130	0.123	0.117	0.111	0.103	0.094	0.085	0.073
Sm	0.123	0.112	0.110	0.111	0.093	0.076	0.066	0.059
Rb	0.136	0.137	0.140	0.144	0.146	0.149	0.152	0.157
Pr	0.119	0.103	0.094	0.088	0.067	0.048	0.033	0.022
Nd	0.120	0.105	0.099	0.094	0.074	0.055	0.042	0.031
Na	0.145	0.153	0.165	0.174	0.172	0.169	0.168	0.167
Lu	0.137	0.137	0.154	0.173	0.163	0.156	0.158	0.163
Li	0.149	0.161	0.174	0.190	0.200	0.208	0.218	0.228
La	0.120	0.106	0.097	0.091	0.073	0.056	0.044	0.034
K	0.142	0.149	0.159	0.167	0.173	0.179	0.187	0.193
Ho	0.130	0.123	0.133	0.143	0.127	0.117	0.112	0.112
Gd	0.229	0.407	0.396	0.460	0.539	0.602	0.715	0.861
Eu	0.204	0.298	0.375	0.412	0.490	0.514	0.573	0.654
Er	0.131	0.128	0.139	0.153	0.138	0.129	0.127	0.130
Dy	0.127	0.121	0.127	0.135	0.120	0.106	0.097	0.097
Cs	0.147	0.158	0.170	0.181	0.194	0.206	0.219	0.232
Ce	0.122	0.113	0.115	0.128	0.131	0.141	0.164	0.194
Ca	0.131	0.121	0.127	0.127	0.120	0.111	0.112	0.103
Bi	0.128	0.122	0.124	0.127	0.114	0.105	0.103	0.104

Figure S13. Summary of E_{hull} values for PrBaCo$_2$O$_6$-derived materials, showcasing the effects of substituting various elements in Ba site.

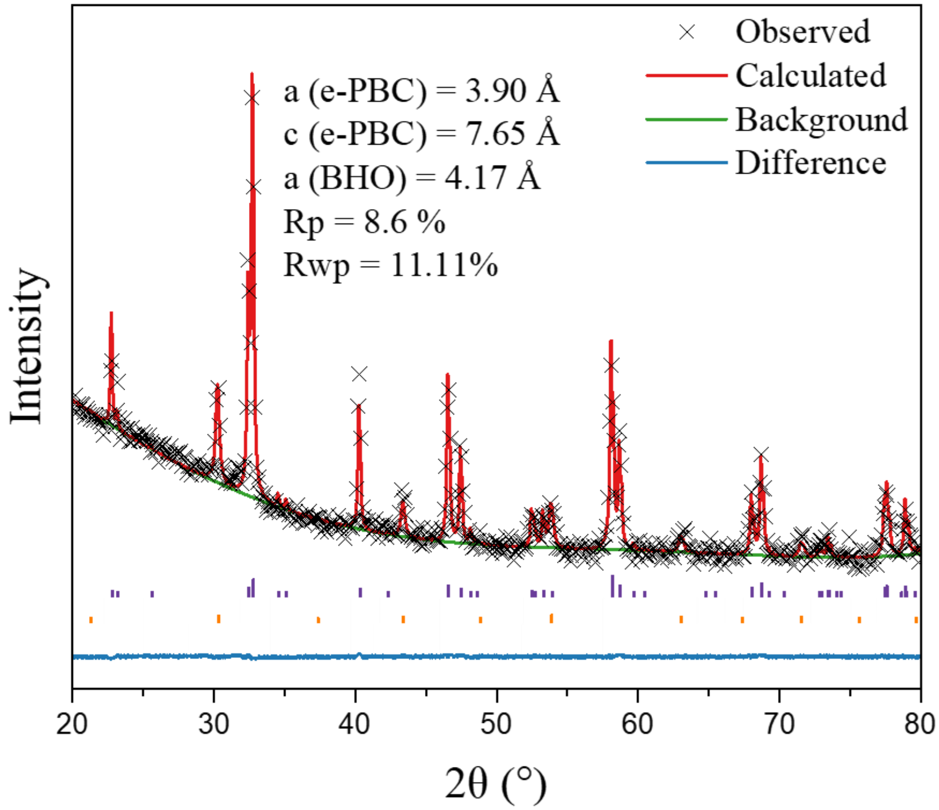

Figure S14. Rietveld refinement results from XRD patterns for PBCHf10.

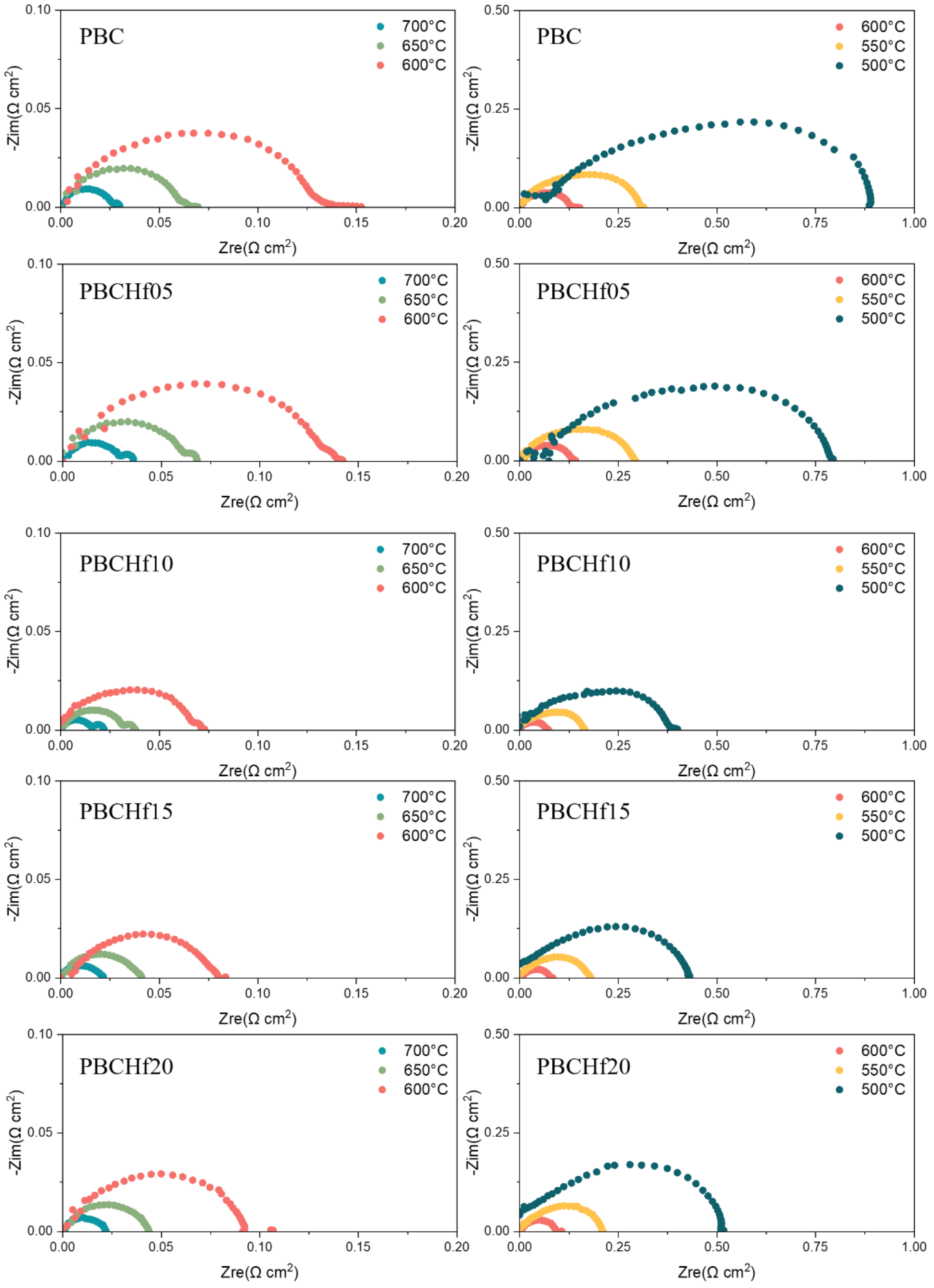

Figure S15. Summary of EIS results for the symmetrical cells using SDC as the electrolyte and Hf-doped PBC materials as the oxygen electrode in air at temperatures from 500 to 700 °C.

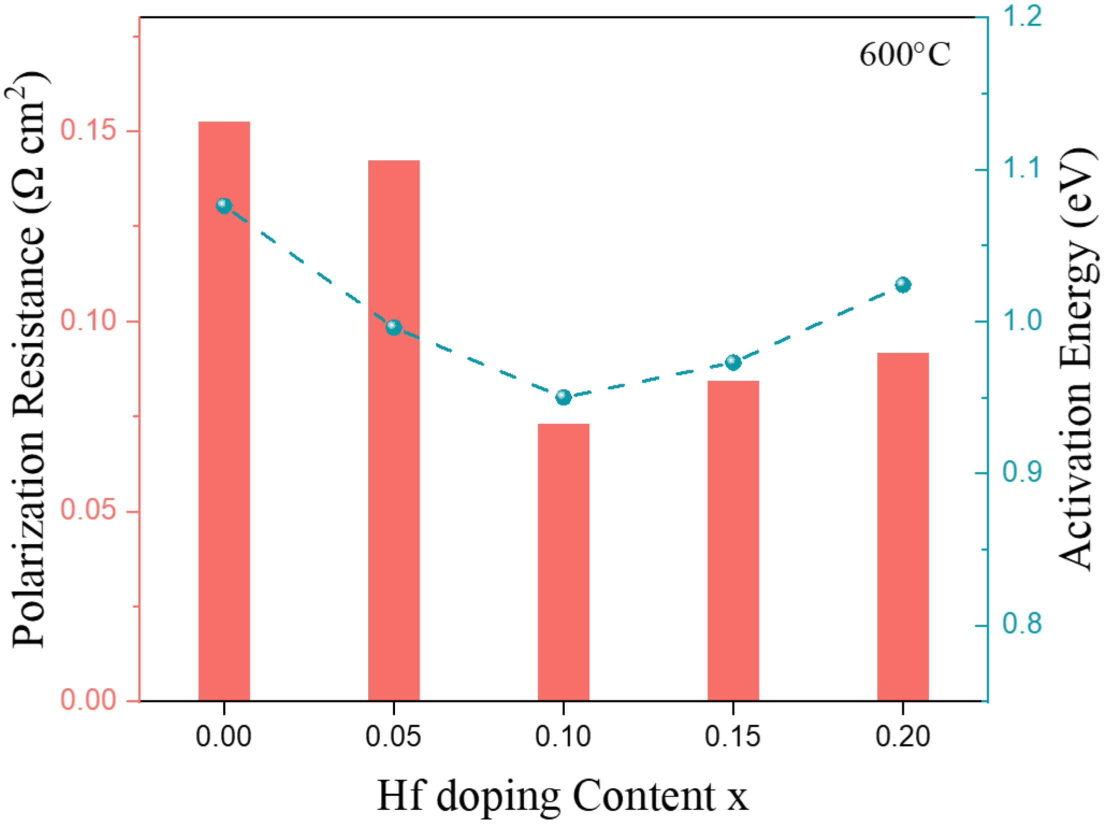

Figure S16. Evaluation of R_p at 600 °C and activation energy for Hf-doped PBC series materials.

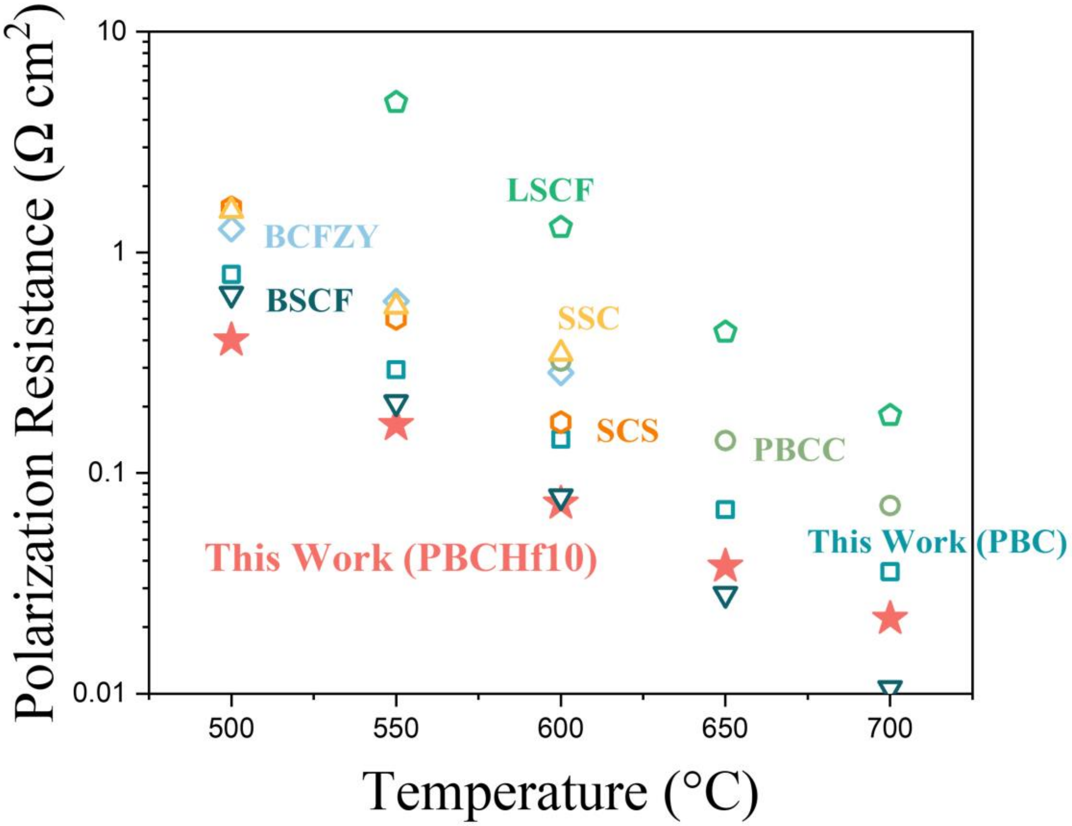

Figure S17. Comparative analysis of R_p for SDC-based symmetrical cells with a configuration of PBCHf10/SDC/PBCHf10 at 700-500 °C[28-33].

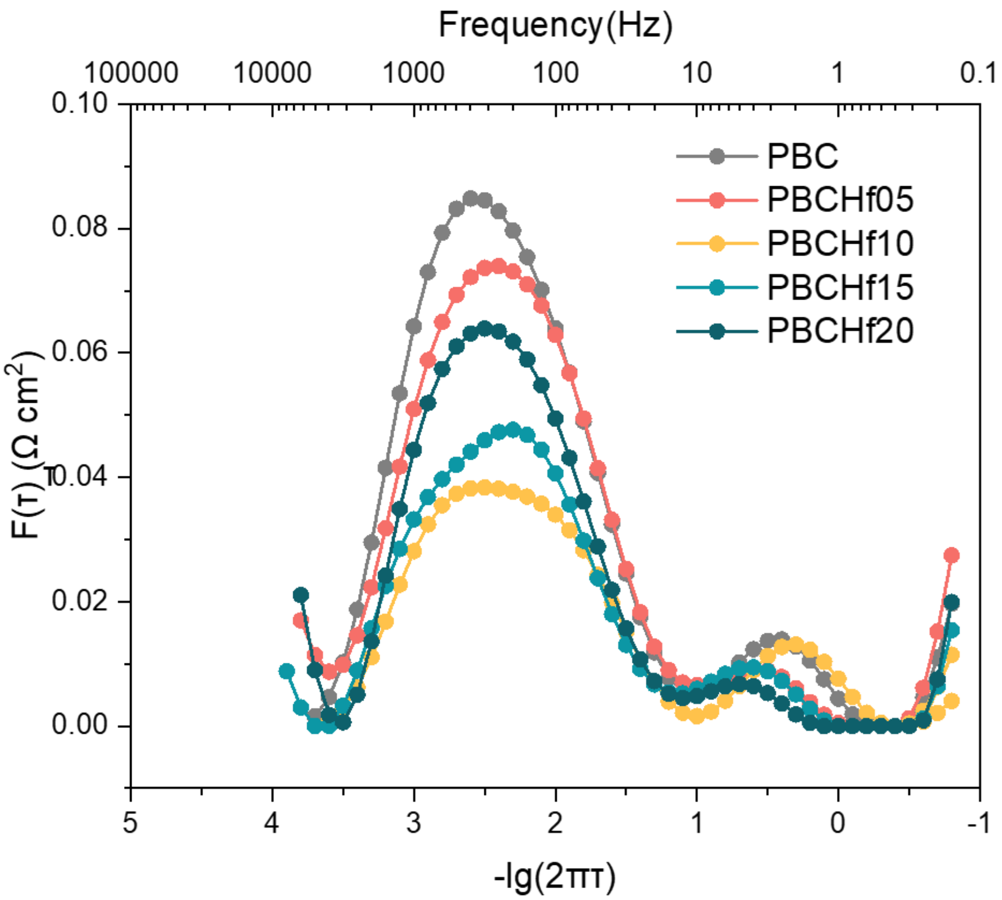

Figure S18. DRT analysis of the EIS results of symmetrical cells in air at 600 °C, as presented in Supplementary Fig. S15.

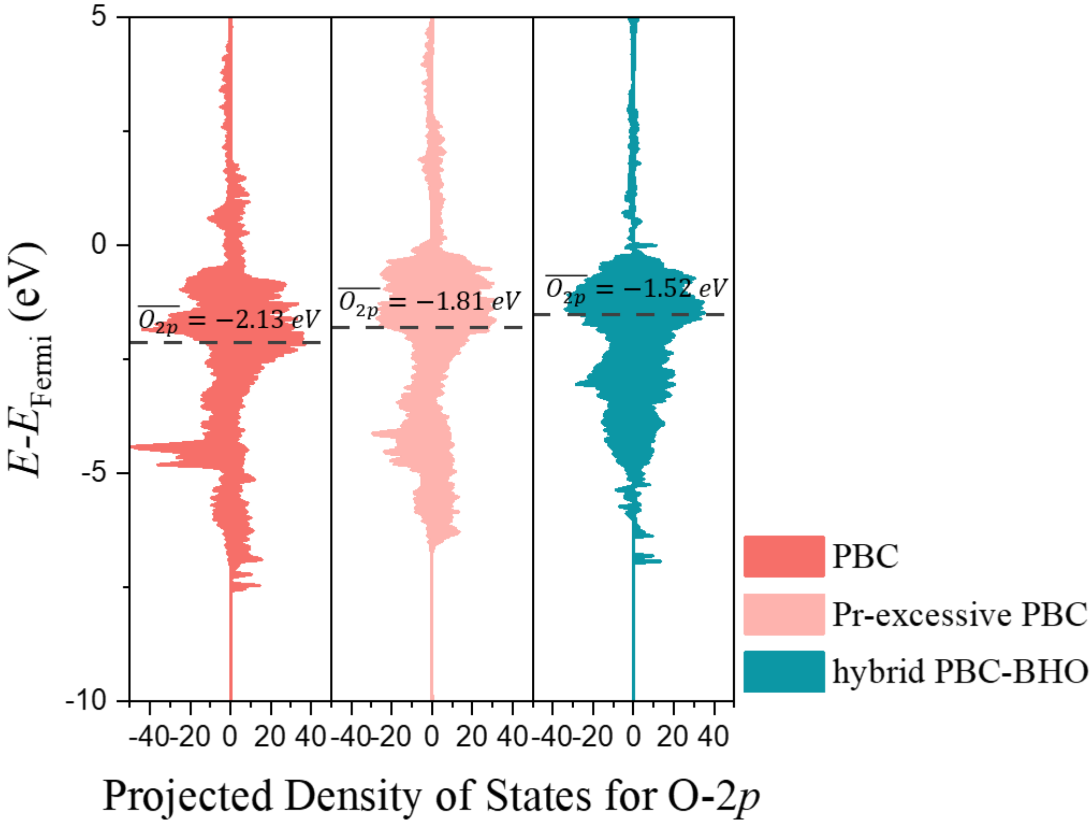

Figure S19. Projected density of states for O-2*p* in PBC, Pr-excessive PBC, and the hybrid PBC-BHO configurations, with the oxygen *p*-band center values labeled.

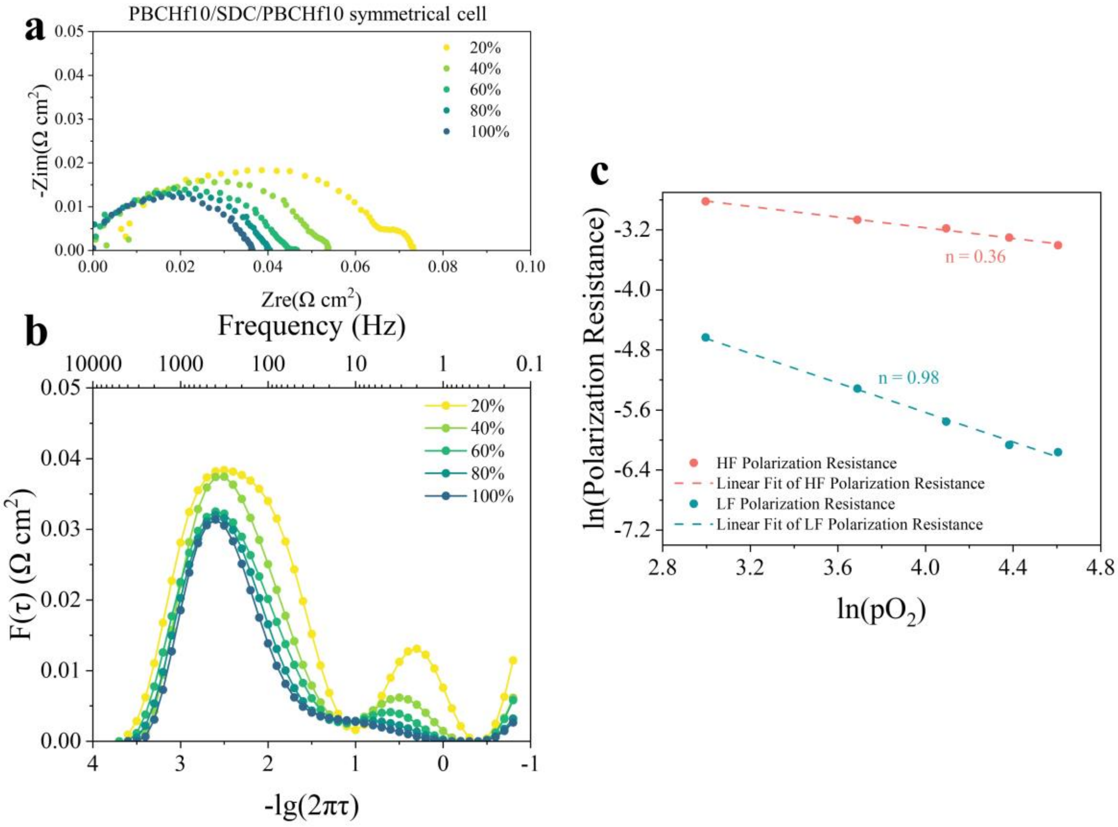

Figure S20. ORR rate-determining steps identification (a) EIS results for PBCHf10/SDC/PBCHf10 symmetrical cells at 600°C under various oxygen partial pressure. (b) DRT analysis of the EIS results presented in (a). (c) The results of linear fitting for the logarithm of both high-frequency and low-frequency R_p, plotted as functions of the logarithm of oxygen partial pressure.

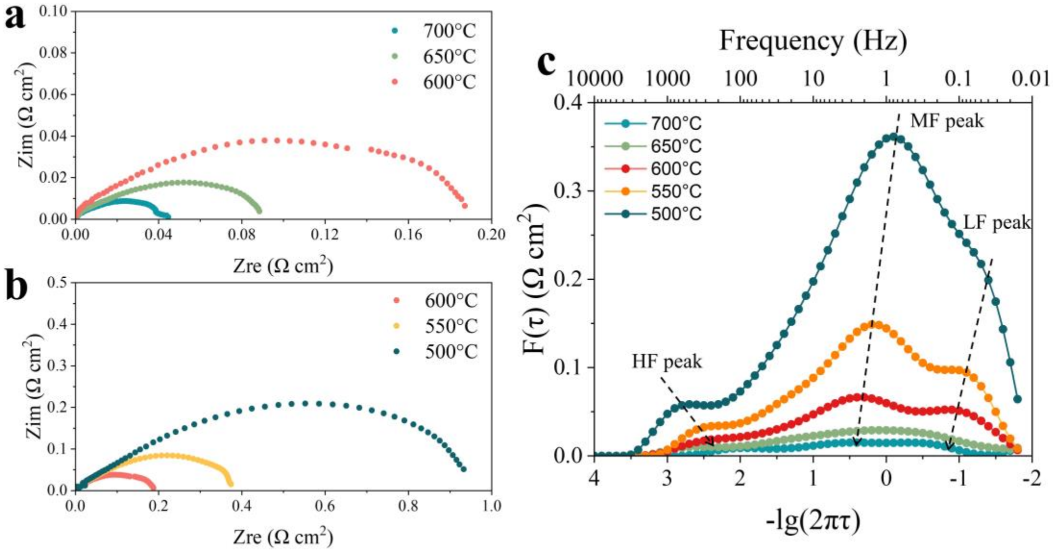

Figure S21. (a) and (b) EIS results for PBCHf10/BZCYYb1711/PBCHf10 symmetrical cells in air at temperatures from 500 to 700 °C. (c) DRT analysis of the EIS results presented in (a) and (b).

DRT analysis was conducted to probe the material's behavior across various temperatures. Three distinct peaks had been observed, with which corresponding to individual elementary steps in the PI-ORR processes.

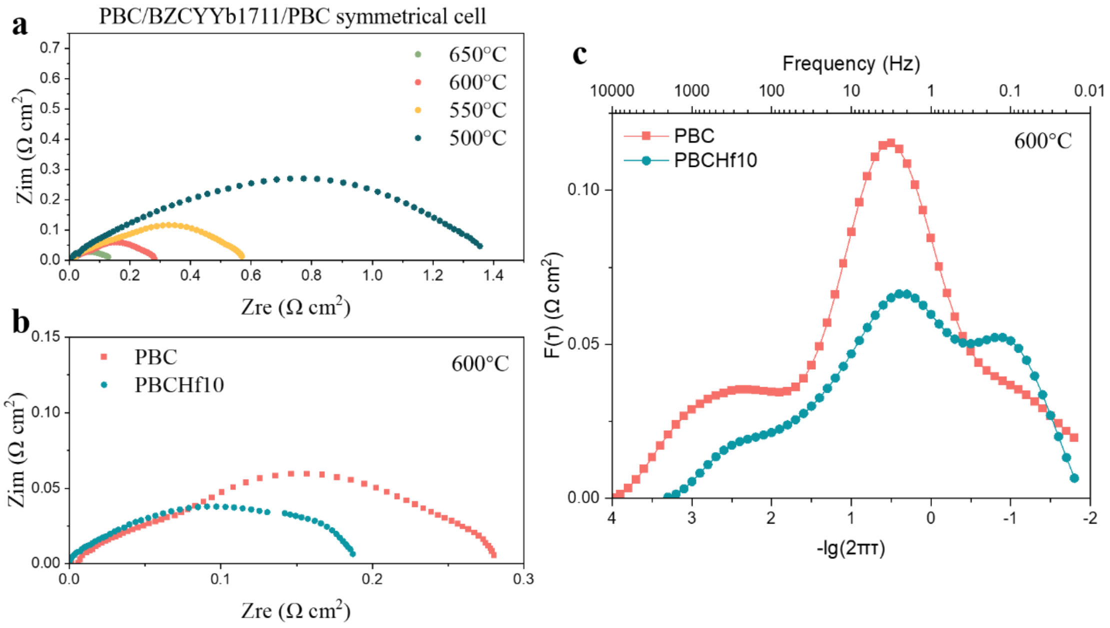

Figure S22. (a) EIS results for PBC/BZCYYb1711/PBC symmetrical cells in air at temperatures from 500 to 650 °C. (b) Comparative study of the R_p for PBC and PBCHf10 in BZCYYb1711 symmetrical cells at 600°C. (c) DRT analysis of the EIS results presented in (b).

PBC/BZCYYb1711/PBC symmetrical cells revealed R_p of 0.128, 0.280, 0.570, and 1.355 Ω cm^2 at 650, 600, 550, and 500 °C, respectively. Notably, at 600°C, PBCHf10 exhibited a lower R_p of 0.187 Ω cm^2, compared to the 0.280 Ω cm^2 observed for PBC. This indicates enhanced PI-ORR catalytic activity of PBCHf10. DRT analysis applied to the EIS results, highlights that this superior PI-ORR catalytic activity is attributed to the optimization of an elementary step, as evidenced by the medium frequency peak.

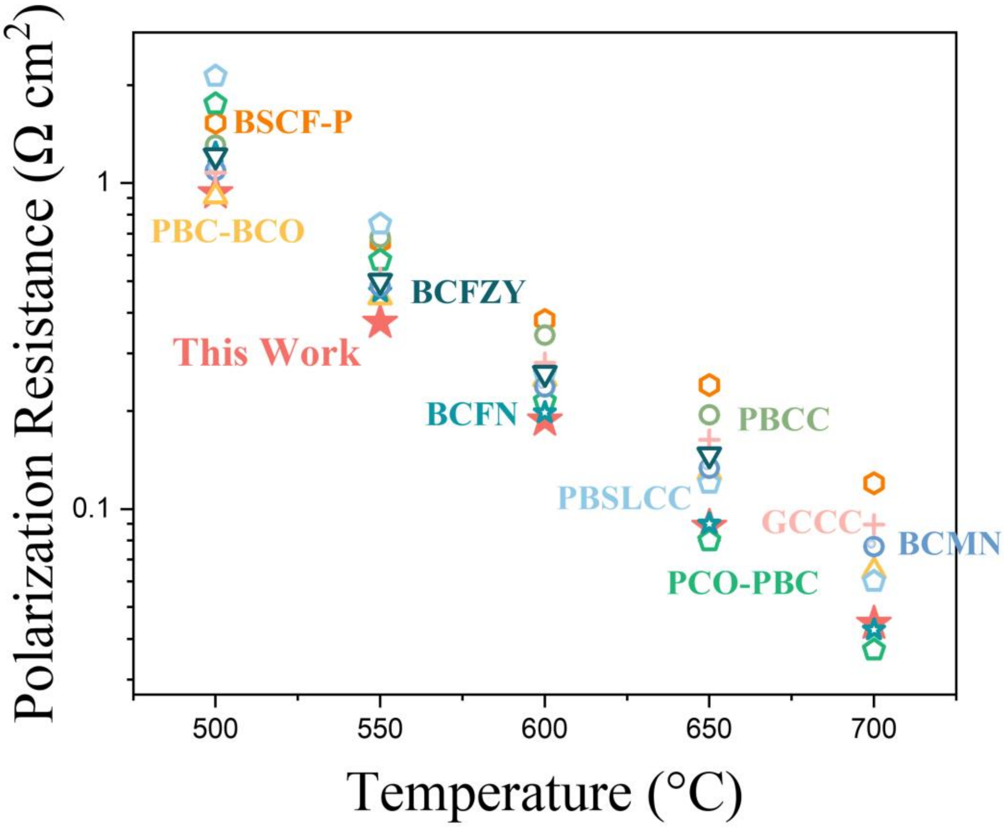

Figure S23. Comparative analysis of R_p for BZCYYb1711-based symmetrical cells with a configuration of PBCHf10/BZCYYb1711/PBCHf10 at 700-500 °C[32, 34-41].

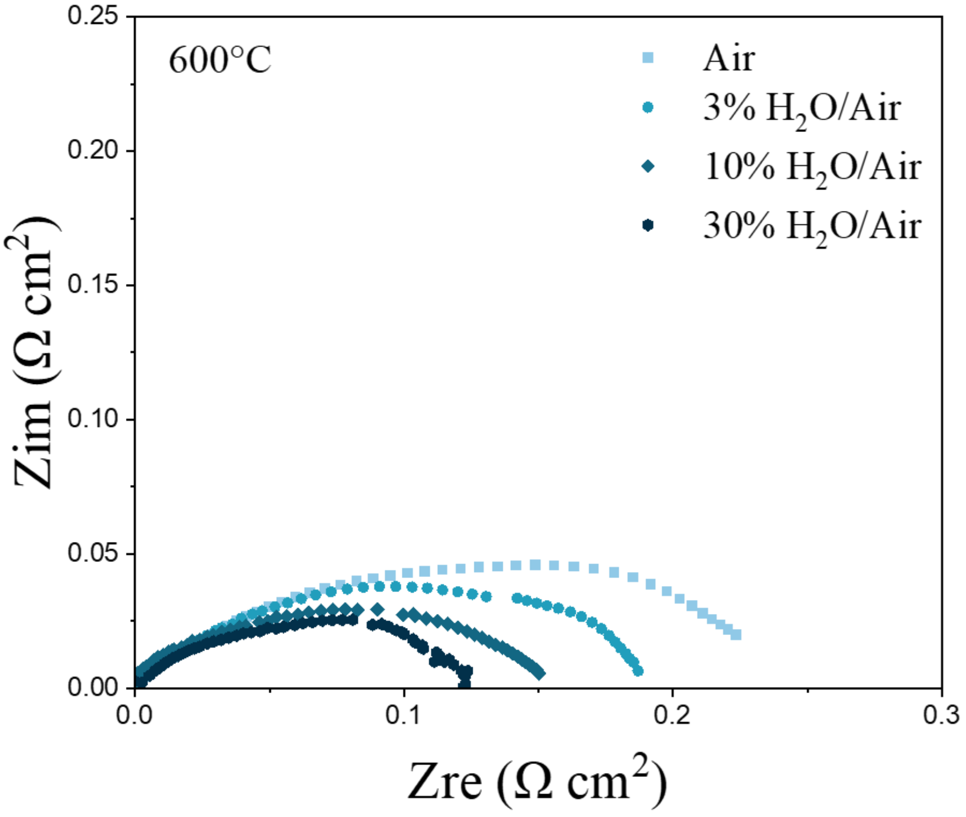

Figure S24. EIS results for PBCHf10/BZCYYb1711/PBCHf10 symmetrical cells at 600 °C under various water vapor pressures using air as the carrier gas.

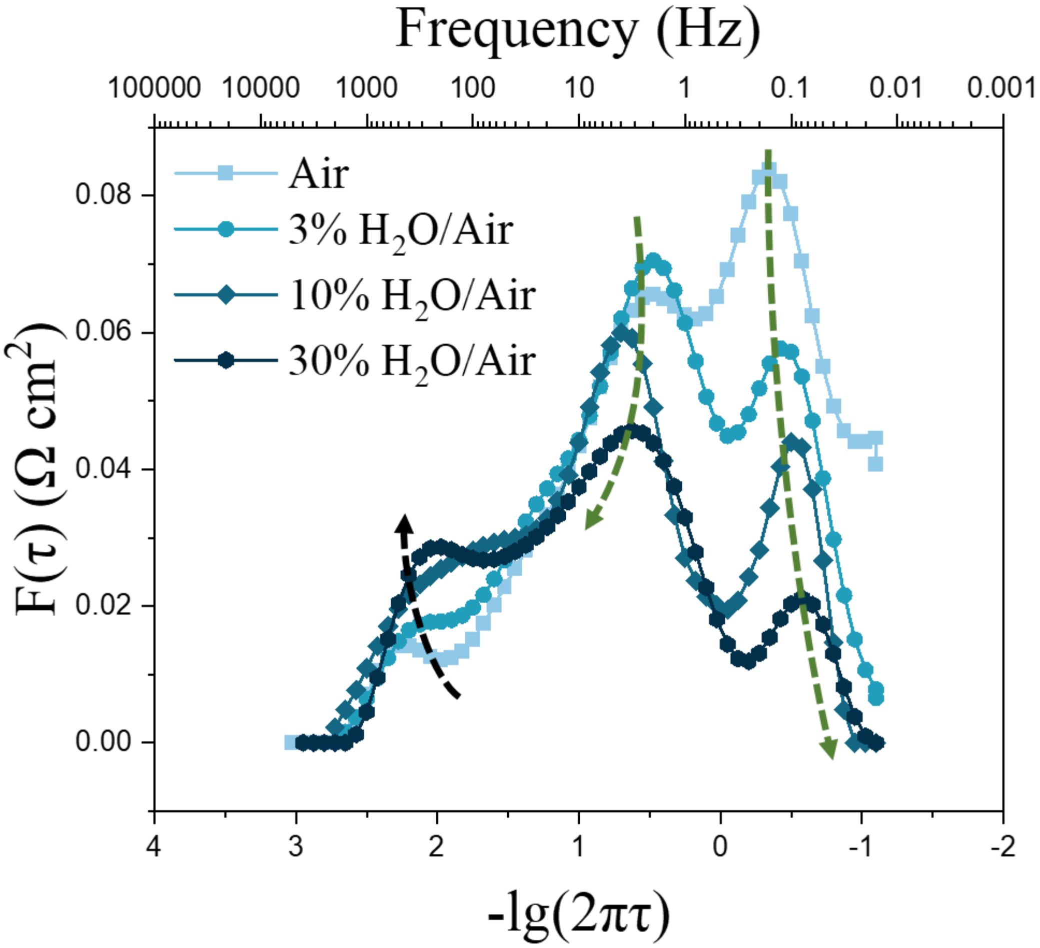

Figure S25. DRT analysis of the EIS results presented in Fig. S24, focusing on the identification of different elementary steps.

Here, the slight increase in the high frequency peaks that can be attributed to decreased oxygen partial pressure.

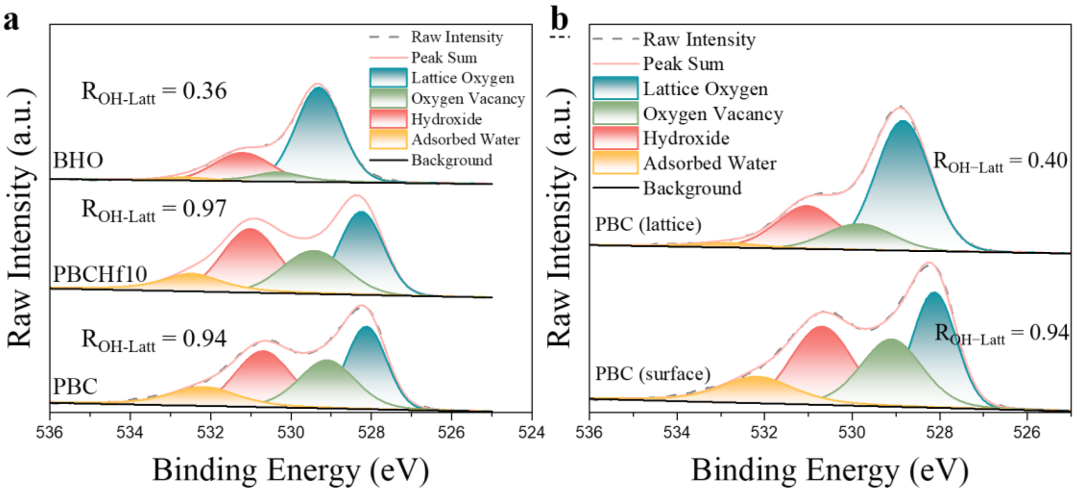

Figure S26. (a) XPS results of the surface O 1s spectrums for PBC, PBCHf10, and BHO powders. (b) XPS results of the O 1s spectrum, for the surface and lattice (bulk) of PBC, obtained from standard XPS and ion-etching techniques, respectively.

All the powder samples undergone a 24-hour pretreatment in wet air immediately prior to the XPS analysis.

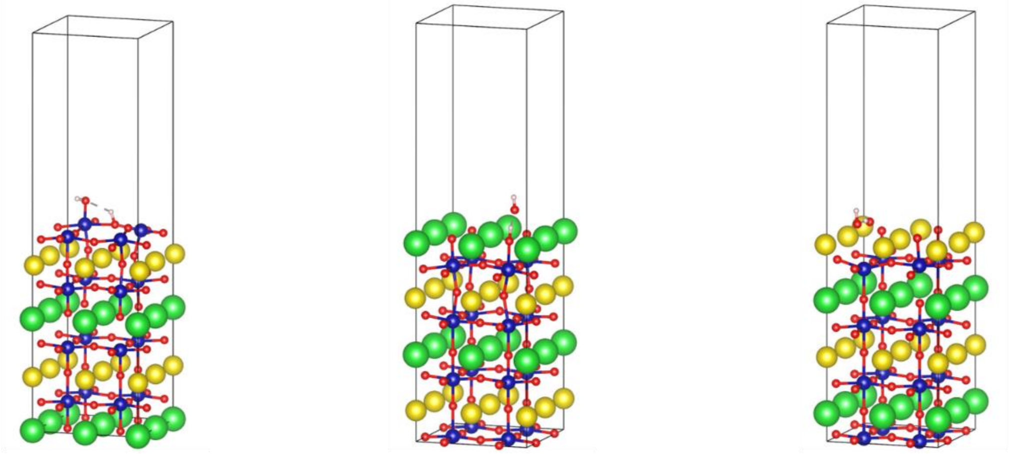

BO$_2$-terminated (001) PBC surface
$E_{\text{hydration}}$ = -1.70 eV
E_{surface} = 0.199 eV/Å^2

AO-terminated PBC (001) surface (Ba)
$E_{\text{hydration}}$ = -0.32 eV
E_{surface} = 0.201 eV/Å^2

AO-terminated PBC (001) surface (Pr)
$E_{\text{hydration}}$ = -1.82 eV
E_{surface} = 0.256 eV/Å^2

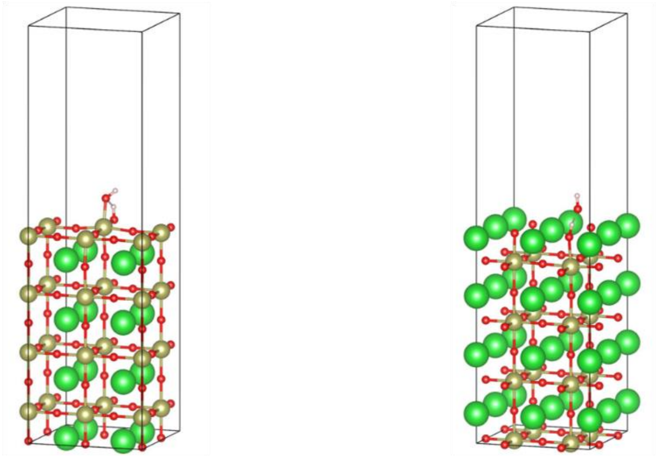

BO$_2$-terminated (001) BHO surface
$E_{\text{hydration}}$ = -1.28 eV
E_{surface} = 0.132 eV/Å^2

AO-terminated (001) BHO surface
$E_{\text{hydration}}$ = -1.02 eV
E_{surface} = 0.137 eV/Å^2

Figure S27. Surface hydration characteristics of the (001) PBC and (001) BHO surfaces.

When analyzing the surface energy (E_{surface}), it is important to note that the BO$_2$-terminated surface consistently emerges as the energetically favorable option for both PBC and BHO. Therefore, the comparison of surface hydration properties between PBC and BHO is specifically focused on the BO$_2$-terminated surface.

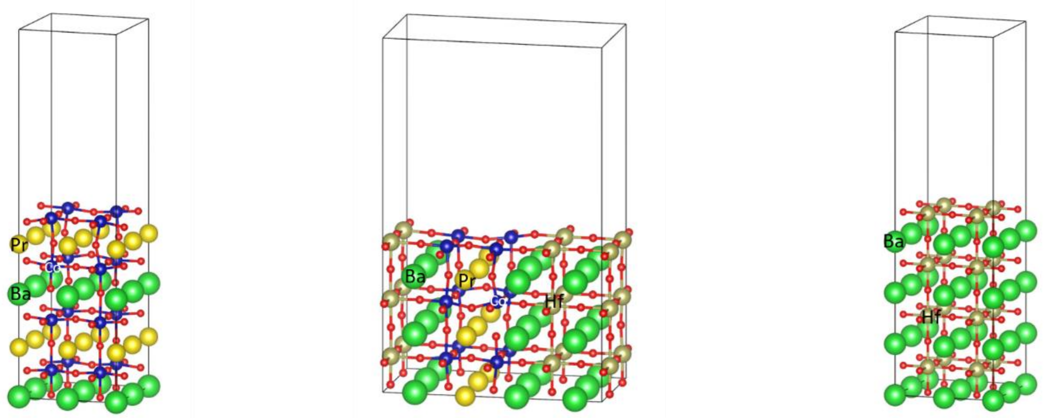

(001) BO_2-terminated $PrBaCo_2O_6$ (001) BO_2-terminated hybrid $PrBaCo_2O_6$-$BaHfO_3$ (001) BO_2-terminated $BaHfO_3$

Figure S28. Depiction of the surface structures for (001) BO_2-terminated $PrBaCo_2O_6$, the hybrid $PrBaCo_2O_6$-$BaHfO_3$, and $BaHfO_3$.

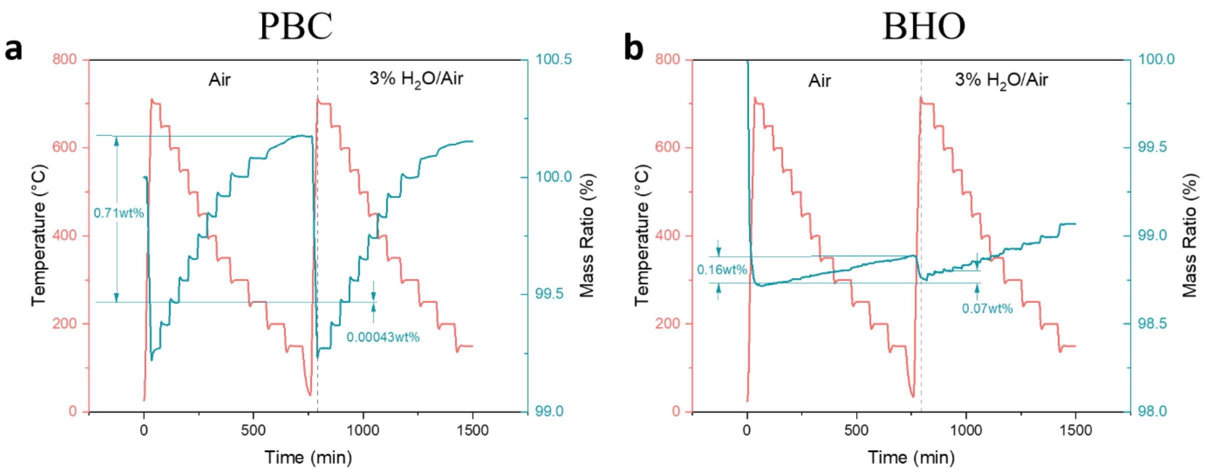

Figure S29. Programmed heating thermogravimetric analysis performed on PBC (a) and BHO (b).

Initially, the sample underwent a controlled temperature increase to 700 °C in a dry air environment to eliminate potential adsorbed species. This was followed by a stepwise cooling procedure, decreasing the temperature in 50 °C increments with 40 minutes equilibration periods, until reaching room-temperature. The observed weight changes between targeted temperatures and room temperature under dry air were attributed to weight loss resulting from the formation of oxygen vacancies. Afterward, the environment was switched to wet air, succeeded by a reheating process back to 700 °C. Employing the same cooling procedure, weight measurements at equivalent temperatures under both dry and wet conditions were taken to assess the hydration performance.

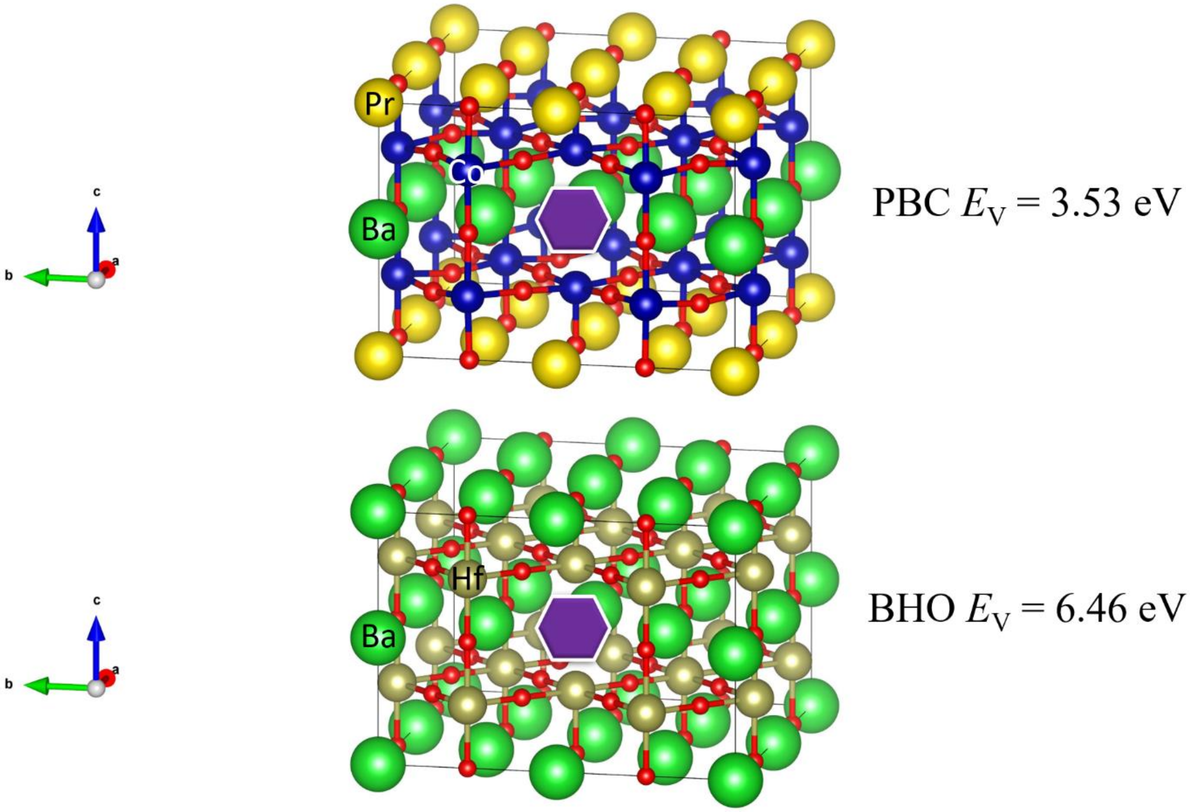

Figure S30. Oxygen vacancy formation energy (E_V) for PBC and BHO.

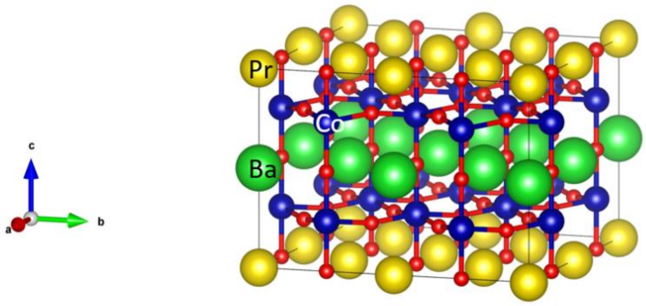

$PrBaCo_2O_6$

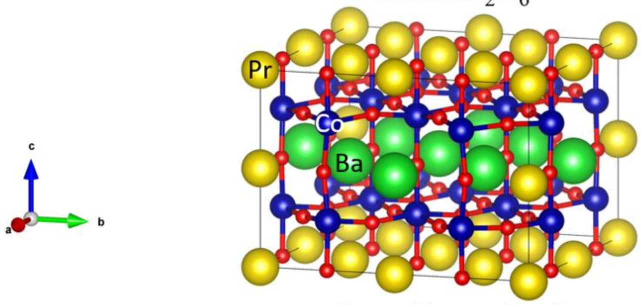

$Pr_{1.125}Ba_{0.875}Co_2O_6$

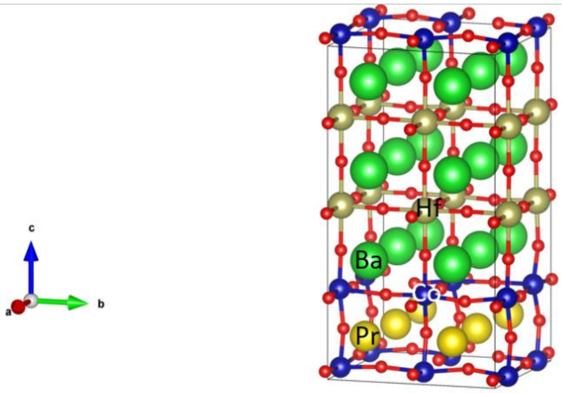

hybrid $PrBaCo_2O_6$-$BaHfO_3$

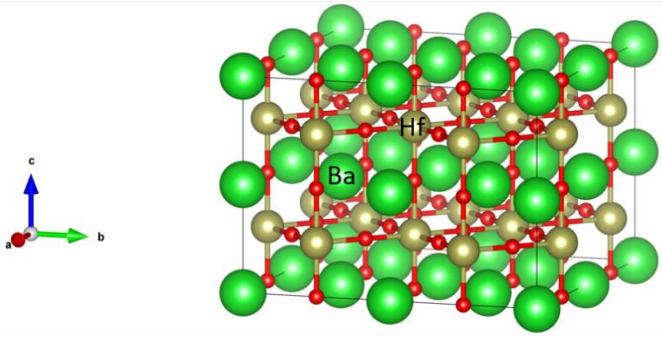

$BaHfO_3$

Figure S31. Depiction of the bulk structures for $PrBaCo_2O_6$, $Pr_{1.125}Ba_{0.875}Co_2O_6$, the hybrid $PrBaCo_2O_6$-$BaHfO_3$, and $BaHfO_3$.

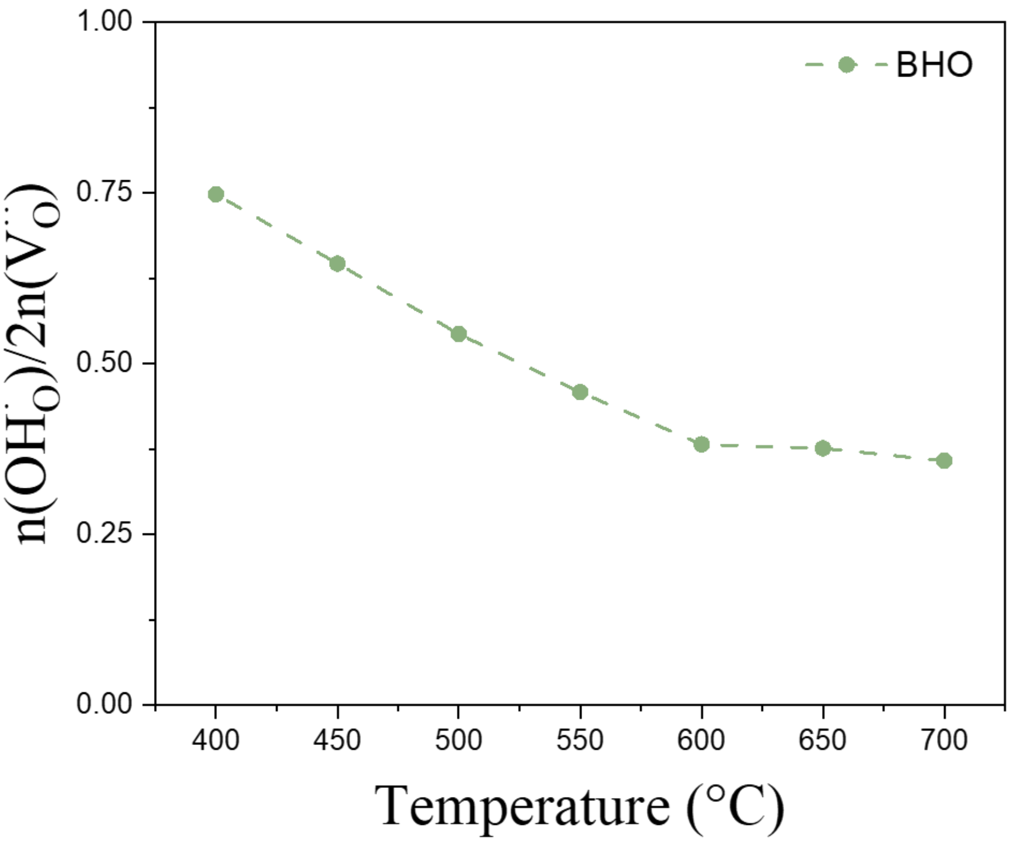

Figure S32. The percentage of oxygen vacancies contributing to proton generation in BHO.

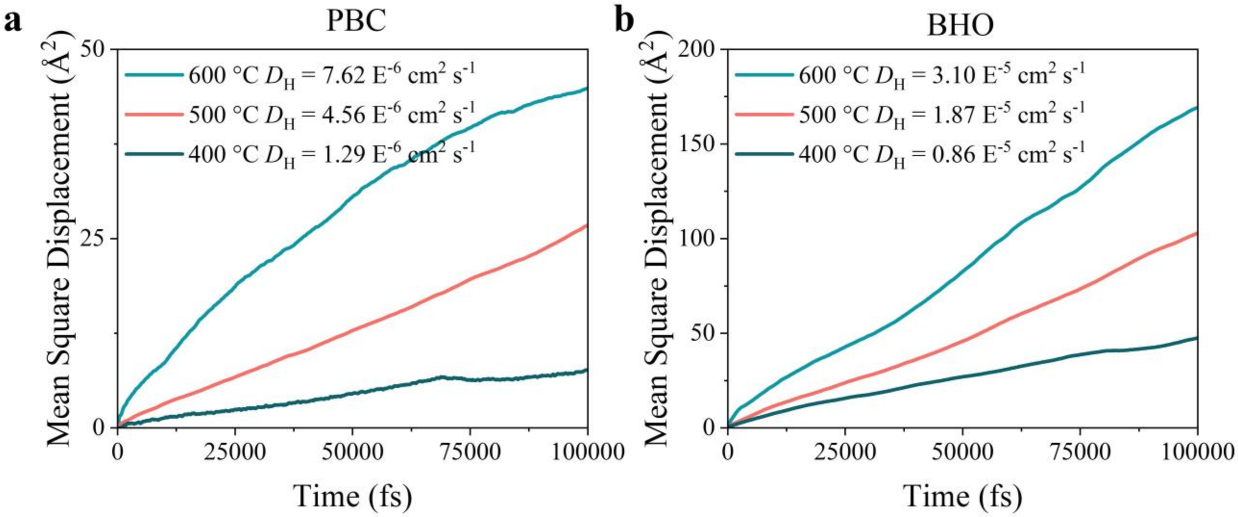

Figure S33. AIMD-simulated mean square displacements of protons in PBC and BHO at 400-600 °C.

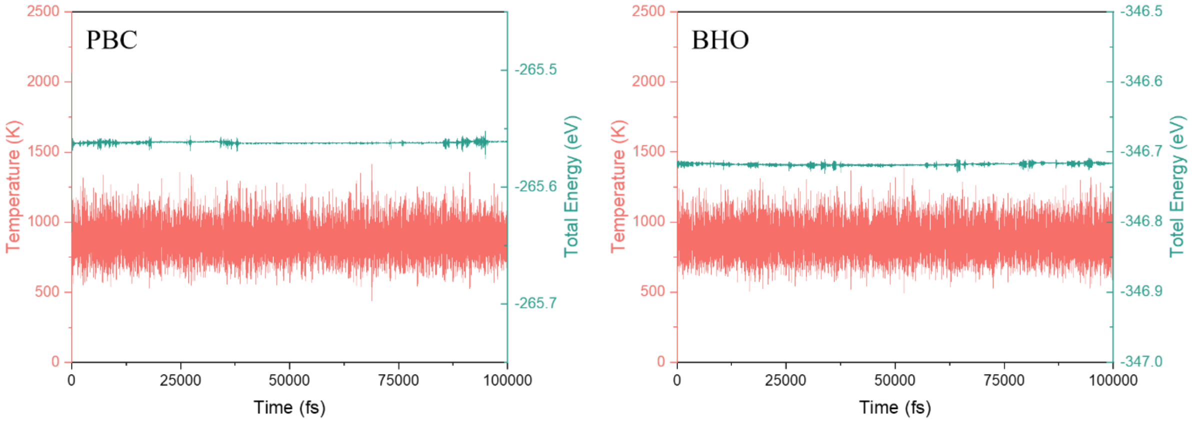

Figure S34. Variations in temperature and energy over time captured during the 100 ps AIMD simulations for both PBC and BHO at 600 °C.

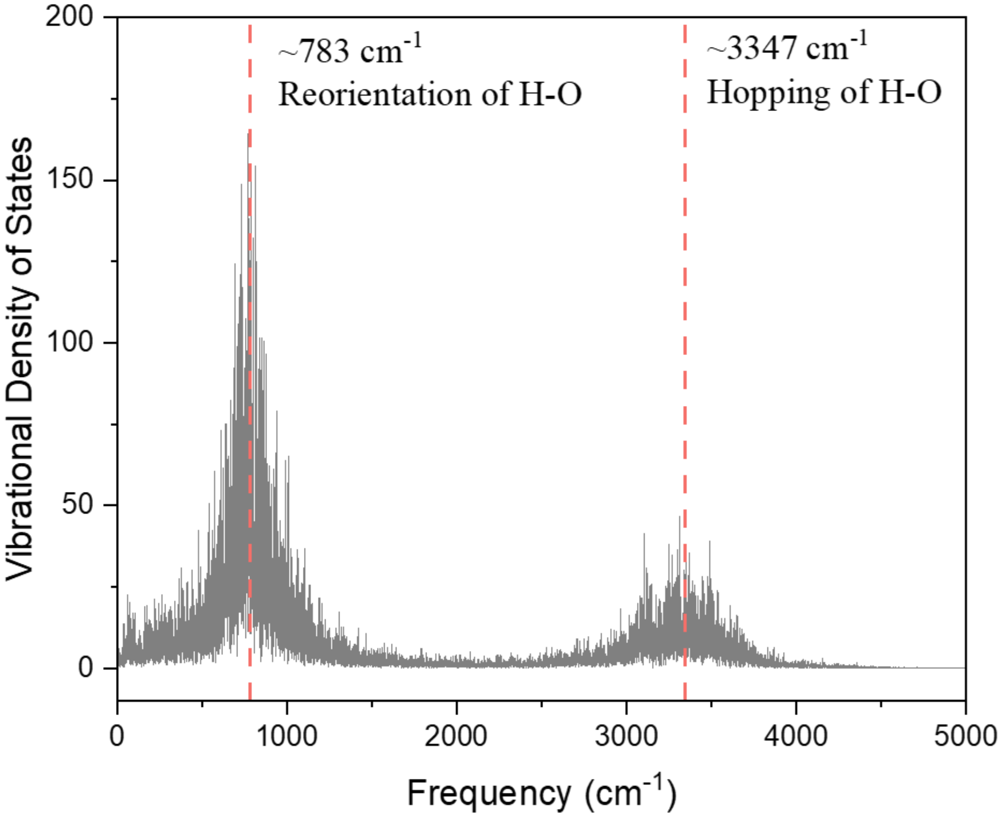

Figure S35. Vibrational density of states of protons in BHO at 600 °C.

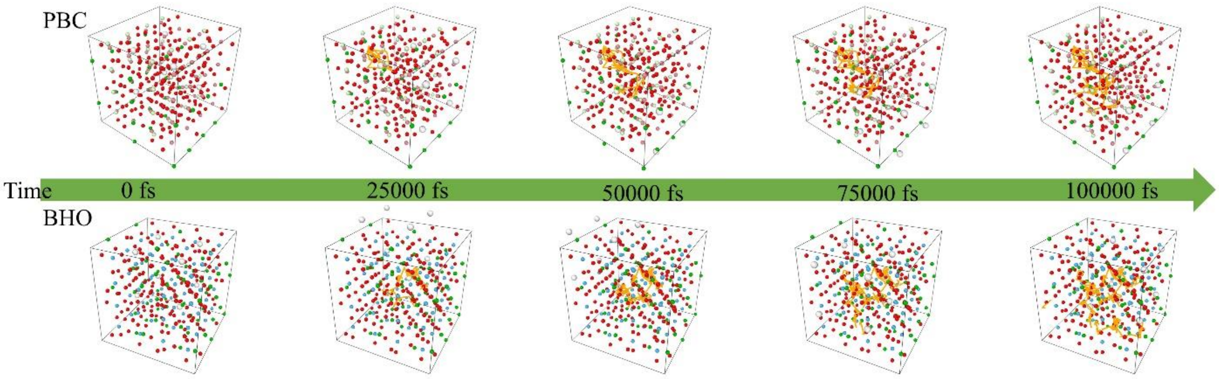

Figure S36. The trajectories of protons in PBC and BHO during 100 ps AIMD simulations at 600 °C.

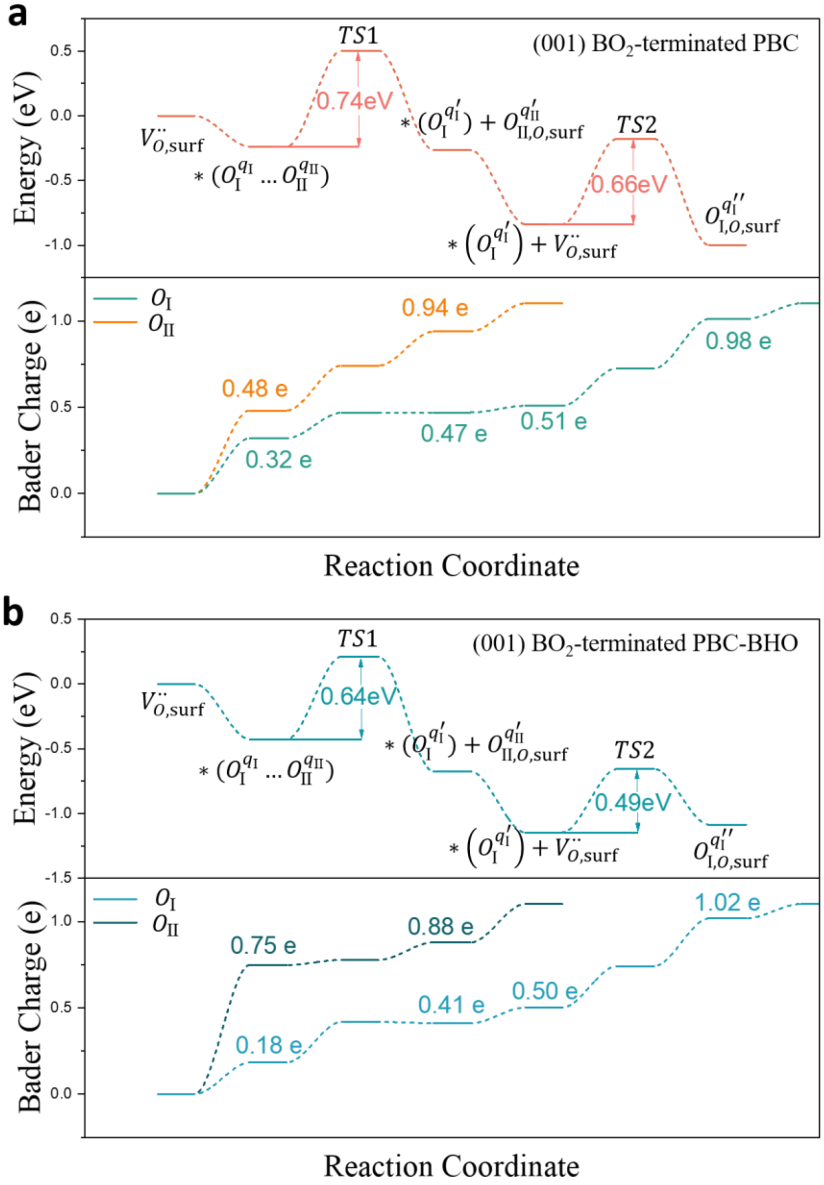

Figure S37. (a) and (b) Detailed energy profiles and variations in Bader charges for oxygen atoms O_I and O_II during ORR on BO$_2$-terminated (001) PBC surface (a) and the PBC-BHO interface (b).

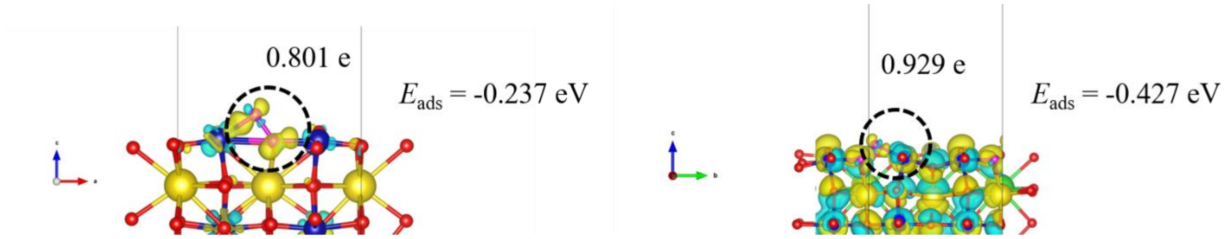

(001) BO$_2$-terminated PrBaCo$_2$O$_6$ ($* OO$) (001) BO$_2$-terminated hybrid PrBaCo$_2$O$_6$-BaHfO$_3$ ($* OO$)

Figure S38. Charge distribution differences analysis for (001) BO$_2$-terminated PrBaCo$_2$O$_6$ and the hybrid PrBaCo$_2$O$_6$-BaHfO$_3$.

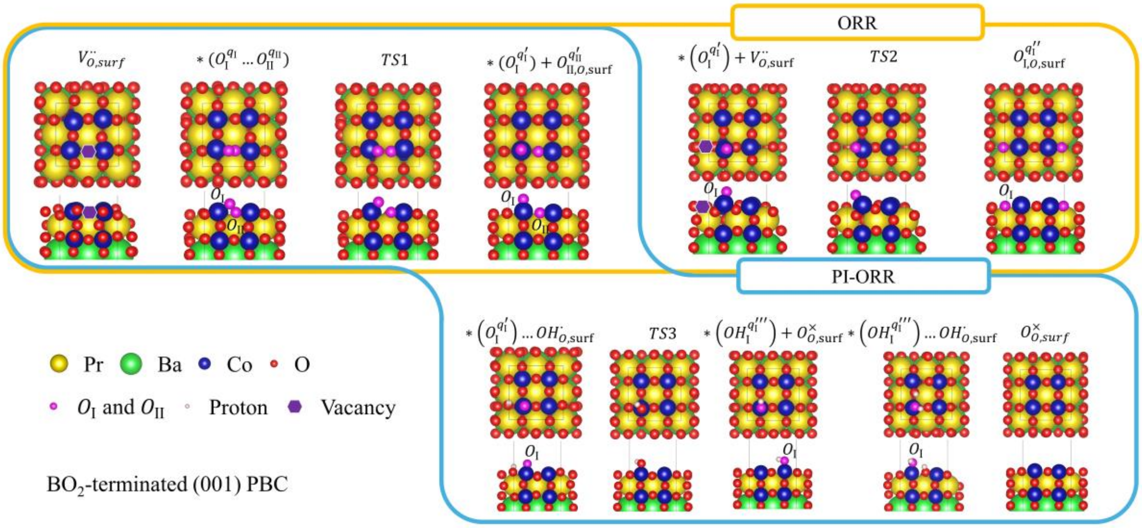

Figure S39. Top and side views of the configurations during ORR and PI-ORR on BO_2-terminated (001) PBC surface.

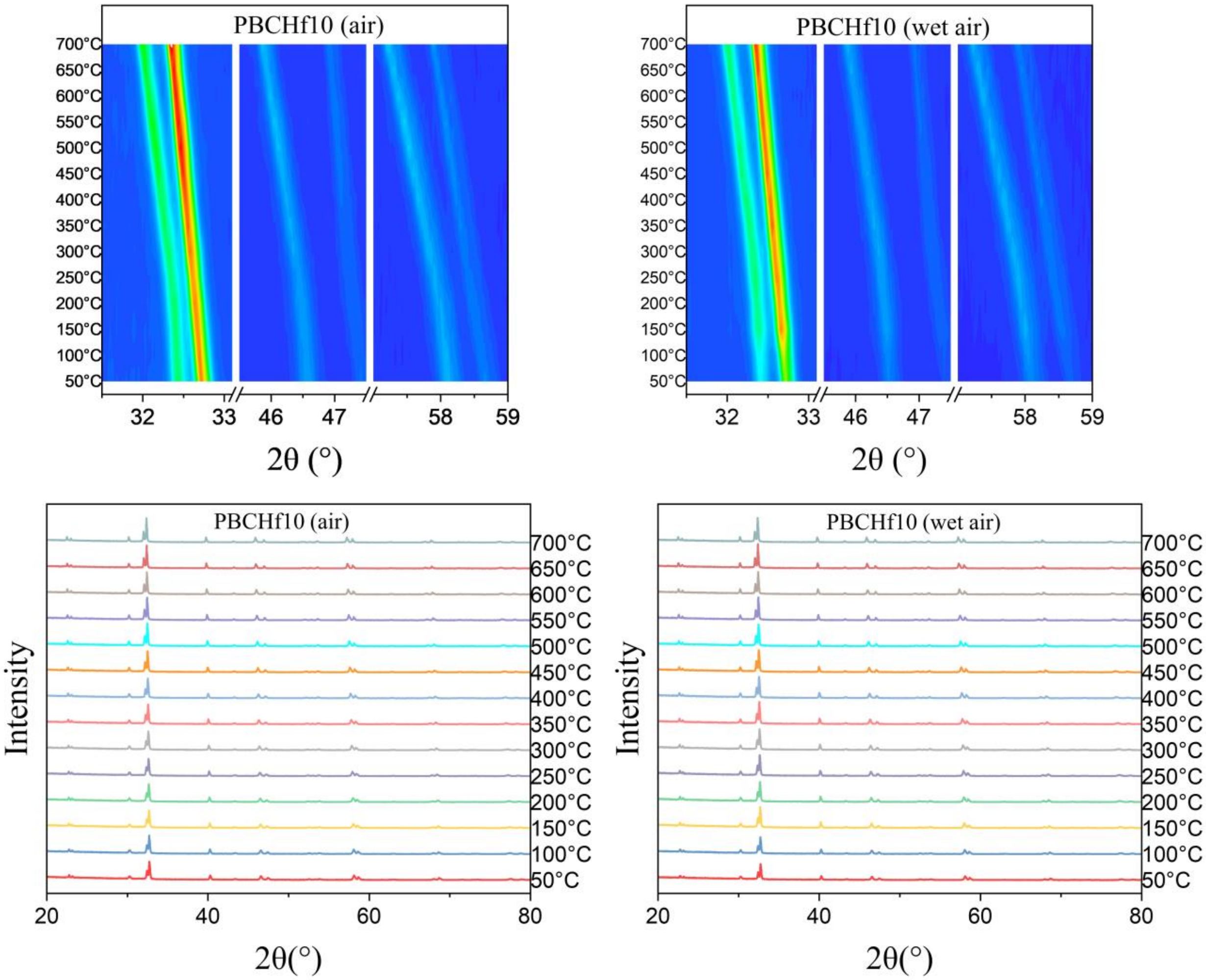

Figure S40. Contour plots and full profile of in-situ XRD patterns for PBCHf10 when exposed to both dry and wet air.

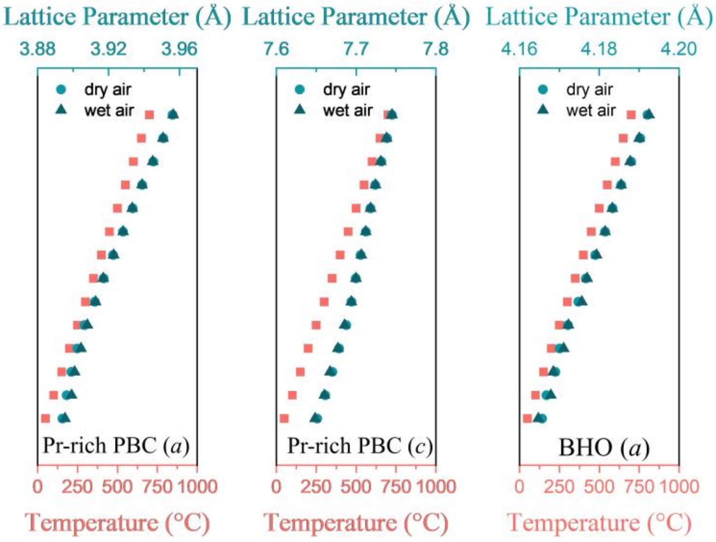

Figure S41. Rietveld refinement obtained lattice parameters for Pr-rich PBC and BHO under both air and wet air conditions.

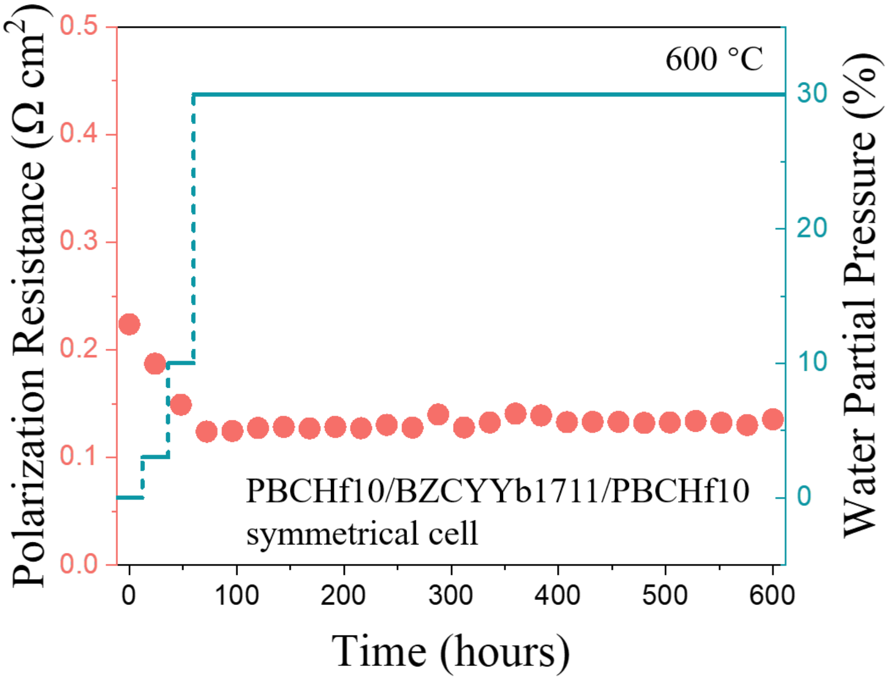

Figure S42. Long-term durability test of the PBCHf10/BZCYYb1711/PBCHf10 symmetrical cell at 600 °C under air with 30% water vapor pressure.

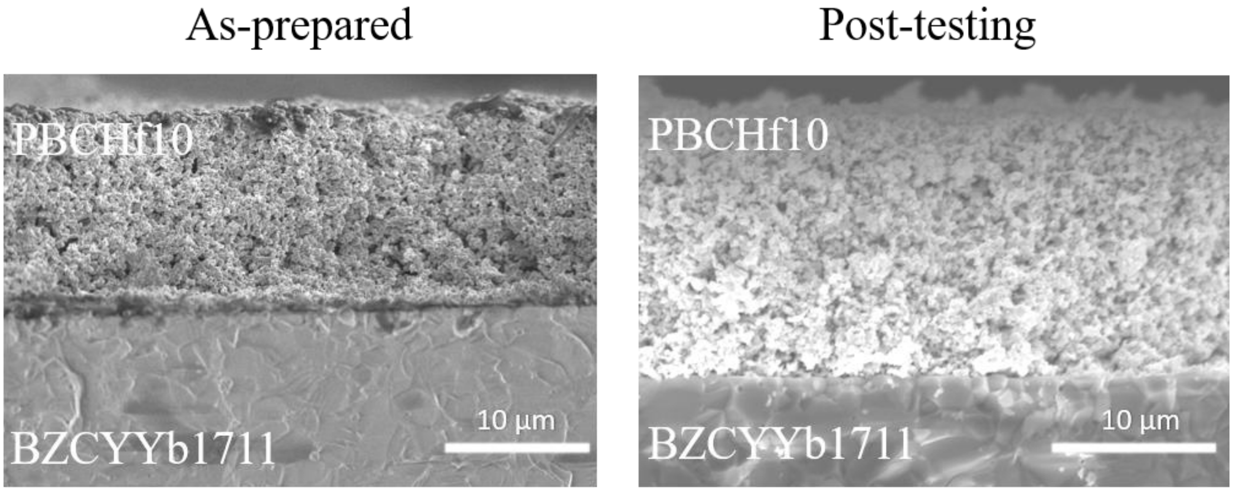

Figure S43. Cross-sectional SEM images comparing the as-prepared symmetrical cells with those after long-term stability testing, specifically following the test shown in Fig. S42.

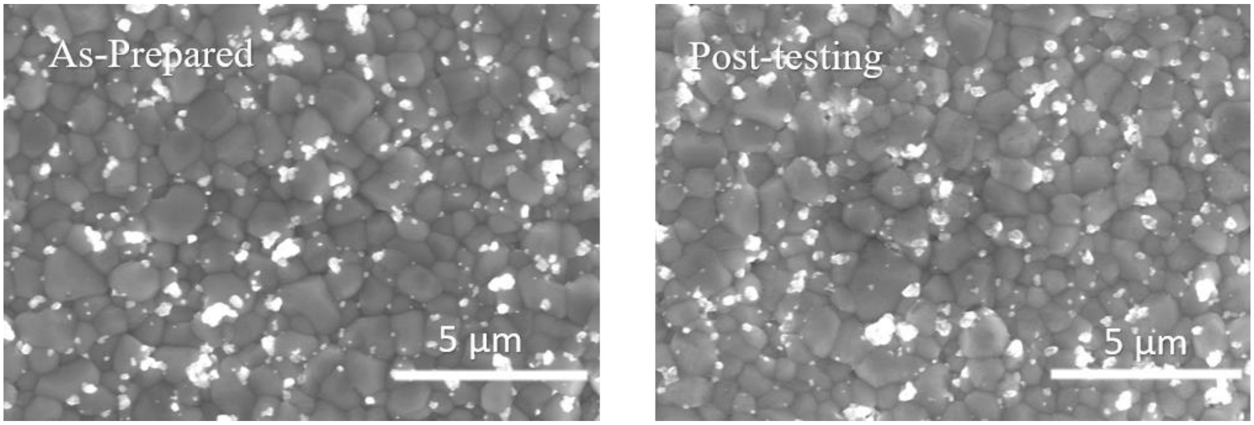

Figure S44. Surface SEM images of strip samples, both in their initial state and after exposure to air containing 30% water vapor pressure for 500 hours.

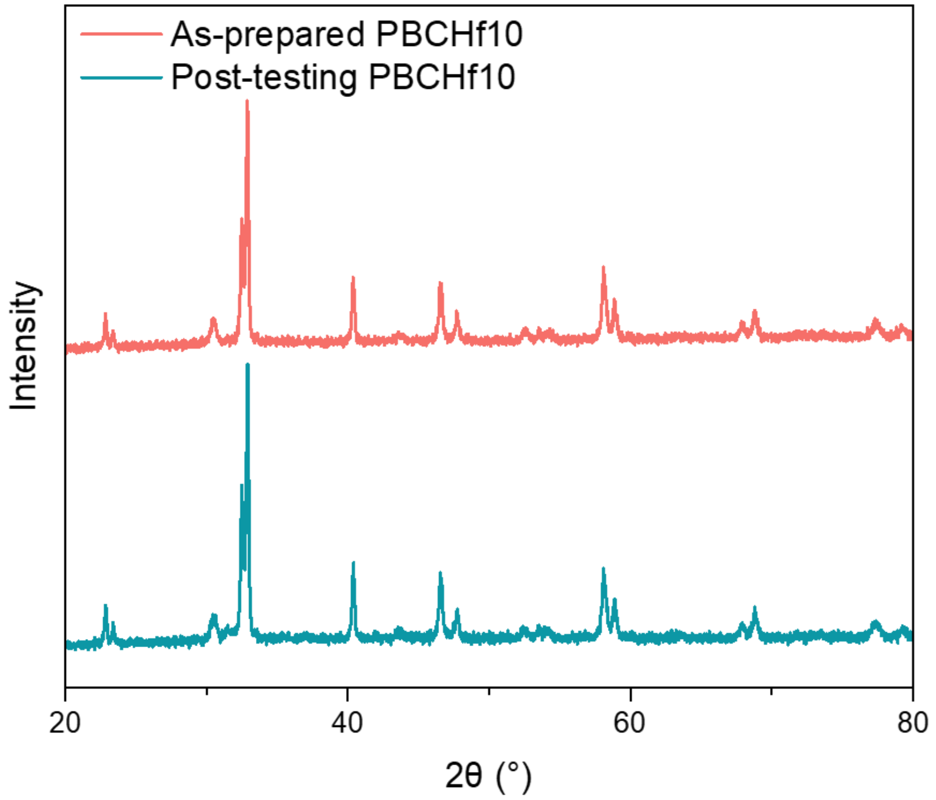

Figure S45. XRD patterns of the as-prepared oxygen electrode (PBCHf10) and those after long-term stability testing, specifically following the test shown in Fig. S42.

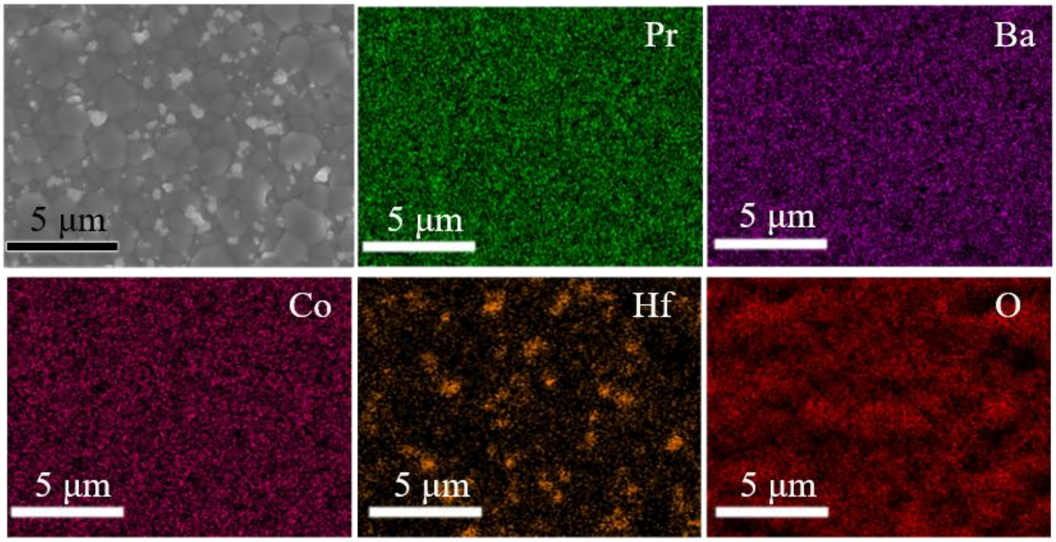

Figure S46. SEM images detailing the surfaces of PBCHf10 strip samples, accompanied by corresponding EDS mapping. The measurements for TEC and ECR will be conducted using this strip sample.

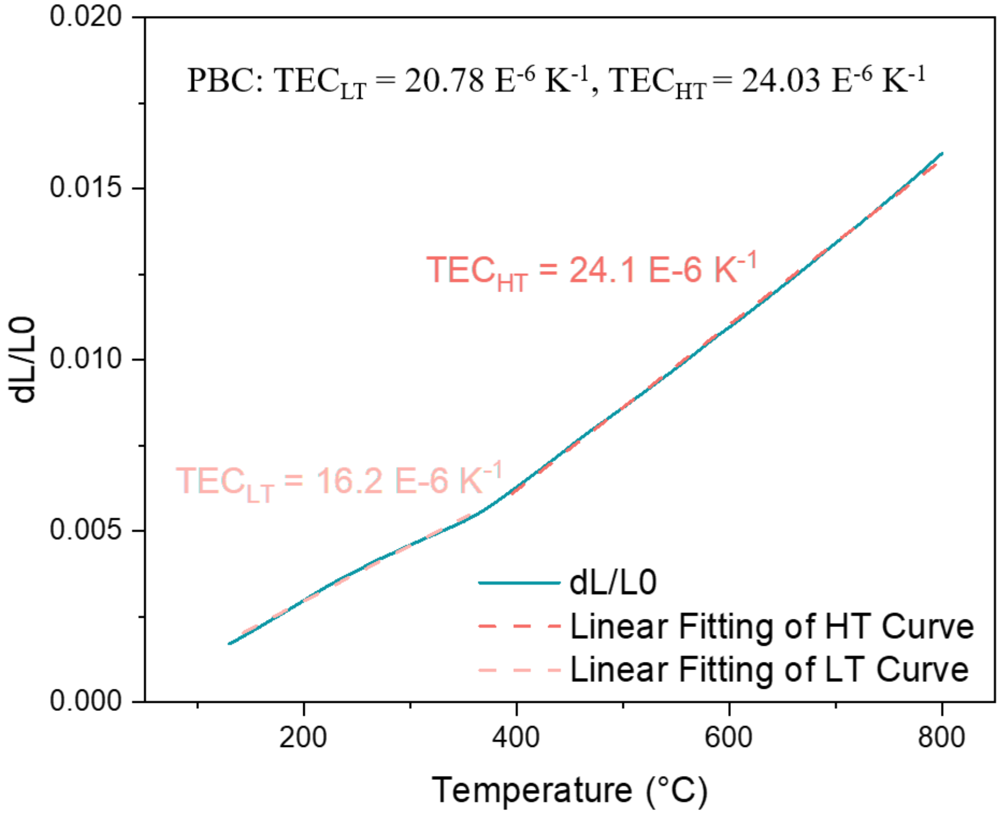

Figure S47. Thermal expansion curves for PBCHf10, with linear fitting results marked, covering temperature ranges from room temperature to 400°C and from 400 °C to 800 °C. Results from the literature for PBC are provided alongside for direct comparison[18].

The TEC curve exhibits an inflection behavior, recording values of 16.2 E^{-6} K^{-1} below 400 °C and 24.1 E^{-6} K^{-1} above 400 °C. This variation is attributed to the change in the spin state of cobalt ions with elevated temperatures. Compared with PBC, PBCHf10 demonstrates a significantly lower TEC at temperatures below 400 °C while maintaining comparable values above 400 °C[18], indicating a closer compatibility with the current state-of-the-art electrolyte material, such as SDC and BZCYYb1711[24].

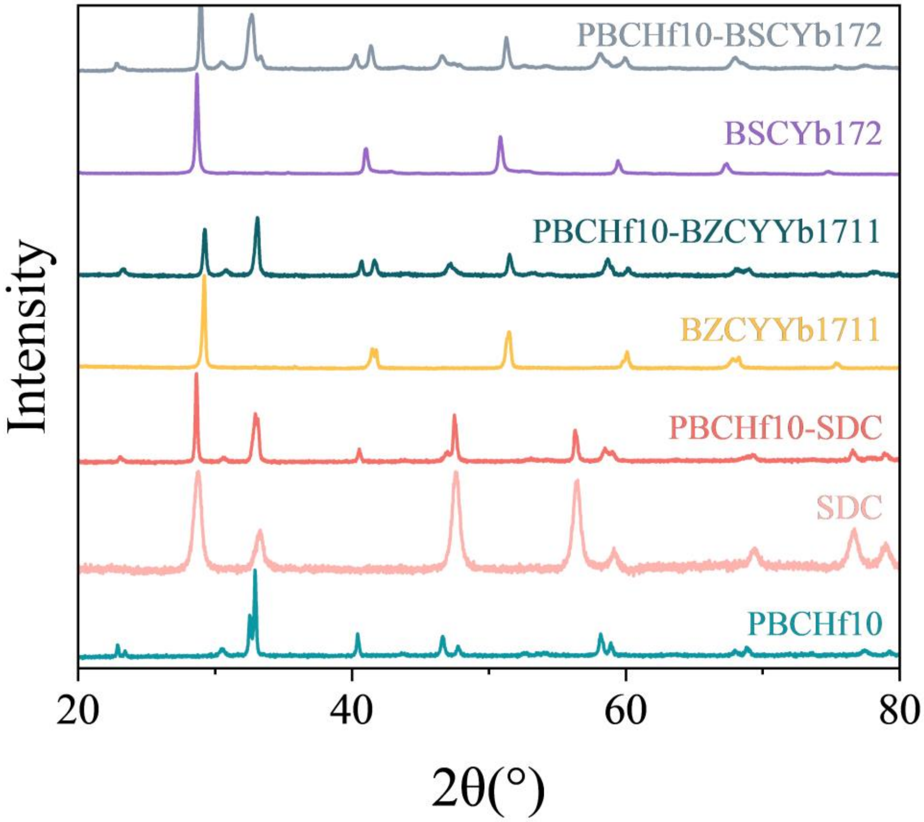

Figure S48. XRD patterns demonstrating the chemical compatibility between PBCHf010 and three electrolyte materials: SDC, BZCYYb1711, and BSCYb172.

The XRD patterns for the composite powder can be attributed to either PBCHf10 or the electrolyte, with no formation of secondary phases. This indicates excellent chemical compatibility between PBCHf10 and the electrolyte materials.

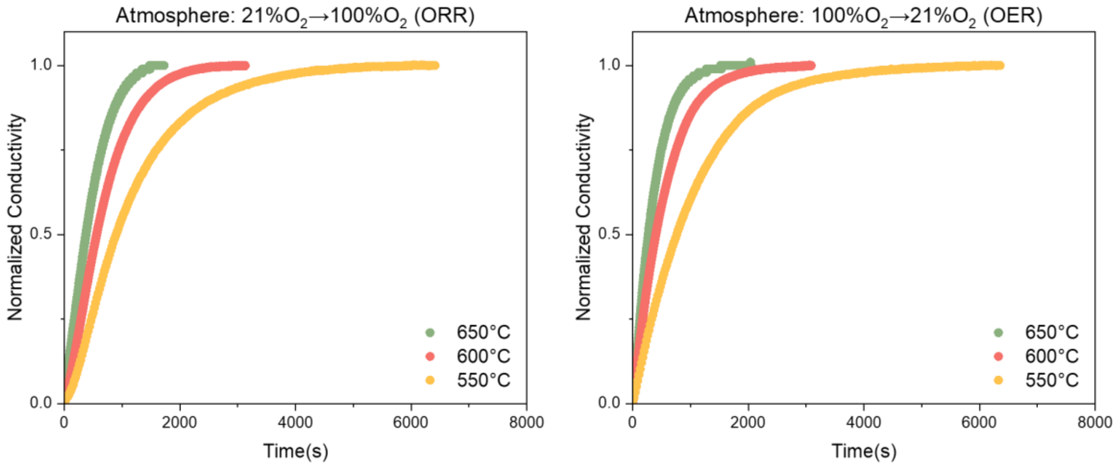

Figure S49. Normalized conductivity curves for PBCHf10 measured between 550 °C and 650 °C during ECR experiments. It features scenarios with elevated oxygen partial pressure (ORR) and decreased oxygen partial pressure (OER).

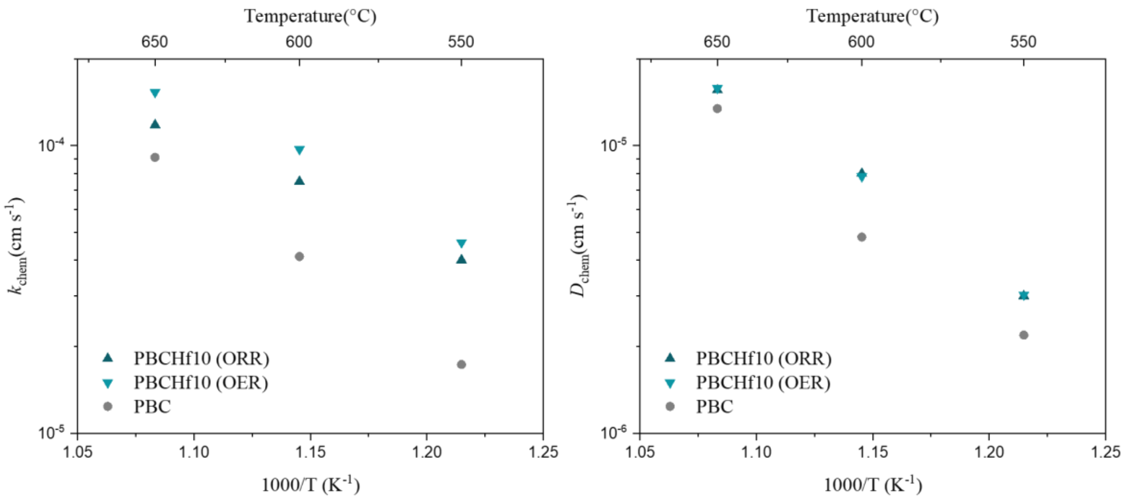

Figure S50. k_{Chem}, and D_{Chem} for PBCHf010, evaluated between 550 °C and 650 °C. These metrics are assessed under conditions of elevated oxygen partial pressure (ORR) and decreased oxygen partial pressure (OER). Results from the literature for PBC (ORR) are provided alongside for direct comparison[18].

Specifically, at 600 °C, PBCHf10 demonstrated comparable D_{Chem} values for ORR (8.0 E^{-6} cm^2 s^{-1}) and OER (7.8 E^{-6} cm^2 s^{-1}). However, a notable difference was observed in the k_{Chem} values, with ORR registering at 7.5 E^{-5} cm s^{-1} and OER at higher 9.7 E^{-5} cm s^{-1}. Notably, it significantly surpassing the performance of pristine PBC in both k_{Chem} (4.1E^{-5} cm s^{-1}) and D_{Chem} (4.8 E^{-6} cm^2 s^{-1})[18].

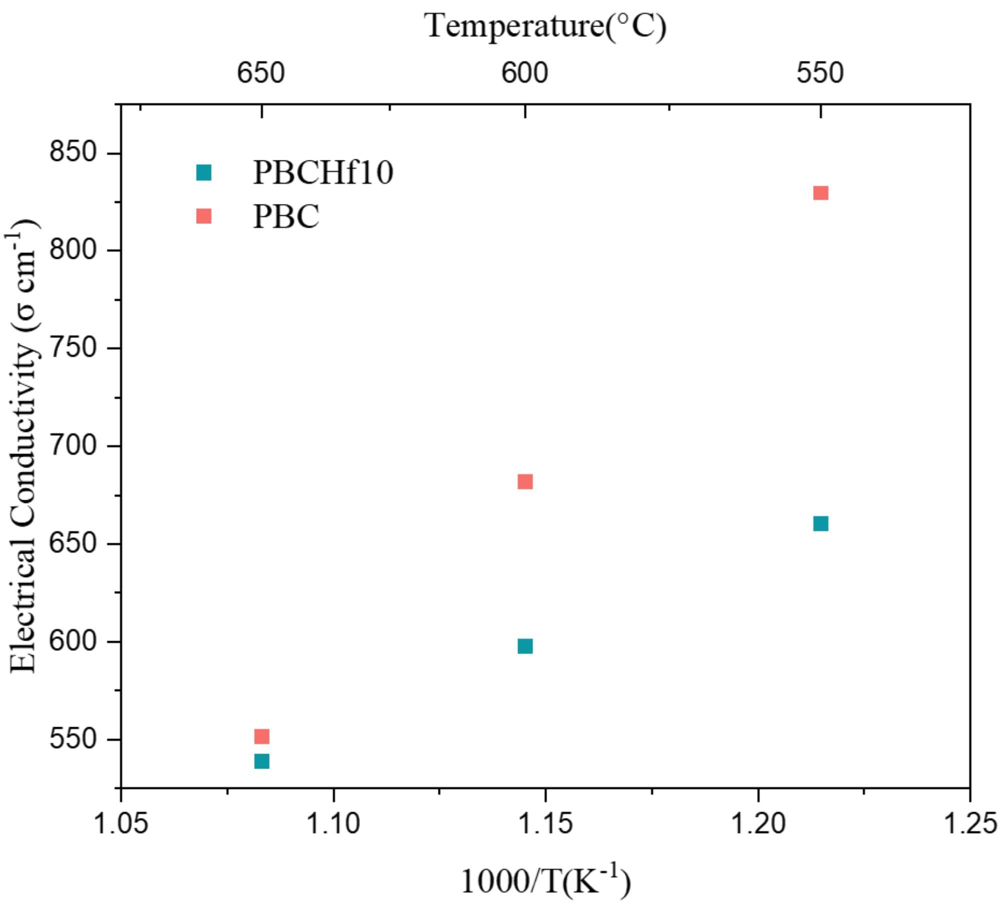

Figure S51. Electrical conductivity of PBCHf010 between 550 °C and 650 °C. Results from the literature for PBC are provided alongside for direct comparison[18].

PBCHf10 possessed a marginally lower electrical conductivity compared to pristine PBC. Nevertheless, both materials exhibited a reduction in conductivity with elevated temperatures. Importantly, PBCHf10 maintained a conductivity above 500 S cm^{-1} below 650 °C, highlighting its excellent current collection efficiency, a desirable attribute for large-scale commercial applications[25].

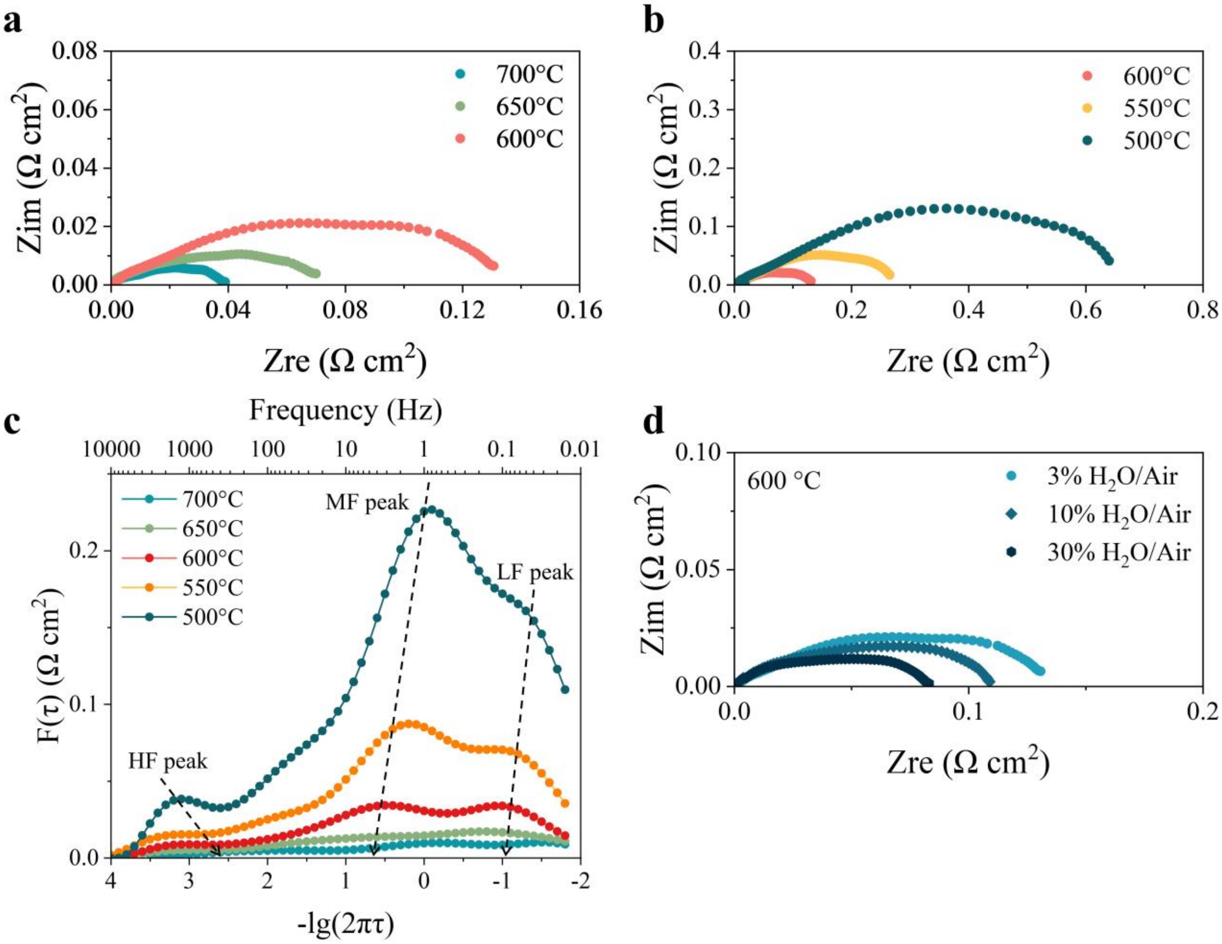

Figure S52. (a) and (b) EIS results for PBCHf10/BSCYb172/PBCHf10 symmetrical cells exposed to wet air in the temperature range of 500 to 700 °C. (c) DRT analysis of the EIS results presented in (a) and (b). (d) EIS results for PBCHf10/BSCYb172/PBCHf10 symmetrical cells exposed to air with different partial pressure of water vapor at 600 °C.

The electro-catalytic activity of PBCHf10 as the oxygen electrode in PBCHf10/BSCYb172/PBCHf10 symmetrical cells was characterized using EIS (Fig. S52a and S52b). At 700, 650, 600, 550, and 500 °C, the estimated R_p values are 0.039, 0.070, 0.131, 0.265, and 0.640 Ω cm^2, respectively, smaller than those obtained for

PBCHf10/BZCYYb1711/PBCHf10 symmetrical cells (Fig. S21a and b). The results suggest that as expected, the R_p values (and hence the electro-catalytic activity) depends on electrolyte materials used in the symmetrical cells. However, DRT analysis indicates that the mechanism of the electrode process is independent of the electrolyte materials, as the contributions from the three major steps, resolved in the frequency domain, remain consistent (Fig. S52c). Furthermore, the dependence of R_p on the partial pressure of water vapor is similar. The R_p values decreases from 0.131 to 0.109 and then to 0.083 Ω cm^2 as the water vapor pressure increases from 3% to 10% and 30%.

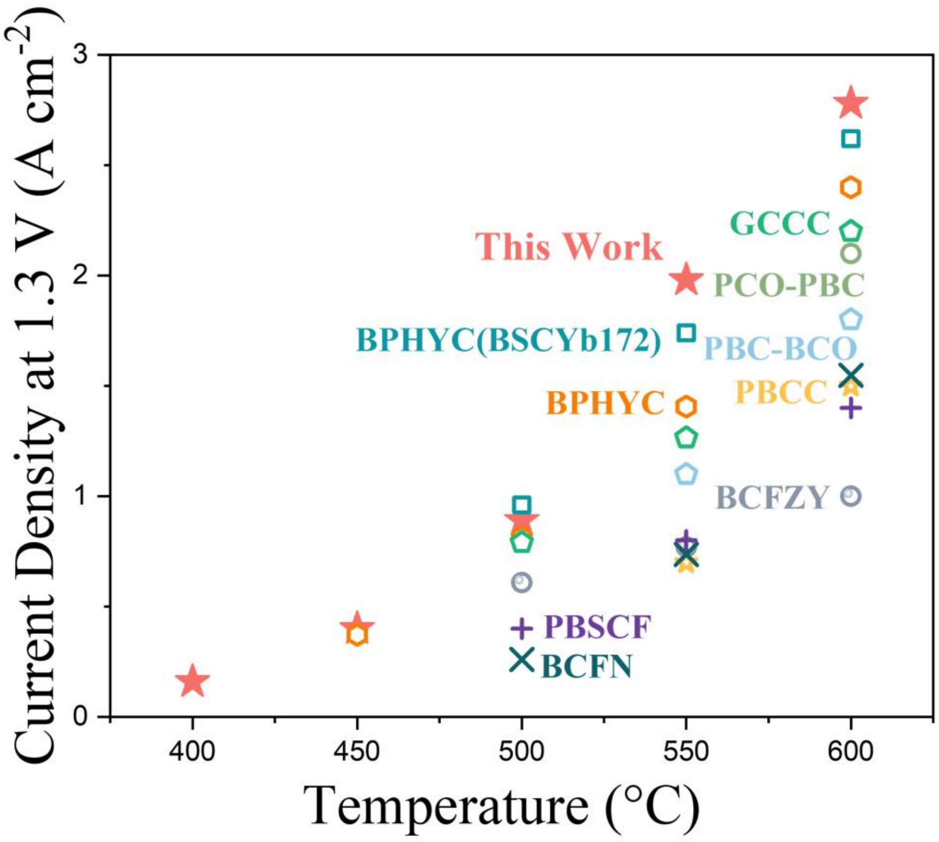

Figure S53. Comparative analysis of current densities at 1.3 V for PCECs at 700-400 °C[26-34].

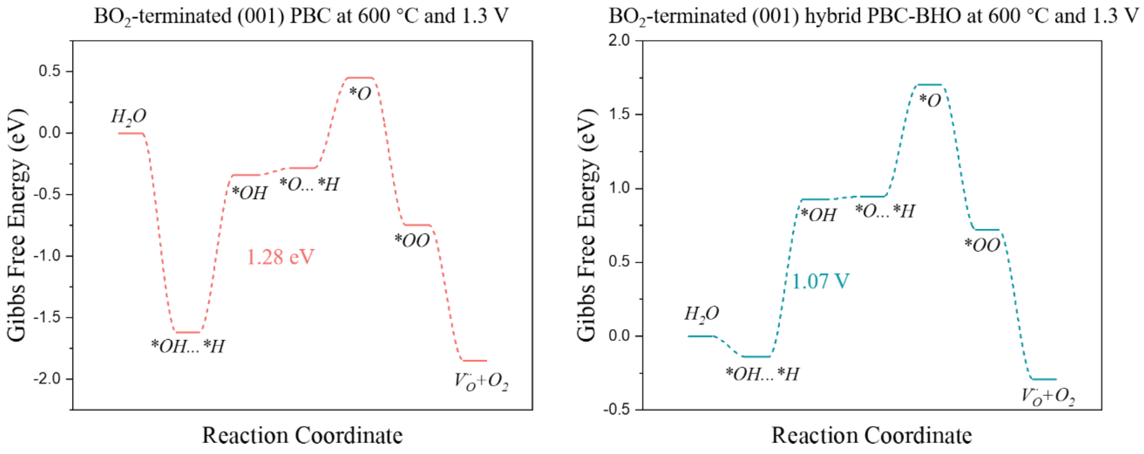
BO$_2$-terminated (001) PBC at 600 °C and 1.3 V

BO$_2$-terminated (001) hybrid PBC-BHO at 600 °C and 1.3 V

Figure S54. Energy profile for PI-OER process on BO$_2$-terminated (001) PBC and the hybrid PBC-BHO surfaces at 600 °C and 1.3 V.

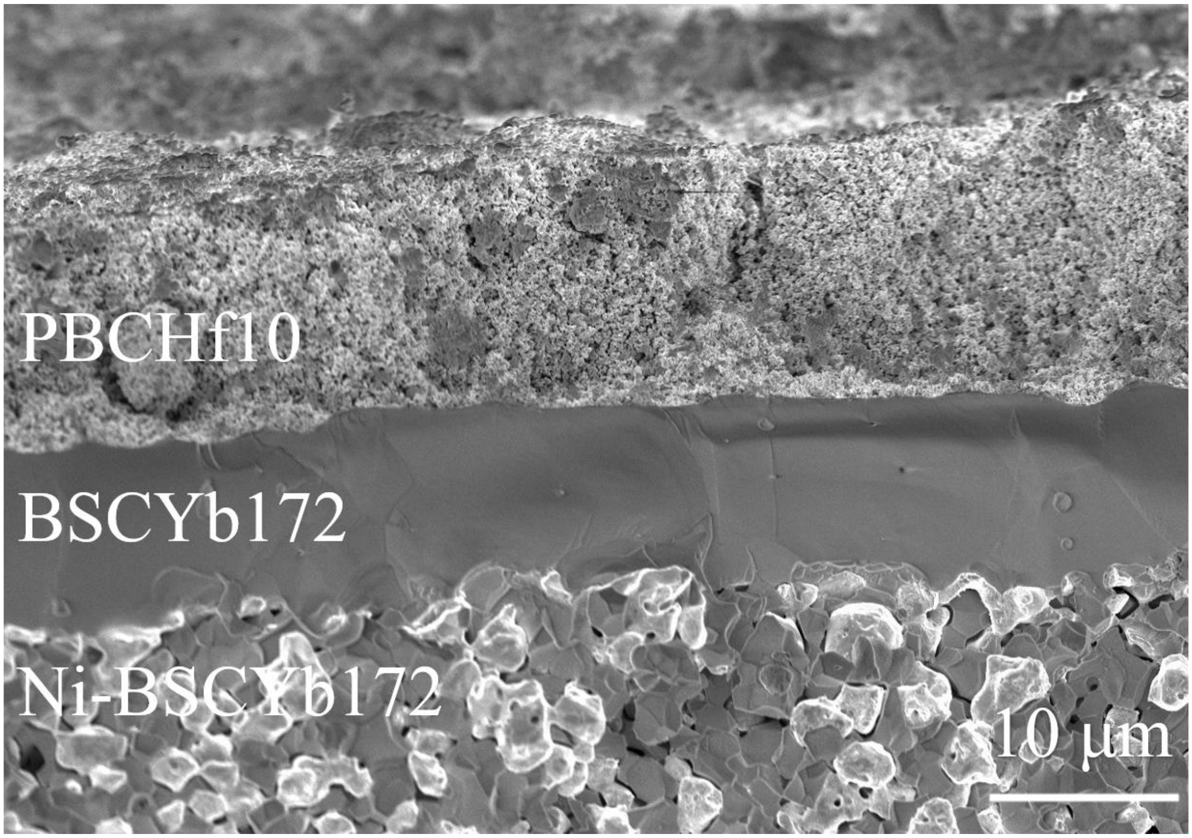

Figure S55. Cross-sectional SEM image of the single cell post long-term durability testing, specifically following the test shown in Fig. 5i.

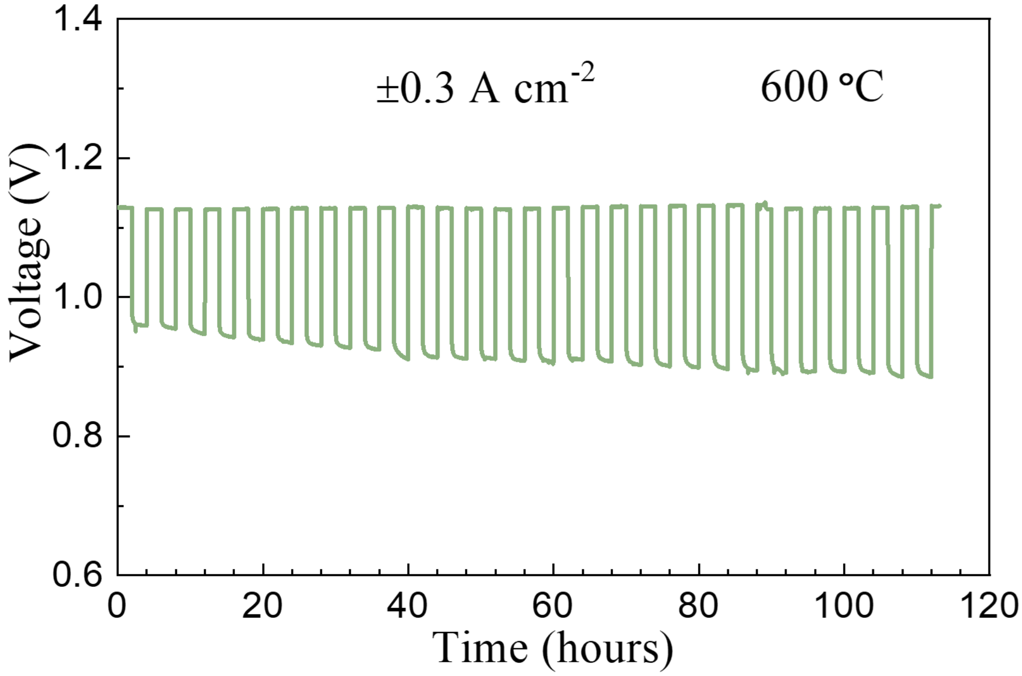

Figure S56. Long-term reversible operation durability of PBCHf10 single cell: The cell voltage variations over time when the operating mode is alternated between fuel cell and electrolysis every 2 hours, with 3% water vapor pressure present in the oxygen electrode.

Table 1. Pseudopotential and U_{eff} applied in the high-throughput calculation

Element	Pseudopotential	*U*eff (eV)
Ba	Ba_sv 06Sep2000	0
Sr	Sr_sv 07Sep2000	0
Pr	Pr_3 07Sep2000	0
Mn	Mn_pv 02Aug2007	3.9
Fe	Fe_pv 02Aug2007	5.3
Co	Co 02Aug2007	3.32
Ni	Ni_pv 06Sep2000	6.2
Cu	Cu_pv 06Sep2000	0
Al	Al 04Jan2001	0
As	As 22Sep2009	0
Bi	Bi 08Apr2002	0
Ca	Ca_sv 06Sep2000	0
Ce	Ce 23Dec2003	0
Cr	Cr_pv 02Aug2007	3.7
Dy	Dy_3 06Sep2000	0
Er	Er_3 06Sep2000	0
Eu	Eu_3 20Oct2008	0
Ga	Ga_d 06Jul2010	0
Gd	Gd_3 06Sep2000	0
Ge	Ge_d 03Jul2007	0
Hf	Hf_pv 06Sep2000	0

Ho	Ho_3 06Sep2000	0
In	In 08Apr2002	0
La	La 06Sep2000	0
Lu	Lu_3 06Sep2000	0
Mg	Mg_pv 13Apr2007	0
Mo	Mo_pv 04Feb2005	4.38
Nb	Nb_pv 08Apr2002	0
Nd	Nd_3 06Sep2000	0
Pb	Pb 08Apr2002	0
Sb	Sb 06Sep2000	0
Sc	Sc_sv 07Sep2000	0
Sm	Sm_3 07Sep2000	0
Sn	Sn_d 06Sep2000	0
Ta	Ta_pv 07Sep2000	0
Tb	Tb_3 06Sep2000	0
Te	Te 08Apr2002	0
Ti	Ti_pv 07Sep2000	0
Tm	Tm_3 20Jan2003	0
V	V_pv 07Sep2000	3.25
W	W 08Apr2002	0
Y	Y_sv 25May2007	0
Yb	Yb_2 06Sep2000	0
Zn	Zn 06Sep2000	0

Zr	Zr_sv 04Jan2005	0
O	O 08Apr2002	0

Table 2. Decomposition analysis results for Ti and Zr-doped PBC

	Doping Content	Decomposition Product 1 (Fraction)	Decomposition Product 2 (Fraction)	Decomposition Product 3 (Fraction)	Decomposition Product 4 (Fraction)	Decomposition Product 5 (Fraction)
Ti-doped PBC	0.0625	Pr8Ti4O20, mp-1195324 (0.1)	Ba4Co4O12, mp-18965 (0.5)	Co6O8, mp-1271793 (0.0875)	Pr4Co4O12, mp-20090 (0.25)	Pr16O24, mp-16705 (0.0625)
	0.125	Pr8Ti4O20, mp-1195324 (0.2)	Ba4Co4O12, mp-18965 (0.5)	Co6O8, mp-1271793 (0.175)	Null	Pr16O24, mp-16705 (0.125)
	0.1875	Pr8Ti4O20, mp-1195324 (0.3)	Ba4Co4O12, mp-18965 (0.5)	Co6O8, mp-1271793 (0.0875)	Co4O4, mp22408 (0.05)	Pr16O24, mp-16705 (0.0625)
	0.25	Pr8Ti4O20, mp-1195324 (0.4)	Ba4Co4O12, mp-18965 (0.5)	Null	Co4O4, mp22408 (0.1)	Null
	0.3125	Pr8Ti4O20, mp-1195324 (0.4)	Ba4Co4O12, mp-18965 (0.375)	Co6O8, mp-1271793 (0.0875)	Co4O4, mp22408 (0.05)	Ba8Ti4O20, mp-3397 (0.0875)

	0.375	Pr8Ti4O20, mp-1195324 (0.4)	Ba4Co4O12, mp-18965 (0.25)	Co6O8, mp-1271793 (0.175)	Null	Ba8Ti4O20, mp-3397 (0.175)
	0.4375	Pr8Ti4O20, mp-1195324 (0.4)	Ba4Co4O12, mp-18965 (0.1875)	Co6O8, mp-1271793 (0.175)	BaTiO3, mp-5020 (0.0625)	Ba8Ti4O20, mp-3397 (0.175)
	0.5	Pr8Ti4O20, mp-1195324 (0.4)	Ba4Co4O12, mp-18965 (0.125)	Co6O8, mp-1271793 (0.175)	BaTiO3, mp-5020 (0.125)	Ba8Ti4O20, mp-3397 (0.175)
Zr-doped PBC	0.0625	Pr4Co4O12, mp-559426 (0.4375)	BaZrO3, mp-3834 (0.0625)	Ba4Co4O12, mp-18965 (0.5)	Null	Null
	0.125	Pr4Zr4O14, mp-559426 (0.1375)	Null	Ba4Co4O12, mp-18965 (0.5)	Pr16O24, mp-16705 (0.1875)	Co6O8, mp-1271793 (0.175)
	0.1875	Pr4Zr4O14, mp-559426 (0.1375)	BaZrO3, mp-3834 (0.0625)	Ba4Co4O12, mp-18965 (0.4375)	Pr16O24, mp-16705 (0.1875)	Co6O8, mp-1271793 (0.175)
	0.25	Pr4Zr4O14, mp-559426 (0.1375)	BaZrO3, mp-3834 (0.125)	Ba4Co4O12, mp-18965 (0.375)	Pr16O24, mp-16705 (0.1875)	Co6O8, mp-1271793 (0.175)

	0.3125	Pr4Zr4O14, mp-559426 (0.1375)	BaZrO3, mp-3834 (0.1875)	Ba4Co4O12, mp-18965 (0.3215)	Pr16O24, mp-16705 (0.1875)	Co6O8, mp-1271793 (0.175)
	0.375	Pr4Zr4O14, mp-559426 (0.1375)	BaZrO3, mp-3834 (0.25)	Ba4Co4O12, mp-18965 (0.25)	Pr16O24, mp-16705 (0.1875)	Co6O8, mp-1271793 (0.175)
	0.4375	Pr4Zr4O14, mp-559426 (0.1375)	BaZrO3, mp-3834 (0.3125)	Ba4Co4O12, mp-18965 (0.1875)	Pr16O24, mp-16705 (0.1875)	Co6O8, mp-1271793 (0.175)
	0.5	Pr4Zr4O14, mp-559426 (0.1375)	BaZrO3, mp-3834 (0.375)	Ba4Co4O12, mp-18965 (0.125)	Pr16O24, mp-16705 (0.1875)	Co6O8, mp-1271793 (0.175)

Table 3. Summary of Rietveld refinement results for high-temperature XRD under air and wet air

Air					
Temperature (°C)	Rwp (%)	Rp (%)	*a* of d-PBC (Å)	*c* of d-PBC (Å)	*a* of BHO (Å)
50	11.11	8.6	3.89574	7.6511	4.1653
100	11.8	9.06	3.89613	7.661	4.1664
150	11.64	9.01	3.89895	7.6699	4.1687
200	11.7	8.83	3.902	7.6776	4.1696
250	11.98	9.11	3.9064	7.6876	4.1721
300	11.6	8.82	3.91189	7.6936	4.1744
350	11.75	9.05	3.9167	7.6988	4.1761
400	11.56	8.77	3.9224	7.7055	4.1789
450	11.09	8.52	3.92732	7.7105	4.1805
500	11.25	8.56	3.93329	7.7175	4.183
550	10.75	8.19	3.93861	7.7234	4.1851
600	11.34	8.74	3.94491	7.731	4.1877
650	11.19	8.63	3.95079	7.7387	4.1902
700	10.68	8.15	3.9561	7.7449	4.1921
Wet air					
Temperature (°C)	Rwp (%)	Rp (%)	*a* of d-PBC (Å)	*c* of d-PBC (Å)	*a* of BHO (Å)
50	11.73	9.04	3.89580	7.6493	4.1651

100	11.81	9.14	3.89843	7.6591	4.1669
150	11.70	9.12	3.90073	7.6668	4.1680
200	12.15	9.34	3.90418	7.6765	4.1709
250	11.89	9.05	3.90775	7.6850	4.1719
300	11.84	8.90	3.91190	7.6927	4.1748
350	11.74	8.97	3.91650	7.6986	4.1763
400	11.50	8.70	3.92276	7.7066	4.1793
450	11.74	8.94	3.92726	7.7106	4.1805
500	11.50	8.77	3.93331	7.7180	4.1832
550	11.54	8.77	3.93863	7.7237	4.1852
600	11.76	8.96	3.94463	7.7305	4.1874
650	11.42	8.67	3.95067	7.7381	4.1900
700	11.66	8.90	3.95606	7.7444	4.1921

Table 4. Summary of the current landscape of identified promising PCECs with their electrochemical performance under fuel cell mode

		Peak Power Density (W cm^{-2})						Ref
Electrode	Electrolyte	700 °C	650 °C	600 °C	550 °C	500 °C	450 °C	
PBCHf010	BSCYb172			1.49	1.29	0.93	0.6	This Work
$Ba_{0.9}Pr_{0.1}Hf_{0.1}Y_{0.1}Co_{0.8}O_{3-\delta}$	BSCYb172			1.57	1.21	0.82	0.52	26
$Ba_{0.9}Pr_{0.1}Hf_{0.1}Y_{0.1}Co_{0.8}O_{3-\delta}$	BZCYYb1711			1.37	0.96	0.62		27
$PrNi_{0.5}Co_{0.5}O_{3-\delta}$	BZCYYb4411			0.62	0.44	0.3	0.2	35
$Ba_{0.5}Sr_{0.5}(Co_{0.8}Fe_{0.2})_{0.95}P_{0.05}O_{3-\delta}$	BZCYYb1711			0.84	0.64	0.42		36
$Pr_{0.1}Ce_{0.9}O_2$-$PrBaCo_2O_{5+\delta}$	BZCYYb1711	1.78	1.21	0.86				30
$Ba_{0.95}(Co_{0.4}Fe_{0.4}Zr_{0.1}Y_{0.1})_{0.95}Ni_{0.05}O_{3-\delta}$	BZCYYb1711			0.94	0.67	0.43	0.26	37
$PrBa_{0.8}Ca_{0.2}Co_2O_{5+\delta}$	BZCYYb1711	1.916	1.58	1.09	0.663			33

$PrBaCo_2O_{5+\delta}$ -$BaCoO_{3-\delta}$	BZCYYb1711		1.68	1.04	0.635	0.387		[32]
$BaCo_{0.4}Fe_{0.4}Zr_{0.1}Y_{0.1}O_{3-\delta}$	BZCYYb1711			0.639	0.534	0.452		[34]
$PrBa_{0.5}Sr_{0.5}Co_{1.5}Fe_{0.5}O_{5+\delta}$	BZCYYb4411		1.085	0.822	0.593	0.372		[28]
$Ba_{0.9}Co_{0.7}Fe_{0.2}Nb_{0.1}O_{3-\delta}$	BZCYYb1711		1.72	1.21	0.828	0.563		[29]
$Pr_{0.2}Ba_{0.2}Sr_{0.2}La_{0.2}Ca_{0.2}CoO_{3-\delta}$	BZCYYb1711		1.511	1.14	0.6159	0.3864		[38]
$Ba_2Co_{1.5}Mo_{0.25}Nb_{0.25}O_{6-\delta}$	BZCYYb1711	1.5048	1.228	0.8095	0.5429	0.3524		[39]
$Gd_{0.3}Ca_{2.7}Co_{3.82}Cu_{0.18}O_{9-\delta}$	BZCYYb1711	2.05	1.6	1.16	0.77	0.48	0.28	[31]
BSC+PBSCF	BZCYYb1711				1.22	0.83	0.55	[40]
$Ba_{0.875}Fe_{0.875}Zr_{0.125}O_{3-\delta}$	BZCYYb1711			1.28	0.95	0.67		[21]

Table 5. Summary of the current landscape of identified promising PCECs with their electrochemical performance under electrolysis mode

			Current Density at 1.3V (A cm^{-2})	Ref

Electrode	Electrolyte	Atmosphere	700 °C	650 °C	600 °C	550 °C	500 °C	450 °C	
PBCHf010	BSCYb172	30%H2O-air||3% H2O-H2			2.78	1.98	0.89	0.4	This Work
$Ba_{0.9}Pr_{0.1}Hf_{0.1}Y_{0.1}Co_{0.8}O_{3-\delta}$	BSCYb172	30%H2O-air||3% H2O-H2		3.67	2.62	1.74	0.96		[26]
$Ba_{0.9}Pr_{0.1}Hf_{0.1}Y_{0.1}Co_{0.8}O_{3-\delta}$	BZCYYb1711	30%H2O-air||3% H2O-H2			2.4	1.406	0.814	0.372	[27]
$PrNi_{0.5}Co_{0.5}O_{3-\delta}$	BZCYYb4411	30%H2O-air||3% H2O-H2			1.2	0.8	0.6	0.4	[35]

$Ba_{0.5}Sr_{0.5}(Co_{0.8}Fe_{0.2})_{0.95}P_{0.05}O_{3-\delta}$	BZCYYb 1711	10%H2O-air||3% H2O-H2			0.8	0.5	0.31		[36]
$Pr_{0.1}Ce_{0.9}O_2$-$PrBaCo_2O_{5+\delta}$	BZCYYb 1711	3%H2O-air||3% H2O-H2	3.7	2.7	2.1				[30]
$Ba_{0.95}(Co_{0.4}Fe_{0.4}Zr_{0.1}Y_{0.1})_{0.95}Ni_{0.05}O_{3-\delta}$	BZCYYb 1711	5%H2O-air||3% H2O-H2			1.27	0.856	0.507	0.3	[37]
$PrBa_{0.8}Ca_{0.2}Co_2O_{5+\delta}$	BZCYYb 1711	50%H2O-air||3% H2O-H2		2.5	1.5	0.7			[33]
$PrBaCo_2O_{5+\delta}$ -$BaCoO_{3-\delta}$	BZCYYb 1711	30%H2O-air||3%		2.75	1.8	1.1			[32]

		H2O-H2							
$BaCo_{0.4}Fe_{0.4}Zr_{0.1}Y_{0.1}O_{3-\delta}$	BZCYYb1711	10%H2O-air‖3%H2O-H2			1	0.77	0.609		[34]
$PrBa_{0.5}Sr_{0.5}Co_{1.5}Fe_{0.5}O_{5+\delta}$	BZCYYb4411	3%H2O-air‖3%H2O-H2		2.25	1.4	0.8	0.4		[28]
$Ba_{0.9}Co_{0.7}Fe_{0.2}Nb_{0.1}O_{3-\delta}$	BZCYYb1711	3%H2O-air‖3%H2O-H2		2.76	1.548	0.7366	0.261		[29]
$Pr_{0.2}Ba_{0.2}Sr_{0.2}La_{0.2}Ca_{0.2}CoO_{3-\delta}$	BZCYYb1711	3%H2O-air‖3%H2O-H2		2.685	1.7528	0.8034	0.2809		[38]

$Ba_2Co_{1.5}Mo_{0.25}Nb_{0.25}O_{6-\delta}$	BZCYYb1711	3%H2O-air||3% H2O-H2		1.904	1.33	0.7826			[39]
$Gd_{0.3}Ca_{2.7}Co_{3.82}Cu_{0.18}O_{9-\delta}$	BZCYYb1711	20%H2O-air||3% H2O-H2	4.3478	3.0039	2.2	1.2648	0.7905		[31]

Table 6. Summary of vibration frequency for surface adsorbed species

PBC (*OO)	904.5148	481.1436	362.5196	201.5264	173.266	151.9902			
PBC (*O)	775.0839	162.7703	139.2061						
PBC (*O+*H)	3580.334	871.9096	767.7579	459.91	185.8841	178.66			
PBC (*OH)	3656.713	902.0057	519.7335	362.6203	174.9357	38.73442			
PBC (*OH+*H)	3727.166	3481.243	855.3854	689.3013	545.1276	540.3105	345.9701	165.5427	132.2481

Hybrid (*OO)	1071.24	494.14	282.1428	196.9131	126.3049	88.63609			
Hybrid (*O)	756.3214	191.6701	177.1186						
Hybrid (*O+*H)	3591.079	973.8809	512.169	478.934	199.2578	183.7914			
Hybrid (*OH)	3582.351	839.6039	618.9015	425.6401	169.6164	140.9573			
Hybrid (*OH+*H)	3743.039	3575.998	841.0952	693.1377	525.9785	422.4371	304.6478	144.3321	73.25025

Unit: cm^{-1}

References

1. P. E. Blochl, *Phys Rev B*, 1994, **50**, 17953-17979.
2. G. Kresse and J. Furthmuller, *Comp Mater Sci*, 1996, **6**, 15-50.
3. J. P. Perdew, K. Burke and M. Ernzerhof, *Phys Rev Lett*, 1996, **77**, 3865-3868.
4. A. Jain, S. P. Ong, G. Hautier, W. Chen, W. D. Richards, S. Dacek, S. Cholia, D. Gunter, D. Skinner, G. Ceder and K. A. Persson, *Apl Mater*, 2013, **1**.
5. V. Somjit and B. Yildiz, *Acs Appl Mater Inter*, 2022, **14**, 42613-42627.
6. C. Chen and S. P. Ong, *Nat Comput Sci*, 2022, **2**, 718-+.
7. R. Jacobs, T. Mayeshiba, J. Booske and D. Morgan, *Adv Energy Mater*, 2018, **8**.
8. L. Zhao, J. Drennan, C. Kong, S. Amarasinghe and S. P. Jiang, *J Mater Chem A*, 2014, **2**, 11114-11123.
9. Y. Xie, N. Shi, X. Y. Hu, K. Zhu, R. R. Peng, C. R. Xia and M. Chen, *J Electrochem Soc*, 2023, **170**.
10. Z. Liu, Y. Bai, H. Sun, D. Guan, W. Li, W.-H. Huang, C.-W. Pao, Z. Hu, G. Yang and Y. Zhu, *Nat Commun*, 2024, **15**, 472.
11. K. J. Yoon, M. Biswas, H. J. Kim, M. Park, J. Hong, H. Kim, J. W. Son, J. H. Lee, B. K. Kim and H. W. Lee, *Nano Energy*, 2017, **36**, 9-20.
12. G. Bergerhoff, R. Hundt, R. Sievers and I. Brown, *Journal of chemical information and computer sciences*, 1983, **23**, 66-69.
13. X. Y. Hu, Y. Xie, Y. H. Wan, Y. Yang, X. J. Wu and C. R. Xia, *Appl Catal B-Environ*, 2021, **286**.

14. Y. P. Cao, M. J. Gadre, A. T. Ngo, S. B. Adler and D. D. Morgan, *Nat Commun*, 2019, **10**.
15. G. Henkelman, B. P. Uberuaga and H. Jonsson, *J Chem Phys*, 2000, **113**, 9901-9904.
16. W. L. Zhang, X. Y. Hu, Y. C. Zhou, Z. Y. Luo, G. Nam, Y. Ding, T. T. Li, Z. J. Liu, Y. J. Ahn, N. Kane, W. N. Wang, J. Hou, D. Spradling and M. L. Liu, *Adv Energy Mater*, 2022, **12**.
17. V. Wang, N. Xu, J. C. Liu, G. Tang and W. T. Geng, *Comput Phys Commun*, 2021, **267**.
18. Y. H. Wan, Y. L. Xing, Y. H. Li, D. M. Huan and C. R. Xia, *J Power Sources*, 2018, **402**, 363-372.
19. J. Suntivich, H. A. Gasteiger, N. Yabuuchi, H. Nakanishi, J. B. Goodenough and Y. Shao-Horn, *Nat Chem*, 2011, **3**, 647-647.
20. Z. Y. Luo, Y. C. Zhou, X. Y. Hu, N. Kane, W. L. Zhang, T. T. Li, Y. Ding, Y. Liu and M. L. Liu, *Acs Energy Lett*, 2022, DOI: 10.1021/acsenergylett.2c01544, 2970-2978.
21. Z. Wang, Y. H. Wang, J. Wang, Y. F. Song, M. J. Robson, A. Seong, M. T. Yang, Z. Q. Zhang, A. Belotti, J. P. Liu, G. Kim, J. Lim, Z. P. Shao and F. Ciucci, *Nat Catal*, 2022, **5**, 777-787.
22. T. Sun, Z. Y. Tang, W. J. Zang, Z. J. Li, J. Li, Z. H. Li, L. Cao, J. S. D. Rodriguez, C. O. M. Mariano, H. M. Xu, P. Lyu, X. Hai, H. H. Lin, X. Y. Sheng, J. W. Shi, Y. Zheng, Y. R. Lu, Q. He, J. S. Chen, K. S. Novoselov, C. H. Chuang, S. B. Xi, X. Luo and J. Lu, *Nat Nanotechnol*, 2023, **18**, 763-+.
23. R. R. Zarr, G. R. Dalton and S. M. Fioravante, *Therm Cond*, 2000, **25**, 259-265.
24. L. Yang, S. Z. Wang, K. Blinn, M. F. Liu, Z. Liu, Z. Cheng and M. L. Liu, *Science*, 2009, **326**, 126-129.
25. Y. Zhang, R. Knibbe, J. Sunarso, Y. J. Zhong, W. Zhou, Z. P. Shao and Z. H. Zhu, *Adv Mater*, 2017, **29**.
26. Z. Luo, X. Hu, Y. Zhou, Y. Ding, W. Zhang, T. Li and M. Liu, *Adv Mater*, 2024, 2311159.
27. W. Zhang, Y. Zhou, X. Hu, Y. Ding, J. Gao, Z. Luo, T. Li, N. Kane, X.-Y. Yu and T. Terlier, *Acs Energy Lett*, 2023, **8**, 3999-4007.
28. S. Choi, T. C. Davenport and S. M. Haile, *Energ Environ Sci*, 2019, **12**, 206-215.
29. K. Pei, Y. Zhou, K. Xu, H. Zhang, Y. Ding, B. Zhao, W. Yuan, K. Sasaki, Y. Choi and Y. Chen, *Nat Commun*, 2022, **13**, 2207.
30. K. Pei, S. Luo, F. He, J. Arbiol, Y. Xu, F. Zhu, Y. Wang and Y. Chen, *Applied Catalysis B: Environmental*, 2023, **330**, 122601.
31. M. Saqib, I.-G. Choi, H. Bae, K. Park, J.-S. Shin, Y.-D. Kim, J.-I. Lee, M. Jo, Y.-C. Kim and K.-S. Lee, *Energ Environ Sci*, 2021, **14**, 2472-2484.
32. Y. Niu, Y. Zhou, W. Zhang, Y. Zhang, C. Evans, Z. Luo, N. Kane, Y. Ding, Y. Chen and X. Guo, *Adv Energy Mater*, 2022, **12**, 2103783.
33. Y. Zhou, E. Liu, Y. Chen, Y. Liu, L. Zhang, W. Zhang, Z. Luo, N. Kane, B. Zhao and L. Soule, *Acs Energy Lett*, 2021, **6**, 1511-1520.
34. C. Duan, R. Kee, H. Zhu, N. Sullivan, L. Zhu, L. Bian, D. Jennings and R. O'Hayre, *Nat Energy*, 2019, **4**, 230-240.
35. H. Ding, W. Wu, C. Jiang, Y. Ding, W. Bian, B. Hu, P. Singh, C. J. Orme, L. Wang and Y. Zhang, *Nat Commun*, 2020, **11**, 1907.
36. Z. Liu, D. Cheng, Y. Zhu, M. Liang, M. Yang, G. Yang, R. Ran, W. Wang, W. Zhou and Z. Shao, *Chem Eng J*, 2022, **450**, 137787.

37. M. Liang, Y. Wang, Y. Song, D. Guan, J. Wu, P. Chen, A. Maradesa, M. Xu, G. Yang and W. Zhou, *Applied Catalysis B: Environmental*, 2023, **331**, 122682.
38. F. He, Y. Zhou, T. Hu, Y. Xu, M. Hou, F. Zhu, D. Liu, H. Zhang, K. Xu and M. Liu, *Adv Mater*, 2023, **35**, 2209469.
39. F. He, S. Liu, T. Wu, M. Yang, W. Li, G. Yang, F. Zhu, H. Zhang, K. Pei and Y. Chen, *Adv Funct Mater*, 2022, **32**, 2206756.
40. F. Liu, H. Deng, D. Diercks, P. Kumar, M. H. A. Jabbar, C. Gumeci, Y. Furuya, N. Dale, T. Oku, M. Usuda, P. Kazempoor, L. Y. Fang, D. Chen, B. Liu and C. C. Duan, *Nat Energy*, 2023, DOI: 10.1038/s41560-023-01350-4.